Design of a New Low-Energy Beamline in CERN's North Area for the NA61/SHINE Experiment

C. A. Mussolini

Thesis submitted in fulfilment
of the requirements for the degree of
Doctor of Philosophy

St. John's College
University of Oxford
Trinity Term, 2023

Abstract

One of the largest North Area fixed-target experiments at CERN, NA61/SHINE, has shown interest in cross-section measurements involving protons, pions, and kaons in the 2 to 13 GeV/c momentum range. However, the current infrastructure in CERN's North Area Experimental Hall proves to be unsuitable for the transport of particles in these low-momentum ranges. For this reason, the design and optimisation of a new tertiary beamline branch which will serve NA61/SHINE and other future experiments is necessary and will constitute the subject of this D.Phil thesis.

Specifically, in this thesis, the entire design process of this new low-energy beamline has been addressed. Extensive studies into the optimisation of the secondary target and primary beam energy which will be used to produce the low-energy hadrons have been performed, leading to the selection of three targets aiming to optimise the beamline performance in different scenarios. Furthermore, significant work has gone into developing a novel optimisation process to meet the design specifications imposed by the experiment onto the beamline. This novel optimisation procedure has been used to maximise the beamline's acceptance while providing a good momentum resolution and small beam-spot size to the experiment. The performance of this beamline design has then been extensively studied using a range of tools, including TRANSPORT, MAD-X PTC, and G4Beamline, to ensure that the figures of merit this beamline will be capable of delivering will meet the experimental needs.

Additionally, the instrumentation which will be installed in the beamline has been selected and will enable particle-by-particle identification over the entire 2 to 13 GeV/c operational range. The effects of the additional material this instrumentation will introduce on the beam have also been studied, with a focus on the particle rate and beam-spot size at the NA61/SHINE target.

Finally, the beamline's possible future implementation into CERN's North Area is discussed and a scheme for its installation is proposed. Additionally, a FLUKA study of the feasibility of the beamline from the point of view of radiation safety is presented.

To my Mum,
under *duress*

Acknowledgements

I would like to begin by expressing my gratitude to my family who, although have been having more and more exotic ideas regarding my work and research as the years have progressed, have always been by my side. I would not be the person that I am today without the endless support that they have offered me since childhood, and for that I will always be grateful. I also have an “amazing, funny, beautiful” sister, hi Coco.

I am also profoundly grateful to the people who have guided me down the road of my education, from secondary school, through university, and all the way to the completion of this D.Phil thesis. Their guidance, insights and encouragement have been instrumental in shaping my academic path, my research interests, and ultimately, me.

I think it makes most sense to begin by thanking the people who first showed me what being a physicist entails. I’m incredibly grateful to Prof. Francesco Arneodo and Dr. Adriano Di Giovanni for the opportunity they gave me in 2014, and again in 2016 and 2017, when they allowed me to take part in several internships at the Laboratori Nazionali del Gran Sasso. The work I did with them during these internships opened my eyes to what a physicist does, and it is in no small part thanks to them, that I decided to embark on my journey to study physics at university.

Following this, I would like to extend my gratitude to Prof. Stephen Blundell and Prof. Steve Biller, my physics tutors during my time as an undergraduate student at Mansfield College. Their knowledge, insights, and teachings have left an indelible mark on me and my way of thinking, and I will be forever grateful for the countless hours we spent together going over problem sets during my time at Oxford. I can wholeheartedly say that I would not be the physicist that I am today were it not for all the lessons and support that they offered me over the years.

Next, I owe an immense debt of gratitude to my D.Phil supervisors, Dr. Nikolaos Charitonidis, and Prof. Philip Burrows. Throughout the entirety of this journey, they have perfectly balanced the challenge of a D.Phil with the guidance they provided, and it is thanks to them that I developed into an independent researcher. Truly, it would take someone with a much greater mastery of the English language to express the extent of my gratitude and respect for both Nikos and Phil, however, what I can say without a shred of a doubt is that I will be forever grateful to them for these past four years. I decided to do a D.Phil because I wanted to produce my own contributions to Physics, and I can say that thanks to them, I have managed to do just that in my time at CERN.

Finally, I want to thank the fantastic people who have made these past years a wonderful chapter of my life. Without my friends both in Geneva and in Oxford, my time during my D.Phil would have been immeasurably less pleasant, and I owe to them much of my personal growth over these past years. Amongst all my friends I must thank a few separately. Firstly, and foremost, I need to thank Elodie Pons, who was a great support during this D.Phil and who made the most emotionally testing parts of this journey much more manageable. Secondly, I want to thank my office mate Elisabetta, who became a really great friend over my time in Geneva. Our talks in the office will be some of my most cherished memories of CERN! And finally, Giulia Mecacci, who became an incredibly close friends of mine and someone who I can always count on for great advice.

Contents

List of Figures

List of Tables

Chapter 1

Introduction

Before delving into the novel work produced during the course of this DPhil, it is important to provide the background to understand CERN, the NA61/SHINE experiment, and what this project has aimed to achieve. To this end, this chapter provides an overview of the CERN accelerator complex and the North Area, the facility where this beamline may operate in the future, followed by a description of NA61/SHINE and its physics goals. These are then used to highlight the need for a novel low-energy beamline in CERN's North Area alongside its desired performance. Finally, an introduction to the remaining chapters of the thesis and what they will tackle is presented.

1.1 An Overview of CERN's Experimental Areas

This section provides a brief overview of CERN and the many facilities present there, with an emphasis on the North Area and the Experimental Hall 1, as this is the location in which the low-energy beamline has been envisioned.

1.1.1 The CERN Accelerator Complex

The European Organization for Nuclear Research (CERN), comprised of several particle accelerators, beamlines and transfer tunnels, and experiments is one of the world's leading particle physics research campuses, whose extent can be seen in *Figure* 1.1. Thanks to the scale of the facilities and the range of experiments performed at CERN, many great discoveries, from the W and Z bosons [1], to the Higgs boson [2] have been made there over the past 40 years.

Protons are produced by stripping the electrons from elementary hydrogen. These are then accelerated through a chain of particle accelerators to reach energies on the TeV scale. This chain of accelerators begins by feeding H^- ions into the LINAC 4 machine, which accelerates them to 160 MeV. These are then stripped to H^+ and transported to

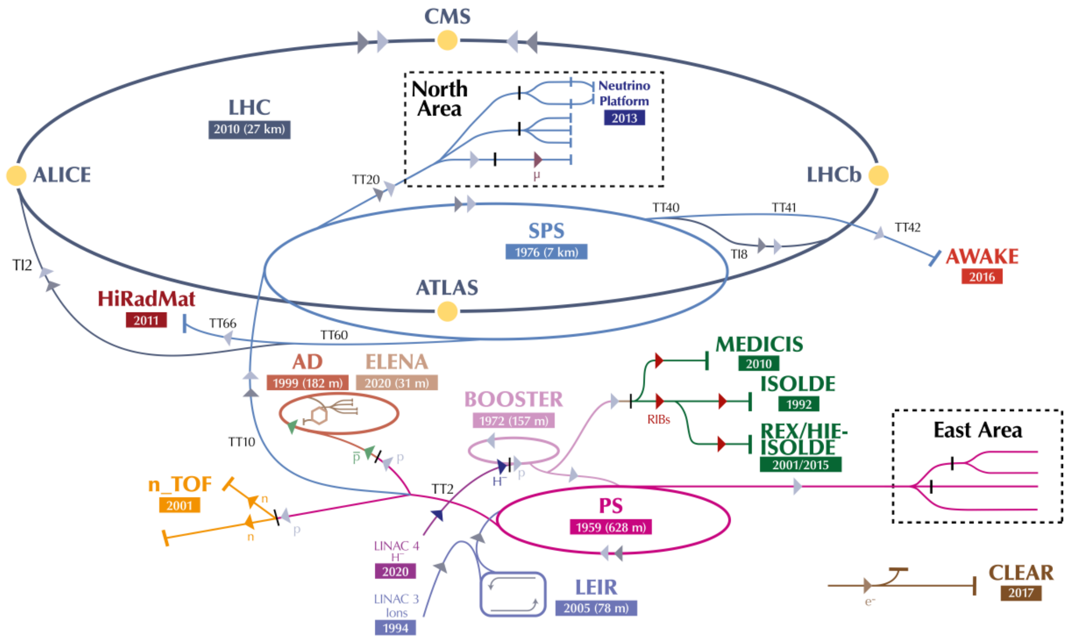

Figure 1.1: The CERN accelerator complex and the many facilities and experiments currently present there [3].

the Proton Synchrotron Booster (PSB). Here particles are further accelerated up to 2 GeV. The accelerator chain then continues with the Proton Synchrotron (PS) and the Super Proton Synchrotron (SPS) which accelerate particles up to 26 GeV and 450 GeV respectively. Finally, the high energy protons can then be injected into the Large Hadron Collider (LHC), where they can be accelerated to energies up to 6.8 TeV [3].

This chain of accelerators is what enables the success of experiments requiring extremely high energy particles, such as ATLAS and CMS, however many other experiments are present which require either much lower energies or particles other than protons. For this reason it is also possible to extract particles at several stages prior to injection into the LHC and deliver them to the experimental areas. For example, following acceleration in the PS, particles can be delivered to CERN's East Area (EA) [4], where experiments such as CLOUD [5] and IRRAD/CHARM [6] use lower energy particles. Another such area is the one which uses 400 GeV energy particles extracted from the SPS, the North Area (NA) [7].

A second chain of accelerators, also ending by injecting particles into the SPS, is also present to accelerate ions. The ions are first accelerated up to energies of about 4.2 MeV/u in LINAC 3 and then are injected over about 70 turns into the Low Energy Ion Ring (LEIR) up to six times every 200 ms, where they reach energies of 72 MeV/u. The ions are then injected into the PS, where they follow the same accelerator chain as the protons [8].

1.1.2 The North Area Facilities

The North Area secondary beam facilities, a schematic of which is shown in *Figure* 1.2, include several fixed target experiments and the beamlines needed to transport the secondary and tertiary particles required by them [9]. Secondary beams are produced approximately 350 metres upstream of the North Area, in an underground cavern designated TCC2, via the interaction of the 400 GeV beam extracted from the SPS with thin beryllium targets designated T2, T4, T6, and T10 [10]. These targets enable the production of secondary beams with momenta ranging from as low as 15 GeV/c to 400 GeV/c and with a variable range of particle composition that can be tuned for the needs of each experiment [11]. Here, the selection of the beam momentum and the beam composition is performed with collimators and bending magnets. The North Area is divided into three Experimental Halls: Experimental Hall 1 (EHN1), 2 (EHN2), and 3 (ECN3), each hosting different experiments.

1.1.3 Experimental Hall North Area 1 (EHN1)

EHN1 is comprised of four beamlines, H2, H4, H6 and H8, emerging from the targets T2 and T4 [10]. These beamlines serve several permanent or quasi-permanent fixed target experiments but can also be used for test beams or parasitic experiments that may be installed behind the main experiments. Particles here are delivered in spills with a flat top spill duration of 4.8 seconds and a super-cycle length dependent on the overall CERN physics programme. In the North Area, these spills consist of a maximum of 10^8 particles underground and 10^7 in the surface buildings, mainly due to radiation protection regulations. All EHN1 beamlines provide a momentum resolution of up to approximately 2% [10].

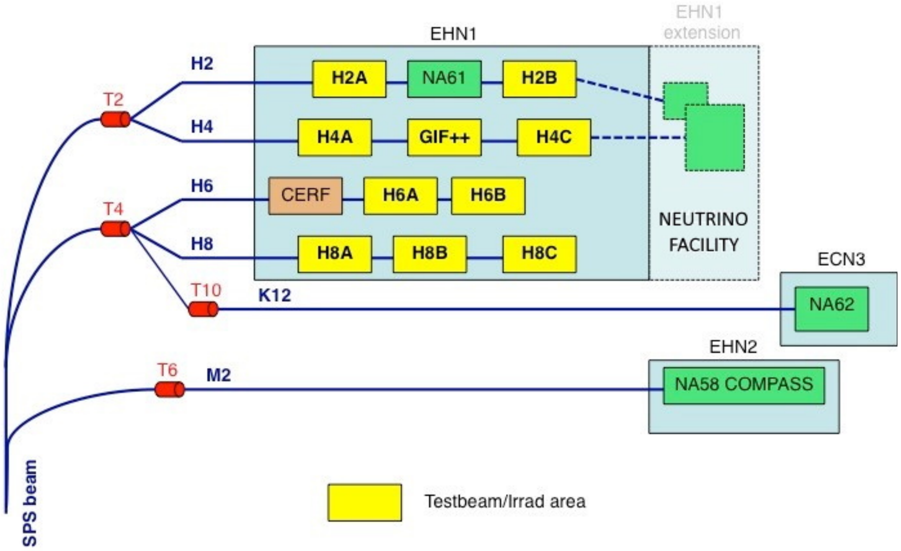

Figure 1.2: The North Area, its beamlines, experiments and target stations. The figure shows how the approximately 5.8 km of beamlines split the beam extracted from the SPS to reach various experiments [12].

In EHN1, beamlines are also equipped with several types of detectors to monitor and control the beam properties. Wire chamber monitors are present to measure the beam profile, scintillators are installed in order to count the beam intensity while other types of detectors, such as threshold Cherenkov counters, are used for particle identification and tagging.

1.2 The NA61/SHINE Experiment

This section provides a brief description of the NA61/SHINE experiment, the collaboration's physics goals, and the NA61/SHINE detector. In-depth discussion of these is also readily available in the literature, for example in Ref. [13] and in Ref. [14], where details of the experiment have been presented in much greater detail than necessary for this thesis. In this section, the description of future measurements the collaboration wishes to perform and their significance to the broader community are introduced. Finally, the reasons for which these measurements cannot be currently performed are described, introducing the need for a new low-energy beamline serving NA61/SHINE.

1.2.1 Overview of the Experiment

NA61/SHINE [13] is a fixed target experiment present in EHN1 which took data for the first time in 2009 and has been present since, although the experiment itself is a continuation of the older NA31 and NA49 experiments. NA61/SHINE's physics goals are to study hadron production in hadron-proton, hadron-nucleus and nucleus-nucleus interactions, with the main aims of:

1. advancing the understanding of the onset of deconfinement and the search for the critical point of strongly interacting matter [15],
2. obtaining precise hadron production measurements for improving calculations of neutrino beam flux in long-baseline neutrino oscillation experiments [16].

1.2.2 The NA61/SHINE Detector and Triggering System

The detection system of NA61/SHINE, shown schematically in *Figure* 1.3, consists of four large Time Projection Chambers (TPCs). Two of these, called the Vertex Time Projection Chambers (VTPCs), are placed inside a strong magnetic field provided by two large superconducting magnets, with a total bending power of up to 9 Tm, while the two other TPCs, denoted as Main Time Projection Chamber Left and Right respectively (MTPC-L, MTPC-R) are placed further downstream. These enable particle tracking by detecting the trail of electrons left by a high energy particle as it travels through gas. By applying a strong vertical electrical field, these electrons are then drifted upwards towards a proportional wire chamber where their number, position and timing are measured to achieve a high spatial resolution. A smaller TPC, the GAP-TPC, is present between the two VTPCs, and uses a similar technique to track particles, increasing the resolution of data for particles which have small production angles. Behind the MTPCs, a large set of scintillators serve as Time-of-Flight counters. These are called the TOF Front (TOF-F), TOF Right (TOF-R) and and TOF Left (TOF-L). They are used to extend the range over which the experiment can perform particle identification [13].

H2, the beamline serving NA61/SHINE is equipped with a series of scintillators,

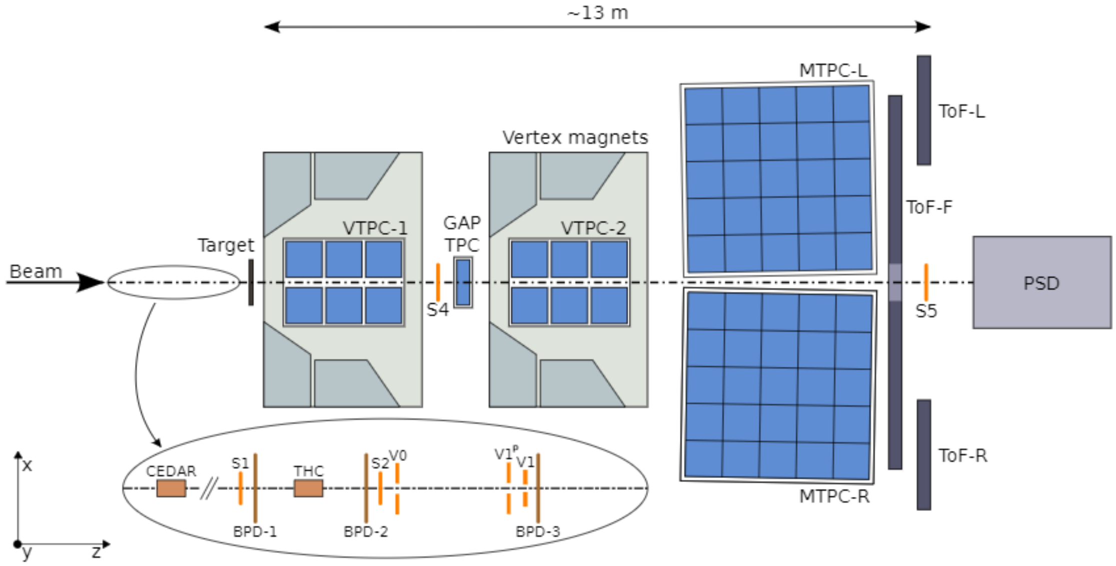

Figure 1.3: A schematic view of the position of the detectors used by NA61/SHINE. Included in the image are the various scintillating detectors which are used as triggers and vetoes [13].

Cherenkov counters, veto counters, and beam position detectors (BPDs). These are used to obtain information on the timing of the particles, the charge of the beam and its position.

The scintillators and Cherenkov counters are used either in coincidence or anticoincidence to trigger the detectors or veto the background particles. For example, to ensure data is taken only when an interaction occurred, the S5 detector, placed downstream of the experiment, is used in anticoincidence, or as a veto, as events interacting with this are generally caused by the beam passing through the target without interacting.

The trajectory of the beam before the NA61/SHINE target and the position of the interaction vertex is measured using three sets of BPDs. These are placed over a distance of approximately 30 metres and consist of orthogonal wire planes to measure an induced charge to obtain the x and y coordinates of the beam at a given z position of the beamline. These measurements are then combined to reconstruct a beam track.

1.2.3 Desired Future Measurements

There has been rising interest in extending the neutrino programme of NA61/SHINE towards lower energy measurements, as currently data which could prove to be extremely important to several neutrino experiments is not available. Many neutrino experiments lack the data to constrain the predictions of neutrino beam fluxes, leading to uncertainties of over 5% [17] in some measurements, much larger than what is currently needed. Moreover, low-energy data are necessary to improve the reliability of simulation tools like GEANT4, where better interaction cross section measurements would prove to be extremely useful.

The number of requests for low-energy hadron beam measurements using the unique NA61/SHINE detector system has grown significantly over the past years, with a brief and non-exhaustive summary of these being shown in *Table* 1.1 [17].

Experiment	Beam particle	Beam momentum	Target materials
T2K [18], Hyper-K [19]	$\pi^{\pm}$, $\mathrm{K}^{\pm}$, p	3-13 GeV/c	Al, C, Fe, He
DUNE [20]	$\pi^{\pm}$, $K^{\pm}$	3-13 GeV/c	Al, C, Ti
T2K, Hyper-K, DUNE	p	2-13 GeV/c	air (N, O), C
JSNS^2 [21]	p	3.82 GeV/c	Hg
MLF [22]	p	3.82 GeV/c	Hg, W, C, lead-bismuth
Short-Baseline	p	8 GeV/c	Be

Table 1.1: Summary of the data requested by various experiments.

In brief, for the T2K and Hyper-K beams, the data which may be obtained using this beamline will be used to constrain the production distribution of hadrons which are the parents of neutrinos. This will be crucial to predict the neutrino flux and its uncertainty, as, at 0.6 GeV/c, for example, the uncertainty on the flux is around 5%, with hadron production being the dominant source.

For the Deep Underground Neutrino Experiment (DUNE) low-energy pion and kaon interactions and, importantly, re-interactions within the horn are the leading source of flux uncertainty. These flux uncertainties lead to errors in measurements around the first and second neutrino oscillation maxima that range between 4% and 8%, while DUNE's requirement are for these uncertainties to be below 3%. Data from the low-energy beamline would be helpful for achieving these lower uncertainties.

For the atmospheric ν measurements of Super-K, DUNE, and Hyper-K, this beamline will provide data to better understand the dominant source of uncertainties which arises from our lack of understanding of hadron production in the atmosphere (e.g. p+ N $\rightarrow \pi^{\pm}$/ K$^{\pm}$+X). These uncertainties lead to errors in neutrino flux predictions of over 10%, which limit measurement sensitivity.

The JSNS^2 experiment, searching for sterile neutrinos with short-baseline neutrino oscillations, produces neutrinos via the interaction of a 3 GeV proton beam with a Hg target. It does this to study the number of $\bar{\nu}_\mu$ which oscillate into $\bar{\nu}_e$, however, a significant number of $\bar{\nu}_e$ are produced via the decay of $\pi^- \rightarrow \mu^- \rightarrow \bar{\nu}_e$. As no measurements are available on π^- production from 3 GeV protons and Hg, the JSNS^2 experiment has estimated the uncertainties arising from this intrinsic background to be on the order of 50%. The acquisition of data on these interactions would be vital for decreasing these uncertainties.

Finally, for both the Materials and Life Science Experimental Facility (MLF) at J-PARC and the Short Baseline Neutrino (SBN) experiments, the proposed beamline could provide data on the interactions of beams of different energies with different targets. For the MLF experiment, the interaction of a 3 GeV proton beam with targets such as mercury, tungsten or lead-bismuth would be vital, whereas for the SBN, the data for the interaction of an 8 GeV proton beam with a beryllium target would significantly decrease the experimental uncertainties arising from neutrino flux calculations, as was the case for the other neutrino experiments discussed above.

More information regarding these experiments, their aims, and their request can be found in Ref. [17] and in Ref. [23].

To perform these measurements, stringent requirements have been placed on the beams which will be required for the neutrino programme of NA61/SHINE. These will be secondary hadron beams with momenta ranging from 2 GeV/c to 13 GeV/c with a small tolerance on momentum error. To maximise the rate of interaction with the NA61/SHINE target, these beams will need to be well-focused, with a beam-spot size smaller than 20 mm RMS. Additionally, to maintain rates of pile-ups comparable to what has been currently achieved, these secondary beams must mainly consist of protons, pions and kaons. These requirements have been summarised in *Table* 1.2.

Parameters	Requirements
Particle type	p, $\pi^{\pm}$, $\mathrm{K}^{\pm}$
$\Delta p/p$	$< 5\%$
Beam size RMS	20 mm at the NA61/SHINE target
Maximum rate	1.5×10^4 Hz
Minimum number of particles per spill	250

Table 1.2: The requirements on the secondary beam delivered to the NA61/SHINE target, obtained from NA61/SHINE's Letter of Intent for the development of the low-energy secondary beamline, submitted to the Super Proton Synchrotron Committee (SPSC) in 2021 [17].

1.2.4 The Need for a New Beamline in the North Area

The current infrastructure, specifically the H2 beamline, is currently not suitable for performing the low-energy measurements desired by NA61/SHINE and the experiments discussed previously. These current limitations arise from several factors.

First amongst these is the fact that the experimental hall was originally designed for beams of 400 GeV/c protons, and while a huge amount of flexibility was included in the initial designs, the infrastructure was never meant to handle low-energy beams. Hence, the magnets and their power supplies are designed to operate at the currents which are necessary for a 400 GeV/c beam [24]. If we were to require these same magnets and power supplies to operate at 5 GeV/c, we would need currents approximately 80 times smaller, and the power supplies simply cannot provide such low currents stably, meaning that the beam itself would be unstable. Clearly this would not be acceptable from the point of view of NA61/SHINE.

Furthermore, the current H2 beamline has a relatively small acceptance, which is appropriate for secondary particles produced at energies of 70 GeV and above by a beam containing upwards of 10^{12} primary protons, but leads to insufficient rates at lower energies. This is an issue as it would not enable NA61/SHINE to obtain sufficient statistics when considering the busy beam schedule of the North Area.

This issue would only be exacerbated by the last problem which arises from using existing infrastructure: the length of the beamline. As the secondary targets and the “wobbling stations" [25–27] are more than 350 metres upstream of NA61/SHINE, many of the pions produced here, and all of the kaons, would decay before reaching the experiment. This again would lead to unreasonably small particle rates.

Despite these challenges, building a low-energy beamline in EHN1 would prove to be invaluable due to the unique infrastructure available at CERN and the possibility of leveraging the equipment and expertise of the NA61/SHINE collaboration. NA61/SHINE has historically been a key player in the measurements of neutrino-relevant cross-sections and the instrumentation for performing these complex measurements is already in place [28] so, while designing a new low-energy beamline may be seen as a large commitment, this pales in comparison to developing an entirely new experiment with the sole aim of performing these vital measurements.

Additionally, due to the unparalleled flexibility provided in the North Area, modifying the existing infrastructure to accommodate a low-energy beamline is well within what can be achieved. Furthermore, using the H2 beamline also makes sense when one considers the types of beams delivered in EHN1. Specifically, the high energy beam extracted from the SPS maximises the number of secondary pions and kaons produced. This can be seen both from data in Ref. [29] and in the target studies which have been performed in the context of this thesis, presented in Chapter 3. This will enable much higher particle rates than could be achieved elsewhere, taking advantage of the world-class infrastructure provided at CERN.

1.3 Conceptual Design of the Low-Energy Beamline

Having highlighted the need for a low-energy beamline in the previous section, this section begins with a description of how this beamline will function, followed by the requirements from NA61/SHINE around which it has been designed. A final section introduces the objectives for the successful completion of this beamline, such as the selection of the secondary target, the design and optimisation of the optics, the choice of instrumentation for the tagging of these particles, and the addressal of many technical challenges regarding the implementation of a novel beamline. This discussion presents how these have been separated and tackled in this thesis.

1.3.1 The Low-Energy Beamline

This beamline would serve to extend NA61/SHINE's experimental capabilities and enable the measurement of the properties of secondary low-energy hadrons with momenta in the range from 2 to 13 GeV/c. Specifically, it would enable measurements of the hadron production cross sections of protons, pions and kaons in low momentum hadron-nucleus interactions while simultaneously not negatively impacting NA61/SHINE's experimental capabilities at 400 GeV/c. The beamline, conceptually shown in *Figure* 1.4, would be installed as a new branch along the H2 beamline and would be used to transport secondary particles from a production target to the experiment's target. Particles produced here would then be analysed using the NA61/SHINE TPC.

The branch would be approximately 55 metres long, beginning with a set of secondary targets, selected to deliver a wide range of beams to the experiment. These would define the upper bound of the particle rate and the composition of particles which would reach the interaction target used by NA61/SHINE.

The low-energy beamline itself would be made up of three separate sections, the front end, the momentum selection station, and the back-end. The front end, comprised of two large-aperture quadrupole magnets, would be used to initially control the beam, and defines the geometrical acceptance. Downstream, a four bend achromat would act as a momentum spectrometer and would be used to remove off-momentum particles with a

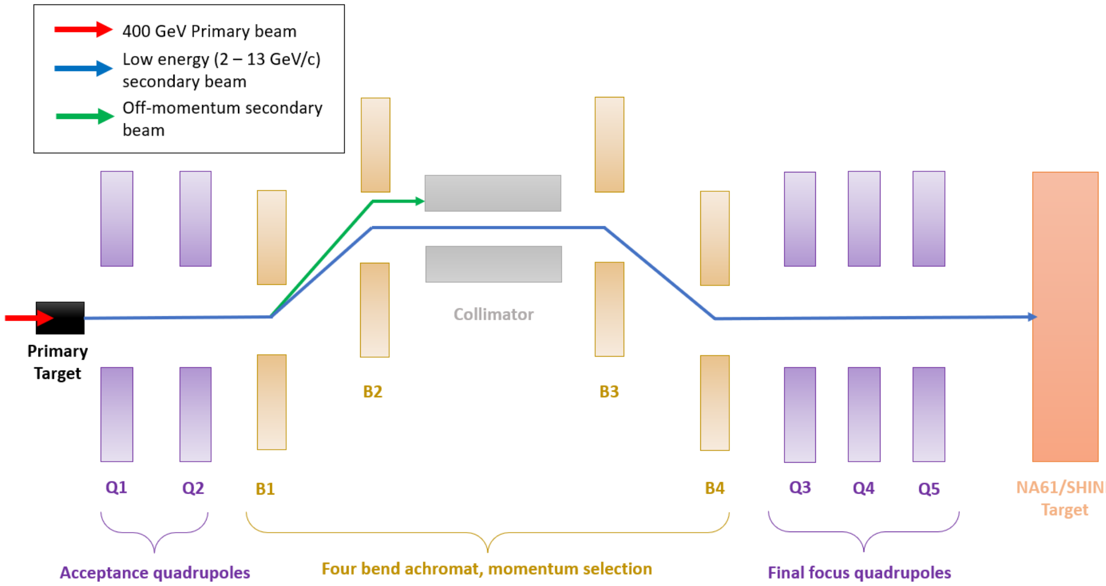

Figure 1.4: The conceptual design of the low-energy beamline. The purple elements are quadrupoles, the yellow elements are bending magnets. The momentum selection is achieved with a collimator placed at the maximum dispersion point.

collimator. Finally, these hadrons would be focused onto the NA61/SHINE target by the back-end of the beamline, made up of three quadrupoles.

Instrumentation installed along the beamline would also enable particle-by-particle tagging of all secondary particles that reach the NA61/SHINE target. This can be achieved using a combination of time-of-flight detectors, for tagging particles in the low-momentum range, and threshold Cherenkov counters, used to identify more energetic particles. By combining these technologies, all particles could be identified over the full range of momenta, from 2 GeV/c to 13 GeV/c.

While this beamline would imply significant modifications to the existing H2 beamline, a strong focus has been put in designing it to have a minimal impact on the current operational capabilities of the H2 beamline at 400 GeV/c. By having the low-energy beamline as a branch of H2 and placing several of its magnets on rails, it would be possible to rapidly switch between low-energy operation and 400 GeV/c operation. Thanks to this, the addition of this new low-energy beamline branch is not expected to negatively impact the data-taking capabilities of experiments currently served by H2.

1.3.2 Thesis Outline

The beamline has been considered to be made up of three essential components: the target, used to produce secondary particles, the beamline lattice, which transports the particles, and the instrumentation equipping the line, used to tag the particles. These three components were then joined together to produce a full, implementable design which can be installed into the North Area. These steps have formed the key components of the process by which the beamline has been created; as such they have also guided the structure of this thesis.

Before describing the design process, however, Chapter 2 provides an overview of the mathematical background necessary for the design of secondary beamlines. This chapter has been written with an emphasis on the nomenclature used in the field of secondary beamlines and addresses the R-matrix formalism, its derivation, and limitations. Following this are discussions on the process via which momentum selection is performed and the issues which arise due to chromatic aberrations. Finally, an overview of the effects of beam interactions with material and the software codes used for beamline design are presented.

After this, Chapter 3 describes the selection of the secondary targets which will be used in the low-energy beamline. This beamline may be considered to take particles from a primary or secondary beam, depending on the configuration of the targets in TCC2. This however does not affect any of the conclusions reached in this thesis, as such, the beam impinging onto the low-energy targets is always assumed to be a primary beam, but this is exclusively a matter of nomenclature. To introduce this discussion, an overview of the models used to understand and model particle production in matter has been presented. Following this, a description of the simulations which have been performed and of the analyses these required to arrive at suitable targets for the low-energy beamline is given. Presented here are studies of the effects of various target parameters on the properties of the beams produced. This chapter concludes with the selection of the optimal targets to be used in the low-energy line.

Chapter 4 provides an overview of the requirements and constraints faced by the beamline and how these have been used to design a novel approach to designing secondary beamlines. The chapter begins with an overview of the current design techniques and describes how these have been modified to be more suited to the design of high-acceptance beamlines. It then describes how this new design approach has been used to design the low-energy beamline and presents extensive MAD-X studies of the beamline's performance. The chapter concludes with a comparison of the results which can be obtained using the new and old methodologies.

Chapter 5 provides more extensive studies of the future beamline's performance using Monte-Carlo simulations. In this chapter, the simulations that have been performed are described, alongside the expected performance of the beamline in terms of particle rates, momentum resolution and beam-spot size at a range of nominal momenta. Following this, the simulations are performed again with realistic magnetic field maps and magnet models to assess any effect these might have on secondary particle and background rates.

Complementing the above studies, Chapter 6 presents the instrumentation that will equip the beamline. This chapter begins with a brief discussion on the technologies used followed by how these will be used together to enable particle-by-particle identification of all relevant secondary particles. The overall instrumentation scheme is described alongside a quantitative analysis of the effects the instrumentation will have on the quality of the beam delivered to NA61/SHINE.

With the design of the beamline complete and all instrumentation in place, Chapter 7 describes the studies that had to be performed to assess and advance the implementation of the low-energy beamline in CERN's experimental halls. The discussion begins by describing how the beamline will be installed alongside the H2 beamline without affecting high-energy operations and the changes to the optics of H2 this will entail. Following this, a scheme for the powering of the magnets is discussed using only available power supplies, before finishing the chapter with the assessment of the beamline from a Radiation Protection (RP) point of view.

The final chapter of the thesis, Chapter 8, presents a summary of the work that has been performed, the goals which have been met during the design of the low-energy beamline, and discusses the scope for future work regarding this beamline.

Chapter 2

Transverse Beam Dynamics

While the topics covered in this chapter can be readily found in the literature [30–32], these are often addressed from a point of view which best suits the treatment of particle accelerators, rather than beamlines. These differences, while subtle, may lead to discrepancies in conventions and some confusion. To avoid this, basic concepts, definitions and the mathematical framework of accelerator physics are discussed here.

2.1 The Frenet-Serret Coordinate System

The standard coordinate system used in accelerator physics can be seen in *Figure* 2.1 [33]. In this framework $\hat{\boldsymbol{x}}$ and $\hat{\boldsymbol{y}}$ represent the horizontal and vertical direction respectively, while the path length of the particle is often represented by the symbol s. The direction of this path at a given point is therefore defined by the vector $\hat{\boldsymbol{s}}$.

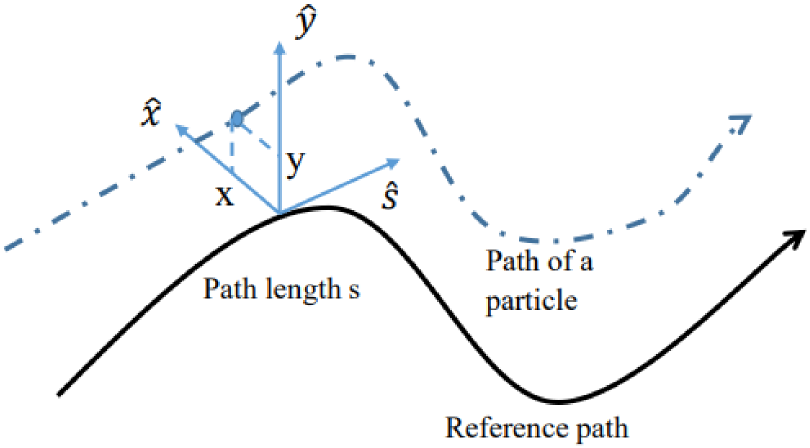

Figure 2.1: The Frenet-Serret coordinate system.

When several particles are present in a beam, their motion is described with respect to the *reference particle*, a particle which follows the ideal, or design, trajectory within the machine. When compared to the reference particle, other particles within the beam can have an offset in their position, given by (x, y) but they can also have different angles in transverse phase space, given by x' and y'. These angles are defined by

$$x' = \frac{dx}{ds} \qquad \text{and} \qquad y' = \frac{dy}{ds}. \tag{2.1}$$

It is commonly assumed that the vast majority of each particle's momentum is in the same direction as the reference particle's, meaning that one can safely assume that that $p \approx p_s$, hence *Equations* 2.1 may be rewritten as [30]

$$x' \approx \frac{p_x}{p} \qquad \text{and} \qquad y' \approx \frac{p_y}{p}. \tag{2.2}$$

Finally, particles in a beam may differ with the reference particle in position along the beam path, given by δs and they may have a different momentum, given by

$$\delta p = p - p_{ref} \tag{2.3}$$

where p_{ref} is the reference particle's momentum and p is the momentum of the particle being studied.

Putting these various coordinates together, one can obtain the particle's position in 6-dimensional phase space, X, given by

$$X = \begin{bmatrix} x \\ x' \\ y \\ y' \\ \delta s \\ \frac{\delta p}{p_{ref}} \end{bmatrix}. \tag{2.4}$$

This coordinate system, called the Frenet-Serret coordinate system, naturally arises in the treatment of charged particles experiencing the Lorentz force, when analysed using Lagrangian mechanics. The mathematics involved in this treatment is both rather cumbersome and readily available in the literature [31], so it will not be addressed in this thesis. On the other hand, the main results of the analysis are of great importance in the context of this work, so these will be discussed in the next section.

2.2 Linear Hill's Equations of Motion

The equation of motion for a charged particle in an electric field E and magnetic field B is

$$\frac{d\bar{p}}{dt} = e(\bar{E} + \bar{v} \times \bar{B}). \tag{2.5}$$

In general, it cannot be solved analytically, however, by disregarding the effects of synchrotron motion, and in cases with zero electric potential and only transverse magnetic fields, it can be simplified significantly into two equations [31, 34].

These simplified equations, which dictate the behaviour of particles in an accelerator, are called the betatron equations of motion [31], and are given by:

$$x'' - \frac{\rho + x}{\rho^2} = \pm \frac{B_y}{B\rho} \frac{p_{ref}}{p} \Big(1 + \frac{x}{\rho}\Big)^2 \tag{2.6}$$

$$y'' = \mp \frac{B_x}{B\rho} \frac{p_{ref}}{p} (\Big(1 + \frac{x}{\rho}\Big)^2 \tag{2.7}$$

where ρ refers to the often used magnetic rigidity, defined via $B\rho = p_{ref}e$. These equations describe the motion of an individual particle in a magnetic field with respect to the reference particle and the betatron oscillation this will undergo as it is transported in the particle accelerator. *Equations* 2.6 and 2.7 are often linearised by dropping the higher order x and y terms as the amplitude of a particle's oscillations around the reference particle is generally small relative to the bending radius.

Considering then a magnetic field in the $y-$direction which has also been expanded up to the first order in x and y,

$$B_x = \frac{\partial B_y}{\partial x} y, \quad B_y = \mp B_0 + \frac{\partial B_y}{\partial x} x \tag{2.8}$$

we can then arrive, by subsisting *Equation* 2.8 into *Equations* 2.6 and 2.7, to:

$$\begin{aligned}
&x'' + K_x(s)x = 0,\\
&y'' + K_y(s)y = 0,\\
&K_x = \frac{1}{\rho^2} \mp \frac{1}{B\rho}\frac{\partial B_y}{\partial x}(s),\\
&K_y = \pm\frac{1}{B\rho}\frac{\partial B_y}{\partial x}(s).
\end{aligned} \tag{2.9}$$

These are in the form of the well-studied Hill's equation [35],

$$x'' + K(s)x = 0, \tag{2.10}$$

and describe the motion of a particle traversing through a focusing function K which is dependent on the magnetic field. In this derivation, only the behaviour of a magnet with dipole and quadrupole components would be accurately described due to the series truncation.

If we consider the functions given by $K(s)$ as piece-wise constant inside the magnets, Hill's equation simply becomes that of a harmonic oscillator, with solutions

$$\begin{aligned}
&u(s) = A \cdot \cos(\sqrt{K}s) + B \cdot \sin(\sqrt{K}s) \quad \text{for} \quad K > 0,\\
&u(s) = As + B \quad \text{for} \quad K = 0,\\
&u(s) = A \cdot \cosh(\sqrt{|K|}s) + B \cdot \sinh(\sqrt{|K|}s) \quad \text{for} \quad K < 0.
\end{aligned} \tag{2.11}$$

By calculating a series of such solutions consecutively for the values of s relevant to each individual element in a beamline, it is then possible to have a solution for the whole machine.

2.3 R-Matrix Formalism

From the solutions to Hill's equation, it becomes useful to consider the evolution of a particle's state vector, defined as

$$U(s) = \begin{bmatrix} u(s) \\ u'(s) \end{bmatrix} \tag{2.12}$$

and to introduce the concept of the R-matrix.

R-matrices are transfer matrices which transform a state vector according to $\boldsymbol{U}(s) = R(s|s_0)\boldsymbol{U}(s_0)$, where $R(s|s_0)$ is the R-matrix from s_0 to s. Generally,

$$\begin{bmatrix} u(s) \\ u'(s) \end{bmatrix} = \begin{bmatrix} A \cdot C(\sqrt{K}s) & B \cdot S(\sqrt{K}s) \\ -A\sqrt{K} \cdot S(\sqrt{K}s) & B\sqrt{K} \cdot C(\sqrt{K}l) \end{bmatrix} \cdot \begin{bmatrix} u(0) \\ u'(0) \end{bmatrix} \tag{2.13}$$

if $K \neq 0$, where C and S are the cosine and sine like terms from *Equation* 2.11. For this relationship to hold, boundary conditions must be set such that a state vector is not transformed without a displacement, hence $\boldsymbol{U}(0) = R(0|0)\boldsymbol{U}(0)$, and therefore $R(0|0) = I$, where I is the identity matrix. Due to this it is trivial to show that $A = 1$ and $B = \frac{1}{\sqrt{K}}$.

From this, it is possible to show that the R-matrices for focusing quadrupoles, drift spaces and defocusing quadrupoles are:

$$R(s|s_0) = \begin{cases} \begin{bmatrix} \cos(\sqrt{K}l) & \frac{1}{\sqrt{K}}\sin(\sqrt{K}l) \\ -\sqrt{K}\sin(\sqrt{K}l) & \cos(\sqrt{K}l) \end{bmatrix} & K > 0 : \text{focusing quadrupole} \\ \\ \begin{bmatrix} 1 & l \\ 0 & 1 \end{bmatrix} & K = 0 : \text{drift space} \\ \\ \begin{bmatrix} \cosh(\sqrt{|K|}l) & \frac{1}{\sqrt{|K|}}\sinh(\sqrt{|K|}l) \\ -\sqrt{|K|}\sinh(\sqrt{|K|}l) & \cosh(\sqrt{|K|}l) \end{bmatrix} & K < 0 : \text{defocusing quadrupole} \end{cases} \tag{2.14}$$

with l being the length of the element and k being given by ${}^{\frac{\partial B_y}{\partial x}}\!/_{p/e}$ in quadrupoles or ${}^{l}\!/_{\rho}$ in dipoles.

These R-matrices have several properties which make them particularly useful. First and most importantly, the R-matrix for a series of elements is simply the product of the individual-element R-matrices, so $U(s_n) = R_n \cdot R_{n-1} ... \cdot R_2 \cdot R_1 \cdot U(s_0)$. This enables the beamline to be considered as a series of individual components, each having a clear set of parameters which vary independently. Secondly, as the R-matrix can be calculated at any point along the beamline, it is possible to tune the strength of the magnets to ensure a specific beam configuration at a desired point. It is also important to remember that, in the absence of acceleration, as is usually the case in transfer lines, the determinant of an R-matrix must equal unity, to conserve the area of phase space. R-matrices also allow the simultaneous treatment of the vertical and horizontal planes by using a block-diagonal matrix of individual R-matrices for each plane, given by R_x and R_y. This matrix,

$$R(s) = \begin{bmatrix} R(s)_x & \mathbf{0} & \mathbf{0} \\ \mathbf{0} & R(s)_y & \mathbf{0} \\ \mathbf{0} & \mathbf{0} & I \end{bmatrix} = \mathrm{diag}(R(s)_x, R(s)_y, I), \tag{2.15}$$

then acts on the vector $\boldsymbol{X}$ defined in *Equation* 2.4.

Often, in the field of accelerator physics the R-matrix is parameterised in terms of Twiss parameters. This is called the Courant–Snyder parametrisation of the R-matrix and is equivalent to the direct use of the R-matrix formalism. In this thesis, the original R-matrix formalism is used, rather than the alternative Courant–Snyder parametrisation.

2.4 Design of Beamline Optics

R-matrices are the main mathematical tool used to design beamline optics, as these enable the beamline designer to produce optics with specific properties. Given a starting beam phase space $\wp_0$, it is often possible to produce a final phase space $\wp_f$ which matches the design specifications by tuning the value of specific elements in the R-matrix.

The example which most commonly arises when designing beamlines is, starting from a point-like particle distribution, to arrive at a focused beam, known as point-to-point focusing. Here, a point-like distribution is one where the spatial size of the object is much smaller than the angular size. This is done by varying magnetic field strengths in quadrupoles or drift distances between magnets until

$$R_{12} = 0 \quad \text{and} \quad R_{34} = 0, \tag{2.16}$$

such that

$$\begin{bmatrix} R_{11} & 0 & 0 & 0 \\ R_{21} & R_{22} & 0 & 0 \\ 0 & 0 & R_{33} & 0 \\ 0 & 0 & R_{43} & R_{44} \end{bmatrix} \cdot \begin{bmatrix} 0 \\ x'_0 \\ 0 \\ y'_0 \end{bmatrix} = \begin{bmatrix} 0 \\ x'_f \\ 0 \\ y'_f \end{bmatrix} \tag{2.17}$$

in both planes simultaneously. This minimises the size of the beam at the end of the beamline under the point-like source assumption. This is often used as secondary targets are assumed to produce particles as point-like sources, making this matching technique very widely applicable. Another common example is to produce parallel beams starting from a point-like source. In this case, the parameters which need to be matched to zero are R_{22} and R_{44}. While it is possible to simultaneously have several elements of the R-matrix equal to zero, it is important to remember that as a consequence of Liouville's theorem, the determinant of R must always be equal to unity, as such, for example, it is impossible to both have $R_{11} = 0$ and $R_{12} = 0$ at the same time.

2.4.1 Limits of First Order Calculations

This treatment and the results to which it has led have depended on the truncation of the higher order terms when deriving the equation of motion. What this translates to is that, in beamlines with large acceptances, be those positional, angular or momentum acceptances, when using the R-matrix formalism, the results will differ from those which have been obtained using particle tracking. Examples of the study and magnitude of these effects can be found in the literature [34].

These studies have found that when considering beamlines with momentum acceptances of over 10%, the errors arising from first order calculations may be larger than a factor 2 in the absolute value of the result. This means that while R-matrix formalism can be used to design the first iteration of optics, these must then be carefully assessed and optimised using specialised particle tracking codes if the acceptance of the beamline is expected to be large.

2.5 Chromatic Aberrations

The R-matrix formalism is analogous to the transfer matrix method used in conventional optics, with focusing or defocusing quadrupoles being akin to focusing or defocusing lenses [36]. In conventional optics, light of different frequencies finds a different refractive index in a lens, and hence rays can be focused at a different distance from the lens. Similarly, in beamlines, particles with different momenta are focused by different amounts in quadrupoles, again leading to different focal points. This happens because when a charged particle is travelling in a magnetic field, it is deviated more the lower its momentum, hence particles of a momentum greater than the nominal momentum are focused further away than desired and the opposite is true for particles of lower momentum.

This, in large circular machines such as the LHC, can be addressed and corrected using specially designed sextupole magnets, which counteract the effect of chromaticity. However, this is possible but difficult when using smaller machines and beamlines due to both space and budget constraints. Additionally, to make the effect of sextupoles significant, these must be placed at positions where the beam is largest in the plane which needs to be corrected and smallest in the other, again a condition which is often unattainable when working with smaller machines. Fortunately, the issue of chromaticity, is a much more significant issue when the beam is recirculating, rather than in single-pass machines, like a beamline.

In beamlines with a large momentum acceptance, chromatic aberrations cause off-momentum particles to focus at an incorrect position, and, often due to the convolution of geometric aberrations due to large angular acceptance, these particles are able to bypass collimation. These therefore arrive at the experiment, worsening the momentum resolution and increasing the size of the beam observed. This is generally undesirable, and must be carefully addressed with particle tracking codes, which will be discussed in *Section* 2.8.

As will be shown in the following chapters, strong collimation can counteract the size enlargement due to chromaticity. By removing more of these off-momentum particles, it is possible to maintain a smaller beam-spot size. Unfortunately, this may also have the unwanted consequence of removing some particles which are within the desired momentum band. This will be discussed in more detail in the following section.

In the framework of this thesis, the chromatic aberrations are studied but no corrective elements have been introduced in the design, since their effect was not deemed necessary to reach NA61/SHINE's requirements.

2.6 Momentum Selection and Momentum Resolution

Particles of different momenta are principally separated using dipole magnets. This is done by tuning the integrated strength of the magnet, Bl, such that it provides the deflection necessary for particles of the nominal momentum to follow the layout of the beamline, whereas off-momentum particles, which will be deflected more or less depending on their momentum, can be separated from the beam using a slit.

The deflection of off-momentum particles as a function of their momentum difference is given by [37]

$$\delta\theta_1 = -\frac{\delta p_0}{p_{ref}} \cdot \theta_1, \tag{2.18}$$

where θ_1 is the bend angle. This means that, after a distance L, this relative deflection is transformed in a separation, or *dispersion*, given by

$$\delta = L \cdot \delta\theta_1 = -\frac{\delta p}{p_{ref}} \cdot L\theta_1. \tag{2.19}$$

This is the starting point for the simple momentum analysis of beamlines, and has been used in the field for many years [37].

The key insight to be gained from this treatment is that if a particle beam has size $\pm\sigma$ at a certain position and there are off-momentum particles that have a $\delta(p_1) > 2\sigma$, then thse particles can be removed from the beam without affecting the on-momentum particles. The factor of 2 is necessary as *both* the on momentum and off momentum beams have a size of $\pm\sigma$. This leads to the minimum resolvable momentum offset, the smallest momentum acceptance which can be selected without losing *good* particles,

$$\left(\frac{\delta p}{p_{ref}}\right) = \frac{2\sigma}{L\theta_1} \tag{2.20}$$

and the closely related *intrinsic resolving power*,

$$P = \frac{1}{\frac{\delta p}{p_{ref}}} = \frac{L\theta_1}{2\sigma}. \tag{2.21}$$

This treatment shows the importance of three key parameters when attempting to maximise the resolving power P of a beamline. Firstly, the size of the beam σ must be minimised, secondly, the distance over which the dispersion is introduced must be maximised, and finally, the bending angle must, if possible, be maximised. The first parameter is a function of the optics used in the beamline, so this can always be optimised, whereas the latter two parameters are decided when the beamline is initially designed, and therefore cannot be changed once they have been selected [32].

It is also possible to derive the relationship between the collimator opening and the standard deviation of $\delta p/p_{ref}$ of all particles which are able to pass through a collimator if one assumes a thin collimator. By considering the position in the bending plane of a particle passing through a collimator to be given by

$$x = R_{16} \cdot \frac{\delta p}{p_{ref}} + \nu, \tag{2.22}$$

where ν is a random variable ranging from $-\sigma/2$ to $+\sigma/2$ to account for the finite size of the beam spot, one can relate the momentum offset to a particle's position

$$\frac{\delta p}{p_{ref}} = \frac{1}{R_{16}} \cdot (x - \nu). \tag{2.23}$$

Calculating the variance of Equation 2.23, one arrives at:

$$\begin{aligned} \mathrm{Var}\Big(\frac{\delta p}{p_{ref}}\Big) &= \mathrm{Var}\Big(\frac{1}{R_{16}}(x - \nu)\Big) \\ &= \mathrm{Var}\Big(\frac{x}{R_{16}}\Big) + \mathrm{Var}\Big(\frac{\nu}{R_{16}}\Big) \\ &= \frac{1}{R_{16}^2} \cdot (\mathrm{Var}(x) + \mathrm{Var}(\nu)). \end{aligned} \tag{2.24}$$

The variance of ν is given by the optics of the beamline and depends on the spatial distribution of on-momentum particles within the beam spot. On the other hand, the variance of x is simply given by the variance of a flat-top distribution between $\pm\frac{C}{2}$, where C is the full collimator opening. This distribution can be used if one assumes that the beamline's momentum acceptance is much larger than the momentum offset being transmitted through the collimator, and therefore, the number of particles with each value of $\delta p/p_{ref}$ is constant.

Putting together these results, and using the well known variance of a flat-top distribution, one arrives at the equation for the standard deviation of $\delta p/p_{ref}$ being given by

$$\mathrm{Std}\left(\frac{\delta p}{p_{ref}}\right) = \frac{1}{R_{16}} \cdot \sqrt{\frac{C^2}{12} + \mathrm{Std}(\nu)^2}. \tag{2.25}$$

2.6.1 Magnet Configurations for Momentum Selection

While only a dipole is necessary to introduce dispersion and a collimator can be used to remove the off-momentum particles, these are often not sufficient to perform momentum selection in a real-world application. In general, one must also recombine the separated beam, ideally completely removing the added dispersion, so that the particles which will reach the target will, to first order, have a position that is independent of their momentum. This can be done in several different ways.

Two-Bend Achromat

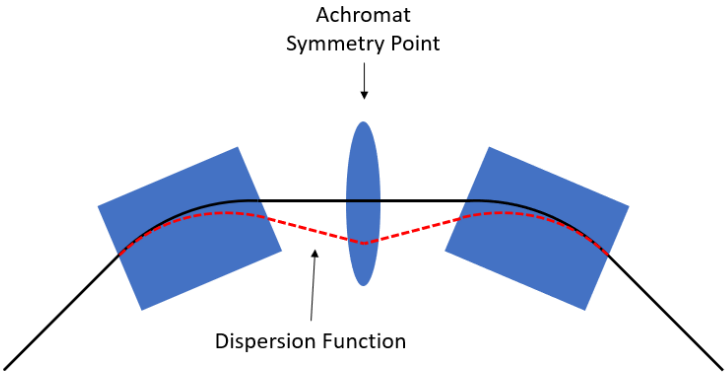

Figure 2.2: A two-bend achromat.

A two-bend achromat is the simplest system to introduce and later recombine dispersion in a beam while not introducing chromaticity. This layout, shown in *Figure* 2.2, has been extensively used in several machine designs [38]. It uses the first dipole to introduce dispersion, a quadrupole, called the *field lens*, to change the sign of the rate of change of dispersion, and the last dipole to then set this rate of change back to zero once the dispersion has been fully removed. To maintain the necessary symmetry, the optics upstream of the two-bend achromat are calculated such that in the bending plane, the beam is focused as close as possible as the field lens, where collimation can then take place.

In this design, the second dipole may be deflecting the beam in the same direction as the first dipole, useful for circular machines, but it can also be designed such that the dipole deflects the beam in the opposite direction, leading to a beam exiting the achromat with the same direction, albeit having been spatially displaced. In this design however, the number of field lenses must be increased to two.

Three-Bend Achromat

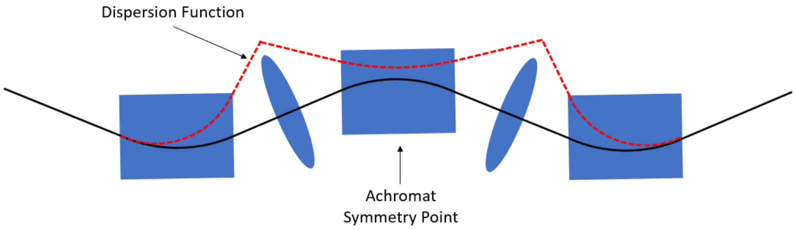

Figure 2.3: A three-bend achromat.

A three-bend achromat is comprised of three individual, identical bends tuned to the same magnetic field strength to introduce and later remove dispersion. An example of such a design is shown in *Figure* 2.3. Here, the optics upstream are again designed such that the beam's focal point is located in the middle of the central bend, again to ensure the symmetry of the construction. In this design, as the bends are alternating in direction, the outgoing beam is produced both at an offset and at an angle relative to the incoming beam.

Four-Bend Achromat

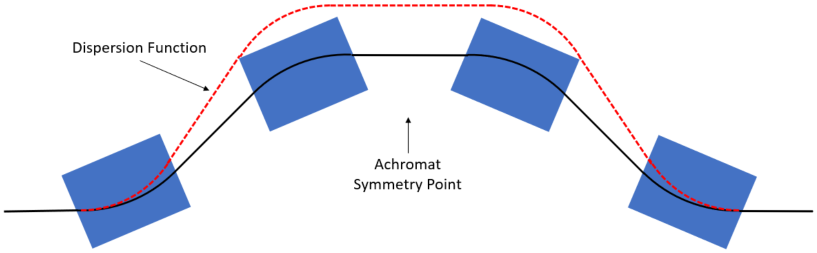

Figure 2.4: A four-bend achromat.

The four-bend achromat is another example of a system designed to perform momentum selection, Here, the dispersion is introduced between the first pair of bends, while it is recombined between the third bend and fourth bends. It is important to note that while the magnetic fields deflect particles in different directions, the magnitude of all the integrated magnetic fields must be the same.

This design does not use any quadrupoles, and the distance between the second and third dipoles can be decided by the beam designer, with the main consideration being the upstream optics and the dipoles' apertures. This provides flexibility on the location of the focal point required for momentum selection, as this only needs to be located between the second and third bends and is fully determined by the upstream optics. Further, an advantage of this configuration is that due to the intrinsic symmetry of the design, the beam exits the achromat travelling in the same direction as the original beam, unlike in the two-bend achromat and three-bend achromat designs.

2.7 Beam Interactions with Material

Particles travelling in a beamline will inevitably interact with material, be it some air remaining in the beam-pipe, detectors installed in the beam-path for particle identification, or beam windows used to seal the vacuum. These interactions may be categorised into three distinct types: elastic collisions with nuclei, inelastic collisions with atomic electrons, and inelastic collisions with nuclei, including the bremsstrahlung process [39].

The first of these, multiple Coulomb scattering, is caused by elastic collisions with nuclei, and leads to a significant, statistically-distributed, growth in the beam's angular size given by [39]

$$\theta_{rms} \approx \frac{13.6\text{ MeV}}{\beta c p} z\left(\frac{x}{X_0}^{0.5}\right)\left(1 + 0.38\,\ln({}^{x}\!/_{X_0})\right), \tag{2.26}$$

where p is the momentum, βc is the particle's velocity, z is the charge of the particle, x is the material's thickness, and X_0 is the material's radiation length. Values for these radiation lengths can be readily found in the relevant literature [40].

The area of phase space which the beam occupies, called the emittance of the beam, can be significantly increased by Coulomb scattering, especially in low-energy beams. This is an effect that is dependent on the distribution in phase space of the beam as illustrated in *Figure* 2.5. This often causes asymmetric emittance growth in the horizontal and vertical planes of the beam. Coulomb scattering can have a truly detrimental effect on otherwise well-designed optics, as such, the minimisation of material, especially those with a short X_0, is of great importance.

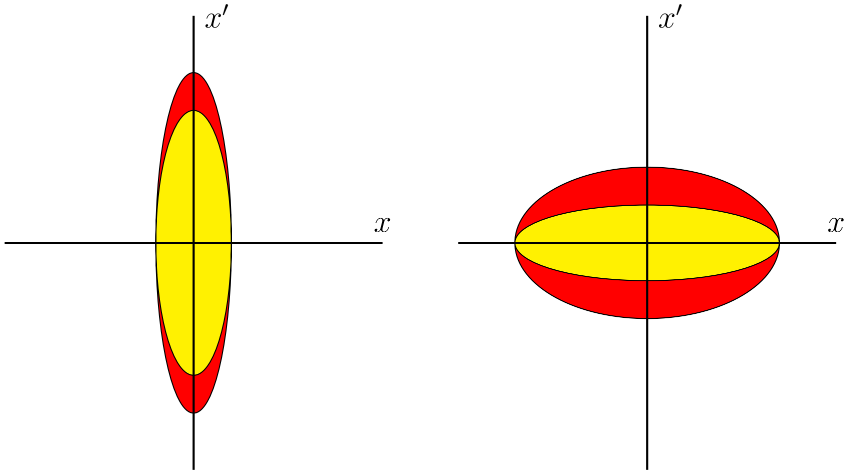

(a) (b)

Figure 2.5: The effect of Coulomb scattering on emittance on two initially congruent phase spaces. These initial phase spaces are shown in yellow, whereas after Coulomb scattering they are shown in red. If the size of the beam is minimised, as in (a), the emittance growth is minimised, whereas in (b) the emittance growth is much larger.

The interaction of beam particles with atomic electrons, on the other hand, leads to an energy loss in the beam, caused by the excitation of these electrons. This is essentially only a function of the density of the electrons encountered and is is given by

$$\frac{dE}{dx} \approx \eta \varrho, \tag{2.27}$$

where ϱ is simply the density of the material and η is a coefficient dependent on the material's atomic number and atomic weight [39]. The effect of this energy loss is minimal in beamlines as the densities encountered by the beam lead to negligible energy losses.

Finally, inelastic nuclear interactions lead to two effects. The first is bremsstrahlung, which is a process in which most often electrons or positrons interact with nuclei to produce γ-rays. This process's Feynman diagram is shown in *Figure* 2.6. These γ-rays may then in turn produce additional electron positron pairs, which can then produce more γ-rays and so on, leading to a an electromagnetic shower. The development of an electromagnetic shower takes place over a material's radiation length, X_0.

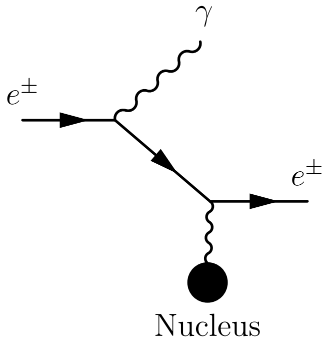

Figure 2.6: The Feynman diagram for bremsstrahlung production.

The second inelastic interaction with nuclei involves the hadrons in a beam and is mediated via the strong force. These interactions on average occur over an interval called the material's nuclear interaction length λ and involve a hadron from the beam interacting with a nucleus to produce a variety of secondary particles. The nuclear interaction length for many different materials is also readily available in the literature, for example in Ref. [41]. Secondary particles produced this way may then in turn also interact with the material, causing a hadronic shower. It is via this process that the majority of secondary beams are produced, via the interaction of a hadronic beam with a target to produce secondary particles.

2.8 Software Used for Beamline Design

The matching process rapidly becomes something which is far beyond the mathematical capabilities of one individual, and as such several specialised software codes have been developed over the years. The ones which are most commonly used at CERN are TRANSPORT [42] and MAD-X [43]. These have been thoroughly bench-marked [44, 45] and provide several tools without which beamline design would be significantly more challenging.

TRANSPORT, developed in the 1960s is a program which takes as input several 'cards', representing beamline elements, creates their corresponding R-matrix, and performs matrix multiplication to obtain the R-matrix of the whole beamline. Starting from an initial $\boldsymbol{X}$, TRANSPORT also describes the evolution of a ray and allows the user to perform matching. The user inputs a "vary card" with the target R-matrix element, its value and accuracy, and the program attempts to vary the user-defined free parameters to reach the target. The plotted output of a TRANSPORT routine can be seen in *Figure* 2.7.

MAD-X, on the other hand, is a much more modern program which provides not only more features but also a more user-friendly interface. As MAD-X has been designed specifically to address several challenges which arose when designing the LHC, the program excels in handling large accelerators. MAD-X provides all the tools which are present in TRANSPORT, such as matching, but also provides several additional utilities, most important among these being the module which enables particle tracking, the *polymorphic tracking code* (PTC) [46].

The main limitation when using MAD-X in the North Area is the fact that many of the beamlines there have been developed using TRANSPORT, and therefore many of the files describing the currently used optics and lattices were not available as a MAD-X input at the time when these studies were performed.

Another tool used in the design of beamlines is one which can simulate the actual particle interactions within the beamline and the elements. This is often done using GEANT4-based software, such as Beam Delivery Simulation (BDSIM) [47] or G4Beamline (G4BL) [48]. As the models for the existing H2 beamline are currently available in G4BL, this was the tool used during this DPhil; however, this choice is mostly a matter of taste.

G4BL is a Monte-Carlo based simulation software which performs particle tracking and simulations. It provides significant amounts of flexibility and has been used for several projects such as MICE [49], the Neutrino Factory [50] and in several North Area beamlines [51–53]. The program works by first allowing the user to define the beamline elements, their materials, fields (including user-defined field maps), etc., placing them into a *world*, and then performing the tracking of particles. This can be done using several different physics lists, different tracking steps and placing user-defined cuts on particle energies. This enables a significant flexibility in the choice of the trade-off between accuracy and computing time. A significant advantage of G4BL is the visualisation, as the program allows for a full 3D visualisation of the beamline.

Finally, FLUKA [54–56] is a general purpose Monte-Carlo software designed for calculations of particle transport and interactions with matter commonly used in the field. This tool is the most often used software in the field to assess the radiation produced by a beamline, in terms of ambient dose produced, activation, energy deposition, and particle fluxes. To attain the highest precision achievable while also maintaining a rapid computation time FLUKA uses several interaction models at different energies to best model the physical processes taking place. As with all the previously described software, FLUKA too has been used over many years, with many of its results having been verified [57, 58]. FLUKA is often used in conjunction with a separate graphical interface, called FLAIR [59].

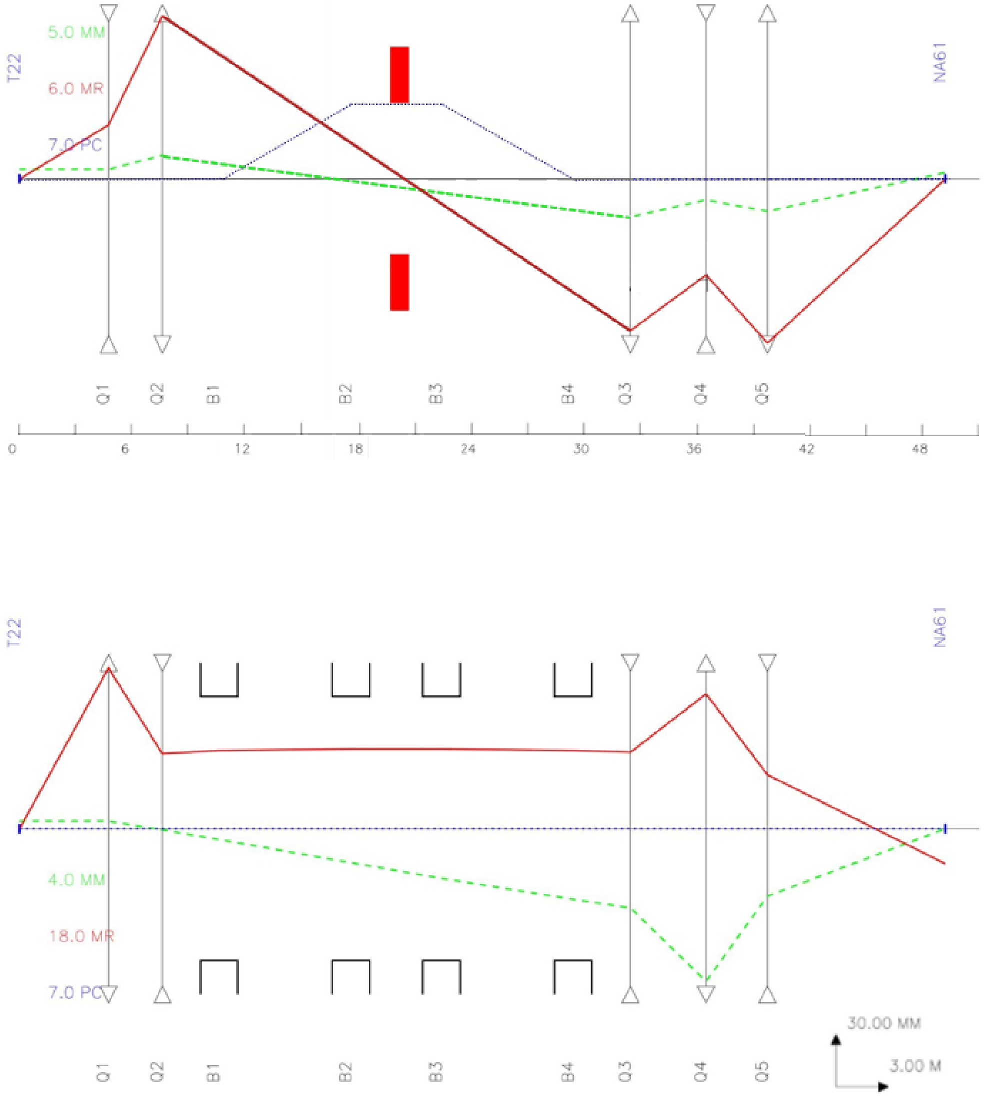

Figure 2.7: An example of a TRANSPORT routine's output, showing the R-matrix elements in the horizontal plane (*top*) and in the vertical plane (*bottom*). R_{11} and R_{33} are plotted in *green*, R_{12} and R_{34} are plotted in *red*, and R_{16} and R_{36} are plotted in *blue*. The green and red plots are also called the *sine ray* and *cosine ray*, representing the motion of a particle with initial conditions of $\boldsymbol{X} = (0, 1)$ and $\boldsymbol{X} = (1, 0)$ respectively.

Chapter 3

Target Optimisation Studies

This chapter describes the process via which the secondary targets used in the low-energy beamline have been optimised. It also describes the assumptions, simulations, and analysis performed. Finally, a section comparing the results obtained using several different simulation packages and a discussion of the reliability of the simulations is included.

3.1 Production of Secondary Particles

Simple models and phenomenological formulae have been developed over many years to describe the processes involved in the production of secondary particles. While these are not commonly used, with researchers usually relying on Monte-Carlo techniques, a general understanding of particle shower formation is quite useful to obtain an intuition for these otherwise complex processes.

3.1.1 Simple Models

The simplest way to conceptualise the production of secondary particles is to begin with a model for the formation of electromagnetic (EM) showers and then to expand upon this to include hadronic showers and obtain a qualitative understanding of secondary particle production. This qualitative understanding is fundamentally incomplete, and most models used nowadays are purely phenomenological and based on a limited number of cross-section measurements, however, it still provides a useful framework and starting point for discussion and analysis.

The simplest model for EM showers is Heitler's model [60], illustrated in *Figure* 3.1. Here, electrons interact via bremsstrahlung and produce photons, which in turn produce e^+e^- pairs. This takes place every *radiation length*, X_0 as long as the particle's energy is above a certain threshold. It is assumed that the energy is divided equally between each secondary particle. Clearly, the number of particles doubles each radiation length,

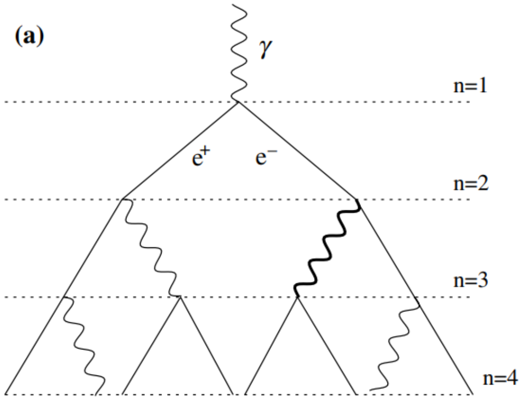

Figure 3.1: Representation of (a) Heitler's model, and (b) Matthews' extension to include hadronic showers. Image from Ref. [61].

meaning that after n radiation lengths, 2^n particles will be present. While this model does not take into account all processes taking place, it does provide reasonable estimates for the total number of particles and the relation between the depth of the shower and the initial energy.

This model was then expanded by Matthews [61] to include hadronic interactions in air showers. Here, an initial proton interacts with some material and produces several secondary pions which will in turn interact and continue the shower. The π^0 produced are assumed to decay immediately to a pair of photons which then behave identically to those in Heitler's model. On the other hand, the $\pi^\pm$ travel a certain distance, called the *nuclear interaction length*, λ_n, after which they again interact with other particles in the target producing subsequent showers. The energy in this model is assumed to be divided equally between π^+, π^-, and π^0, the latter of which decays into two photons, meaning that $1/3$ of the energy goes into EM showers. Again, these showers persist until each particle has an energy smaller than the critical energy. This model provides a good estimate for the hadronisation which takes place in secondary targets, but as it was developed to handle air showers it lacks key processes, such as re-absorption and the production of heavier secondaries. To tackle these, one has to rely on phenomenological models.

3.1.2 Phenomenological Models and Monte-Carlo Techniques

Phenomenological models are useful as they do not need to account for the full complexity of the secondary production via hadronisation processes of a high-energy, high-intensity proton beam impinging on a target, as these rely fully on data to provide relatively simple formulae which can be used to estimate these yields. One of these empirical formulae is called the *Atherton parametrisation* and comes from the NA20 [62] experiment. It can be used to characterise the production of $K^{\pm}$, $\pi^{\pm}$ and $p\bar{p}$ in thick beryllium targets for beams with momenta in the range 60 to 400 GeV/c impinging on Be targets and is often used to estimate the composition of beams produced in the North Area. These formulae, along with the respective values of the free parameters can be readily found in Ref. [62] and Ref. [27]. Several other parametrisations are also available, for example that developed by NA56/SPY [63], however they all have the same limitation in extrapolating beyond the dataset used to originally generate the model, be it for different primary energies, different materials or different geometries, and so overall, the utility of these models is strongly dependent on the use-case.

For these reasons, the main technique to estimate the particle yield of secondary targets is via Monte-Carlo simulations. As shown in *Figure* 3.2 [29], there is a large number of cross section measurements at different energies and for different particles which can be used to accurately simulate both the hadronic and electromagnetic interactions of particles with matter and subsequent showers produced. These simulations offer significant flexibility on the type of geometries, materials, and energies which can be simulated, and can predict yields accurately to within 10% of the real particle yields [64]. While this means that results obtained this way may not be suitable for all applications, this is perfectly adequate for understanding general trends in target performance and selecting an appropriate secondary target for beamlines.

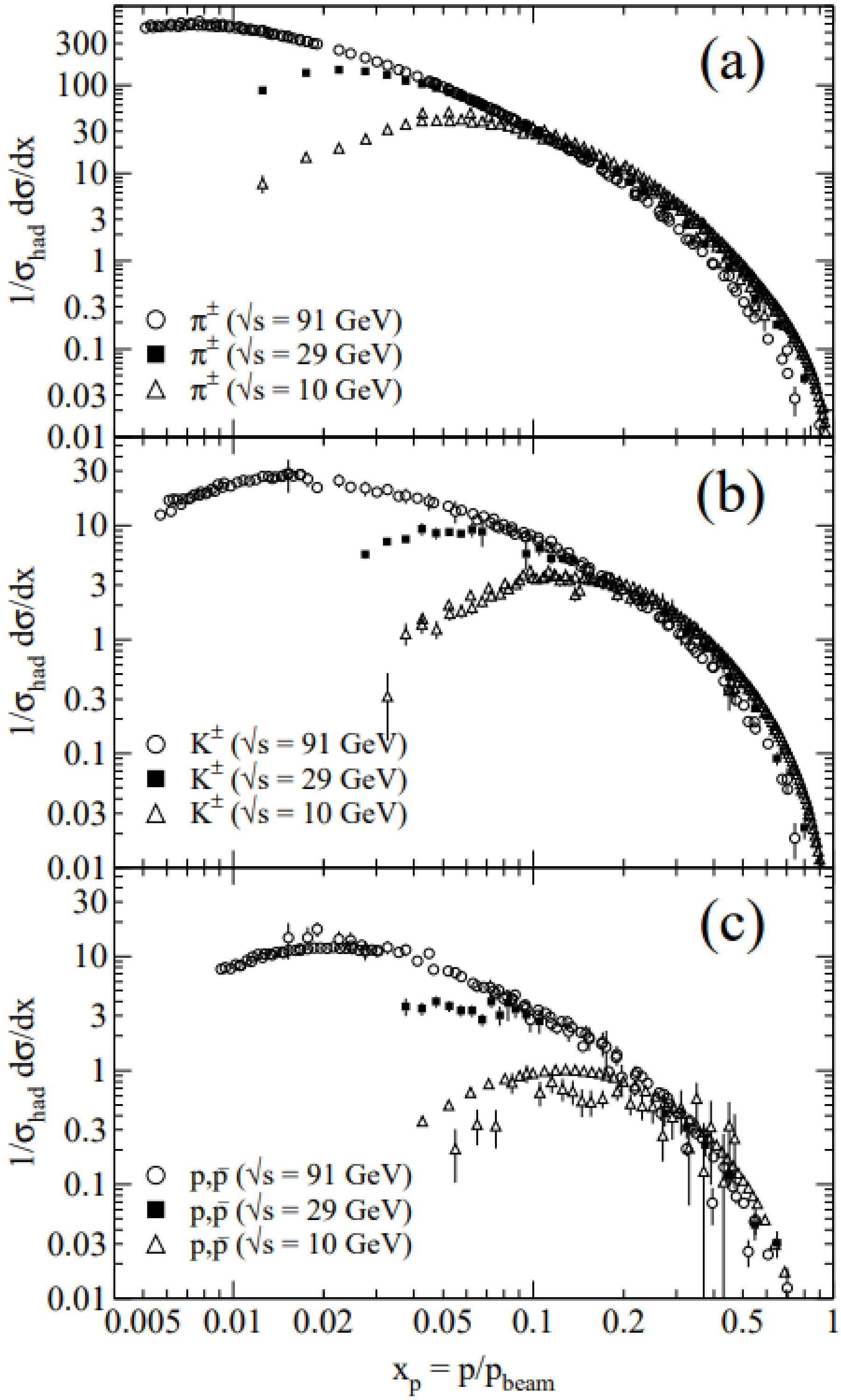

Figure 3.2: Scaled momentum spectra of (a) $\pi^{\pm}$, (b) $K^{\pm}$, and (c) $p\bar{p}$ at $\sqrt{s} = 10, 29, 91$ GeV. In the case of the low-energy beamline $\sqrt{s} \approx 27$ GeV, while x_p is between 0.005 and 0.035

3.2 Simulations of the Targets

The first step in designing the newly proposed beamline was to optimise the target which will be used to produce the low-energy particles. To do this, extensive simulations have been performed to maximise the particle yield while minimising the number of leptons present in the beam.

3.2.1 Overview of the Simulations

G4Beamline (G4BL), has been used to simulate the expected particle flux and beam composition which is produced by various targets using different primary beams. These simulations have been performed on a range of targets which have either been previously used at CERN or have shown significant potential for providing the desired particle rates. The materials studied include both low-Z targets, such as carbon and beryllium and high-Z materials, such as copper and tungsten. For each of these, a range of lengths and radii have been investigated, to study their effect on the yield and beam composition. Additionally, large importance has been given to optimising the momentum of the impinging beam. This parameter has been varied from values as low as 70 GeV/c to the SPS's maximum momentum of 400 GeV/c.

The H2 beam line is able to transport either the primary 400 GeV/c SPS beam or various secondary beams, as described in Section 1.1.2. As the latter are produced via the interaction with a Be target in TCC2, secondary beams have a mixed composition of pions, protons and kaons, and the ratios of these particles varies with the beam momentum. These changes in composition can be accounted for by using the Atherton parametrisation, given by,

$$\frac{d^2N}{dpd\Omega} = \begin{cases} \mathrm{A}\left(\frac{\mathrm{B}}{p_0} e^{\frac{\mathrm{B}p}{p_0}}\right)\left(\frac{\mathrm{C}p^2}{\pi} e^{-\mathrm{C}(p\theta)^2}\right) & \text{for } K^{\pm},\ \pi^{\pm}, \text{ and } \overline{p}, \\ \mathrm{A}\left(\frac{\mathrm{B}+1}{p_0}\left(\frac{p}{p_0}\right)^{B}\right)\left(\frac{\mathrm{C}p^2}{\pi} e^{-\mathrm{C}(p\theta)^2}\right) & \text{for } p \\ \mathrm{A}\left(\frac{\mathrm{B}}{p_0} e^{\frac{-\mathrm{B}p}{p_0}}\right)\left(\frac{\mathrm{C}p_0^2}{\pi} e^{-\mathrm{C}(p\theta)^2}\right) & \text{for } e^{\pm} \end{cases} \tag{3.1}$$

The parameters A, B, and C used in this parametrisation vary for each individual particle species and can be found in Ref. [27].

Using this formula, the expected secondary beam composition can be calculated over a range of momenta. This can be seen in *Figure* 3.3.

To increase the number of relevant target interactions that could be simulated in a reasonable time, thereby reducing statistical uncertainties, secondary particles with a momentum lower than 500 MeV/c have been suppressed. This significantly reduces the time taken to complete each simulation while not affecting the results, as these low-energy particles would not reach the NA61/SHINE experiment due to the momentum selection station present in the beamline.

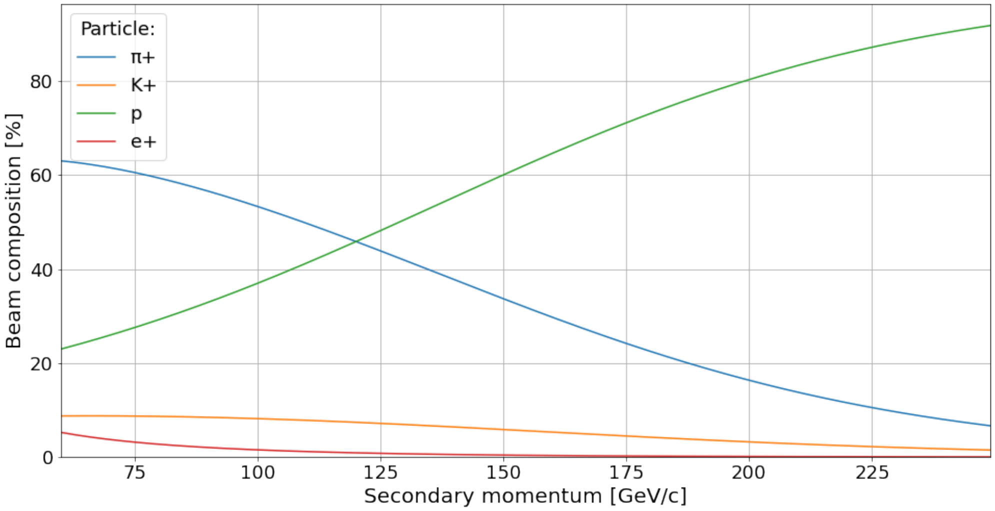

Figure 3.3: The expected percentage composition of the secondary H2 beam as a function of secondary beam momentum. It has been assumed that this beam was produced by the interaction of a 400 GeV/c primary proton beam impinging onto a long beryllium targets.

3.3 Results of the Target Studies

Many different parameters have been simulated to find the optimal targets:

- The target material, which included: carbon studied in two different forms, beryllium, tungsten, and copper.
- The target length, ranging from 20 to 130 cm for low-Z materials and from 10 to 40 cm for high-Z materials, $\approx 0.5\lambda_n$ to $\approx 4\lambda_n$.

- The target radius, ranging from 15 to 30 mm.
- The primary beam momentum. Beams of 70, 100, 150, 200, 250, 400 GeV/c momenta were investigated.

These studies were performed using 10^6 particles impinging on each target, with those either being primary protons, or secondary particles produced in TCC2 in the ratios described in Section 3.2.1. The results of the simulations have then been normalised to secondaries per primary particle, in order to be easily scaled for different possible intensities. Additionally, a decay distance of 50 m has been assumed, appropriately scaling down the number of particles expected at the NA61/SHINE target.

All simulations have been carried out using the FTFP_BERT physics list [65], a comprehensive set of models that encapsulate particle interactions and decay processes, used for accurately simulating several physical phenomena in the low-energy regime.

3.3.1 Comparison of Different Targets and Beam Parameters

As different targets produce beams which are very different in both rate and composition, optimising the target's material and shape has proven to be one of the key tasks in the DPhil. The differences in production yields arise mainly from two factors: first, the density of the material. The denser a material is, the higher the likelihood of an interaction, and so, the higher the yield of secondary particles. Secondly, the atomic charge of the various elements significantly affects the production of secondaries. This is due to a higher Z affecting both the likelihood of interaction and also increasing the intensity of effects such as bremsstrahlung. For brevity, only results for particles produced within a ±10% momentum band centred around 2 GeV/c and 13 GeV/c are shown in the following sections, however more momentum values have been studied. The results of these further studies can be found in Appendix A. Only the minimum and maximum momenta of interest have been shown here to bring to light as much as possible the differences in the distributions, providing a good overview of the results.

Before introducing the results of these simulations, it is important to address the error bars in the following plots. As discussed earlier, there are significant uncertainties in the production cross-sections of secondary hadrons in the 1 - 13 GeV/c momentum range - which in no small part have led to the development of this very low-energy beamline. These uncertainties are estimated to to be in the $\approx 10 - 20\%$ range [66]. Due to this, throughout the simulations in this chapter, a systematic ±10% error has been assumed for all these results. Fortunately, as these are systematic errors, while the overall particle rates estimated in the simulations may be wrong, they will be wrong by a *consistent* amount. This means that the results will be useful for selecting targets to be used by NA61/SHINE as we are only interested in overall trends in particle production. Due to this, while these errors are somewhat large, they are not expected to affect the outcome of the optimisation.

In the upcoming sections, what is presented is not the total number of particles produced by each target, but rather the number of particles that are expected to reach the *end* of the beamline. Hence, all particles produced are subjected to several acceptance cuts, which can be performed in different ways and will be discussed in more depth in Section 3.3.4. The cuts used for this analysis are ones that closely match the phase space that is accepted in the low-energy beamline for NA61/SHINE, discussed in depth in Chapter 4 and Chapter 5. These cuts are, defined at the end of the target, a positional acceptance of ±35 mm in the horizontal plane and ±8 mm in the vertical plane, and angular cuts of ±7.5 mrad in the horizontal plane and ±25 mrad in the vertical plane.

Effect of Primary Beam's Momentum on Particle Production

The primary energy of the beam, as stated earlier, has been simulated from as low as 70 GeV/c up to 400 GeV/c. This range has been chosen as it best matches the capabilities of the SPS's beam delivery and attempts to cover well the range of momenta from *Figure* 3.2 that is expected to optimally produce secondary hadrons in the low-momentum range. The results for 20 cm long high-Z targets with a 2.5 cm radius and 70 cm long low-Z targets with a 2.5 cm radius can be seen in *Figure* 3.4a which shows how the primary beam momentum affects the rate of hadron production at 2 GeV/c for a selection of high-Z and low-Z materials, and in *Figure* 3.4b which shows the same plot for hadrons produced at 13 GeV/c. These plots show both the yield of particles per particle on target, and the composition c_i of particles in the beam, defined as $c_i = 100 \times \frac{n_i}{N_{\text{tot}}}$, where n_i is the number of particles of species i and N_{tot} is the sum of the number of positively charged hadrons and positrons.

As these plots clearly show, higher energies correspond to higher particle rates, one of NA61/SHINE's key requirements. Unfortunately, higher momenta also correlate with higher $e^{\pm}$ background rates, as shown by the lower overall hadronic composition of the beams as the impinging beam's momentum increases. This highlights one of the challenges of this optimisation, a higher particle rate generally implies a larger leptonic component of the secondary beam. Further, one can see that generally high-Z materials are preferable both in terms of rates and in terms of overall beam composition, with tungsten being the overall best performing material.

Effect of Target Length on Production Yield and Composition

The effect of the target length on the beam is more complex. This is because as the length of the target is increased, the beam rate increases, until a maximum is reached, followed by a drop in the intensity of the secondary beam due to reabsorption. At the same time however, the beam composition changes, with the ratio of hadrons to all particles changing drastically. This means that while it is relatively straightforward to find the length which corresponds to the highest rate, it is not clear whether this will provide the beam with the optimal composition. Another difficulty is that, as shown below, as the energy of the secondary particles changes, the composition of the beam also changes. This means that a target that may have been optimal for producing particles at one energy, may not be adequate at other energies. These effects can be seen in *Figures* 3.5a and 3.5b for 2.5 cm radius targets using a 400 GeV/c primary beam.

As expected, higher Z materials had a peak in production at much shorter distances than low-Z materials, while also producing beams with a more desirable composition. On the other hand, low-Z targets appear to produce slightly more particles at higher energies;

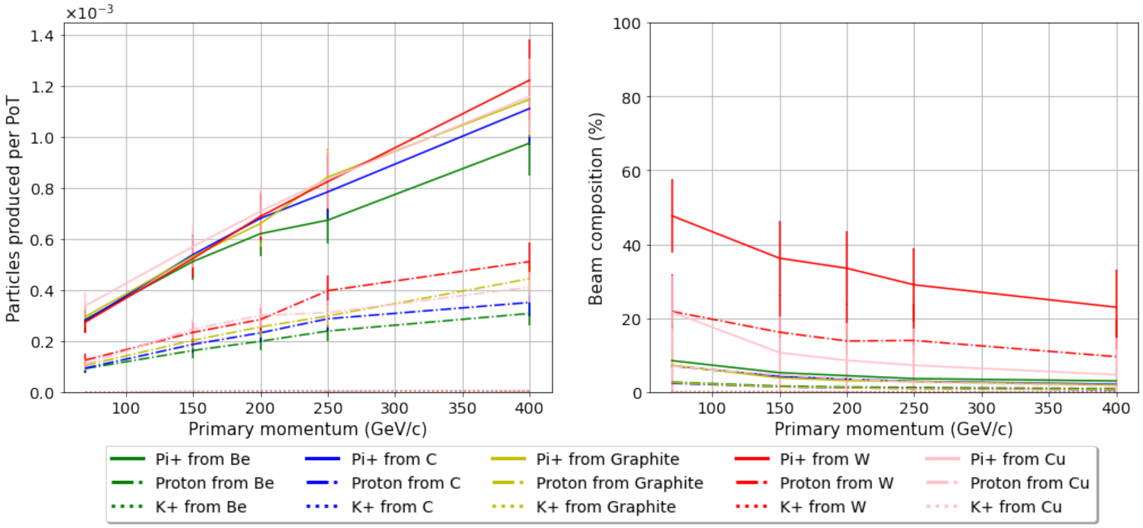

(a) Hadrons produced at 2 GeV/c (±10%).

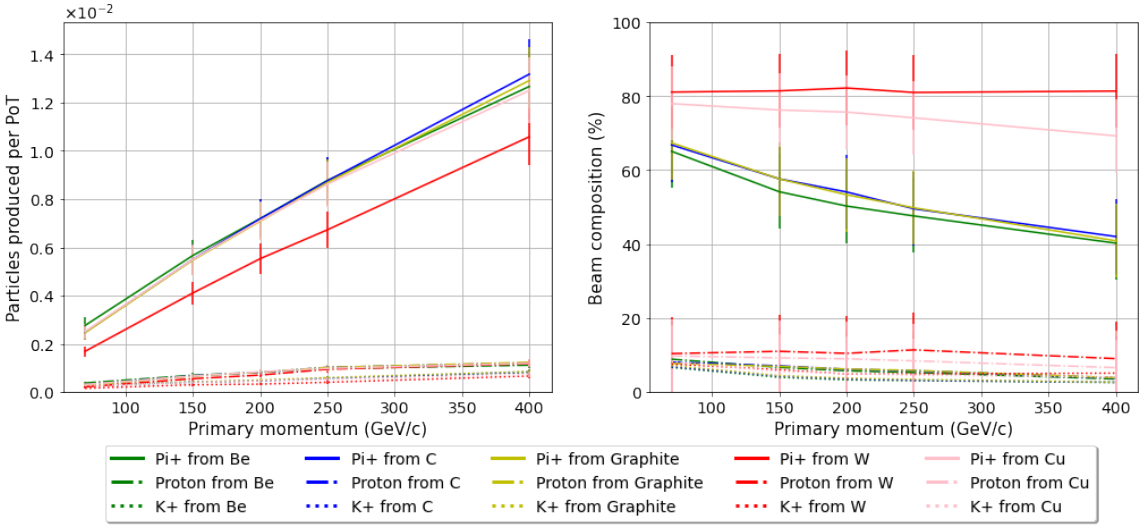

(b) Hadrons produced at 13 GeV/c (±10%).

Figure 3.4: Effect of primary momentum on hadron production from targets made of several different materials. *Left*: The number of hadrons produced per particle on target as a function of primary momentum. *Right*: The beam composition reaching the end of the beamline as a function of primary momentum, not shown is the positron content.

however this is within G4BL's uncertainties.

Effect of Target Radius on Production Yield and Composition

On the other hand, it was found that the radius of the targets has a small effect on the intensity of the secondary beam and does not affect at all the composition of the beam. This was found for the secondary beam at both 2 GeV/c and for that at 13 GeV/c, as can be seen in *Figures* 3.6a and 3.6b for 20 cm long high-Z targets and 70 cm long low-Z targets, using a 400 GeV/c primary beam. This makes the choice of radius to be used a rather straightforward one, as there are no physics based downsides in using a 30 mm target. While there may be other factors, such as availability of the targets or cost which may have an effect on the target choice, it is unlikely that they will play a significant role in the selection. The fact that the target's radius does not have a significant effect on the secondary beam likely arises from the fact that the beam-size of the primary is much smaller than the size of the target, and so any changes in the latter have a tiny effect.

3.3.2 Selection of Optimal Targets

There are many different parameters one can optimise for: hadron rate, hadron composition, number of particles at high energies, at low energies, or any combination of these, and this makes it difficult to define a single figure of merit. For this reason, we decided to select several targets which could perform optimally depending on the type of beam required by NA61/SHINE.

To do this all targets t have been given several rankings R_{ijkt} based on their percentile performance. The index i accounts for the differences in rankings arising from producing different hadrons, be it a pion, a kaon or a proton. The index j accounts for the performance at different secondary beam momenta and takes values of 2, 6, 8, 10, or 13 GeV/c and finally, the index k accounts for the differences in ranking for targets when considering either the overall yield of a specific hadron or the percentage of the beam that it makes up. These rankings were used to obtain an overall score for each target $\mathcal{S}_t$ given by $\mathcal{S}_t = R_{ijkt}w_iw_jw_k$, where w_i is the weight assigned to a specific hadron, w_j is the weight of a specific momentum and finally w_k accounts for whether we give more or less

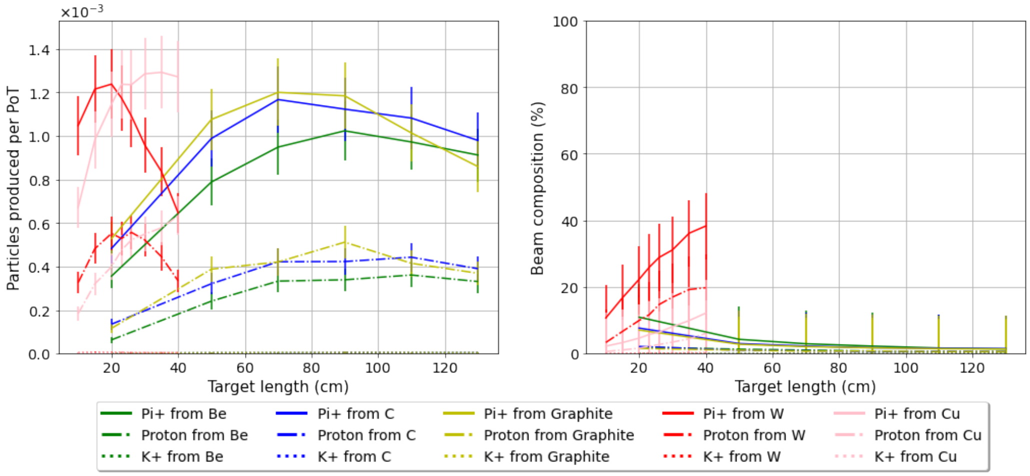

(a) Hadrons produced at 2 GeV/c ($\pm 10\%$).

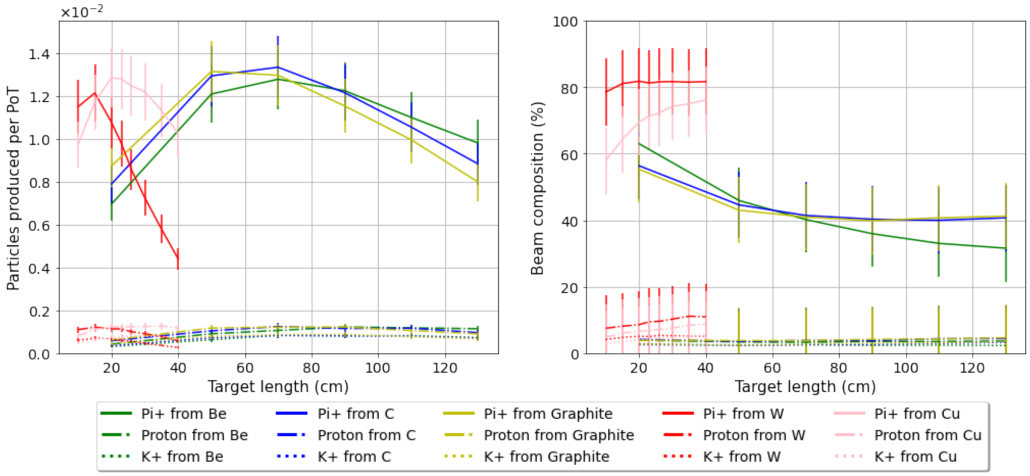

(b) Hadrons produced at 13 GeV/c ($\pm 10\%$).

Figure 3.5: Effect of varying the length of several targets on both the hadronic yield and the beam composition. *Left*: The number of hadrons produced per particle on target as a function of target length. *Right*: The beam composition reaching the end of the beamline as a function of target length, not shown is the positron content.

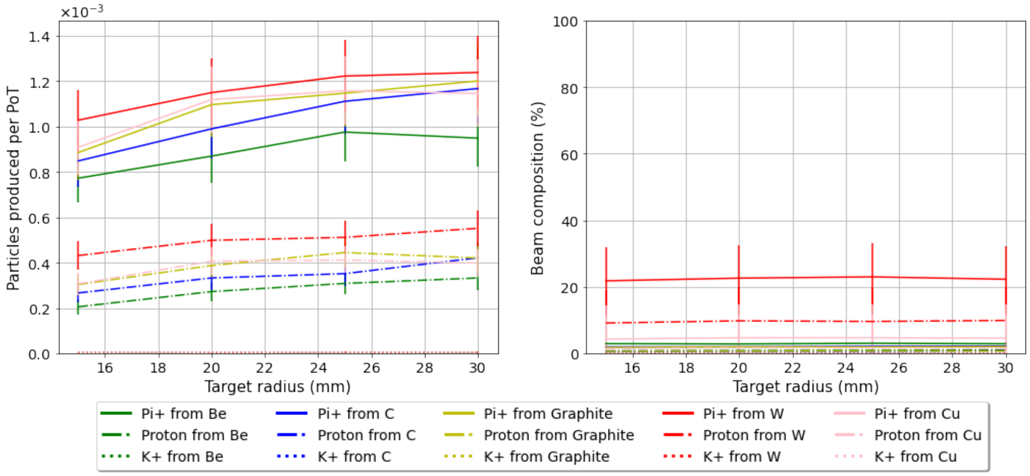

(a) Hadrons produced at 2 GeV/c ($\pm 10\%$).

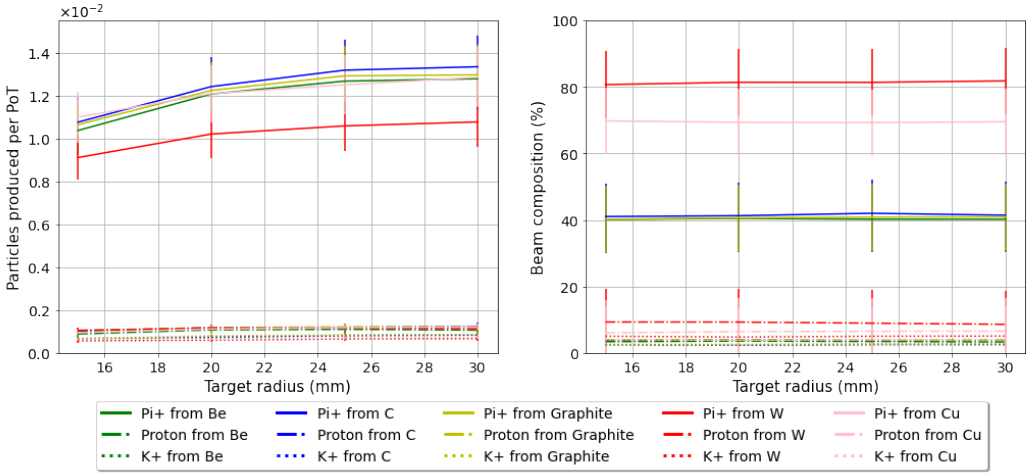

(b) Hadrons produced at 13 GeV/c ($\pm 10\%$).

Figure 3.6: Effect of varying the radius of several targets on both the hadronic yield and the beam composition. *Left*: The number of hadrons produced per particle on target as a function of target radius, *Right*: The beam composition reaching the end of the beamline as a function of target radius, not shown is the positron content.

importance to the overall rate or the hadronic composition of the beam. The target with the highest score is deemed to be the optimal target for a given requirement.

To enable the flexibility that the experiment will require, different optimal targets have been selected. As the target switching station, described in Section 3.4, can hold up to three targets, three targets were chosen. These have been designated the high yield target, the composition target and finally the balanced target. The high yield target maximises the particle rates at all momentum ranges. For this, w_k was changed to have a value of 0.7 for yield rankings and 0.3 for composition rankings. On the other hand, the composition target has been selected by inverting these weights, emphasising beams with fewer leptons, while giving less importance to the overall rate. Finally, for finding the balanced target w_k was set to 0.5 for all beam types. While w_i and w_j have not been used during this selection, the flexibility provided by this framework may prove to be useful in the future, as it may be possible that NA61/SHINE will require different targets to optimise for low energy particles.

Target name	Target material	Target length (cm)	Target radius (mm)	Beam momentum (GeV/c)
High yield	Tungsten	20	30	400
Hadron composition	Tungsten	26	30	400
Balanced	Tungsten	30	30	400

Table 3.1: Final selection of optimised targets for the newly proposed H2 Low-Energy beamline.

The optimal targets based on this method were all tungsten targets, with slightly different properties, listed in *Table* 3.1. The performance of these, both in terms of particle rates at different energies and of beam compositions at different energies can be seen in *Figure* 3.7. The different targets behave differently, as expected, with the high yield target always having the highest particle rates and the composition target always having the highest proportional hadron content, with a difference of approximately 5%

compared to the high-yield target.

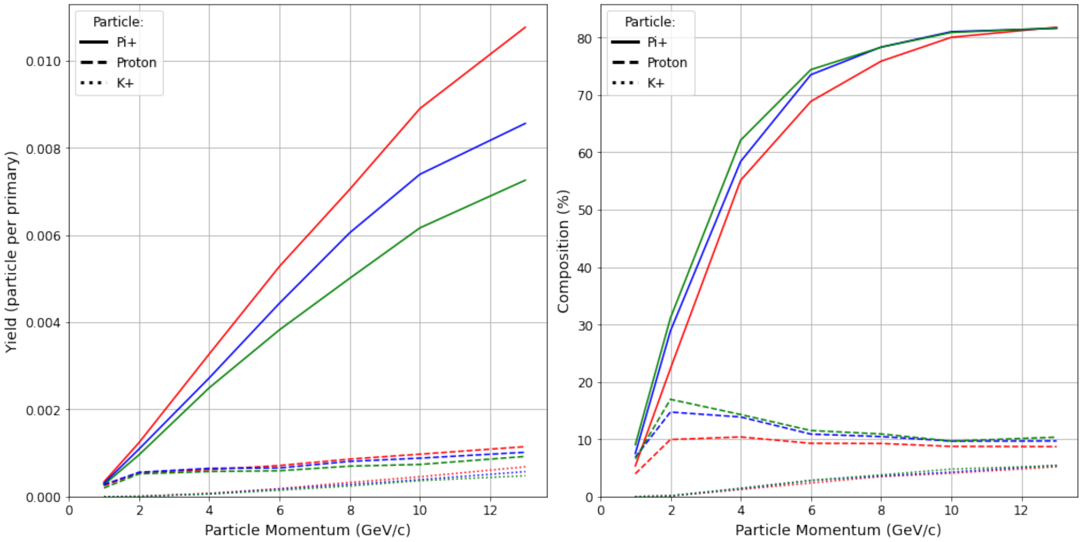

Figure 3.7: The performance of the three optimal targets, each shown in a different colour. The high yield target is shown in red, the hadron composition target is shown in green, whereas the balanced is shown in blue. For each target, the plot shows: on the *left* the secondary yield per primary particle as a function of secondary momentum and on the *right* the beam compositions as a function of secondary momentum. In this plot, the previously discussed ≈ 10% errors should be assumed on the particle yields.

3.3.3 Phase Space Occupied by Particles

The spatial and angular distribution of the secondary particles which were produced is important as it provides an insight as to whether the assumptions of a point-like target can be considered valid. These distributions in turn dictate the matching conditions one ought to use, as described in Section 2.4. It is also important to investigate the differences in production for each particle, especially to assess how different the angular production of hadrons and leptons is.

The results of these studies can be found in *Figure* 3.8a for particles with a 2 GeV/c momentum and in *Figure* 3.8b for particles at 13 GeV/c momentum. Both of these plots include particles with an initial momentum within a ±10% momentum band of the nominal momentum. For simplicity, only the phase-space distribution in the horizontal plane has been included; however due to the rotational symmetry right after the target, the results for the vertical plane would be identical.

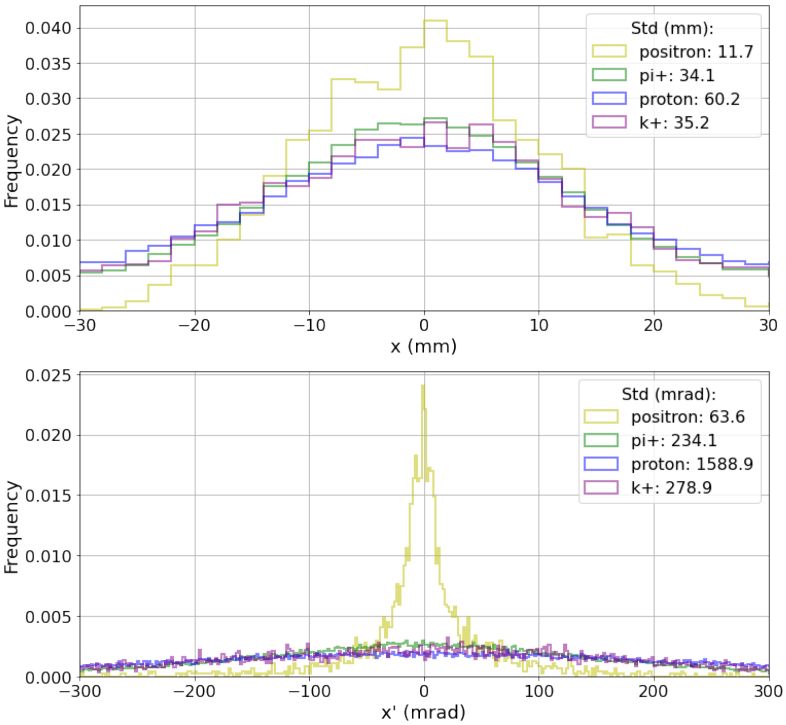

(a) 2 GeV/c (±10%)

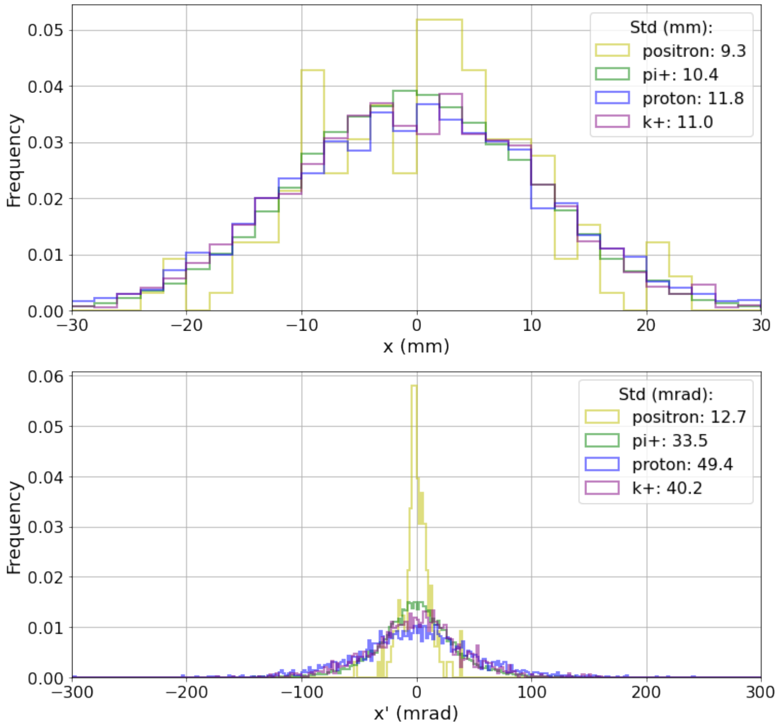

(b) 13 GeV/c(±10%)

Figure 3.8: Histograms of the (*top*) position and (*bottom*) angle at which particles are produced in a tungsten target in the horizontal plane. This is shown for (a) 2 GeV/c and (b) 13 GeV/c. As the energy is decreased, the distribution is clearly not point-like.

As can clearly be seen from these plots, and in agreement with the theory described in Section 3.1, the angular distribution of secondary particles is larger as the energy is decreased. Additionally, it is clear that secondary hadrons and secondary positrons from the primary beam have different angular distributions.

The narrow angular distribution of the electrons and positrons can be explained by kinematics. As described in the Matthews model, around one third of the energy from a hadronic shower can be expected to produce π^0 which then decay into two photons, initiating EM showers. It can be shown that the maximum opening angle between the two photons produced in the pion decay is given by $\sin(\theta) \approx m_\pi/(2E_\gamma)$ [67]. As we are using beams of energies in the order of tens or hundreds of GeV and because pair production is dominated by the highest-energy photons, produced by the highest-energy π_0, it is safe to assume that the energy of the photons is much larger than the rest energy of the pion, meaning that the opening angle of the photons will be extremely small with respect to the direction of travel. These photons then produce electron-positron pairs which are also focused in the forward direction to conserve momentum, leading to the narrow $e^\pm$ beams observed.

On the other hand, protons are produced with a broader distribution than the other secondary particles. This is because the majority of these particles are in fact not secondary particles produced by interactions within the secondary target, but are simply primary particles that have interacted via elastic scattering and have lost energy. This can be seen by comparing the yields of protons and anti-protons in simulation. If the protons were produced in proton-antiproton pairs, we would expect roughly the same number of these, however, we find that there are approximately 50 times more protons than antiprotons. Since these particles are simply slowed down in the target, they are subject to Coulomb scattering, which increases the angular distribution according to Equation 2.26.

For all these secondaries it is clear that in this low-energy regime, the distribution of particles is rather broad in both position and angle. What this implies is that neither a point-like target nor a parallel beam are ideal assumptions for the initial conditions of the beam.

3.3.4 Varying the Selection Cuts

When selecting the optimal targets and counting the number of particles produced, it was important to only consider those which would reach the end of the beamline. As discussed earlier, this required the use of acceptance cuts. The earliest used, pre-dating the design of the low-energy beamline, were some simplistic angular acceptance cuts. With these, if particles were outside a cone of a half aperture of 20 mrad once they reached a first quadrupole, assumed to be 50 cm downstream, they were assumed to be lost, otherwise, it was assumed that these would reach the end of the beamline. These geometrical cuts were a very first estimate to perform an initial optimisation, with an assumption of a beamline's acceptance based on previous low-energy secondary beamline designs. After the completion of the beamline design, these cuts have been revisited in order to correctly reflect the performance of the low-energy beamline. These cuts have been discussed in the previous section. With these cuts the actual beamline acceptance has been considered and therefore will provide the most accurate estimate of particle rates without simulating the whole beamline. These two different acceptance cuts can be seen in *Figure* 3.9, superimposed on the phase-space distribution of particles from two targets, and clearly they are quite different. [1]

A question which naturally arises is whether these two different cuts may affect which target is chosen by a designer. More specifically, if the ratios of particles accepted via the two different cuts are consistent. *Figure* 3.10 shows the number of particles accepted after the original cuts as dashed lines, whereas the solid line shows those numbers for the new acceptance cuts. What these show very clearly is that there is a strong dependence

---

[1] The shape of the original acceptance cuts, shown in green, can be explained by the fact that these are in fact positional cuts done at a distance of 50 cm from the target. If these cuts are then transformed via the matrix

$$T = \begin{bmatrix} 1 & -d \\ 0 & 1 \end{bmatrix} \tag{3.2}$$

where d is the distance between the target and the magnet, they are simply sheared backwards, giving the cuts shown in the image.

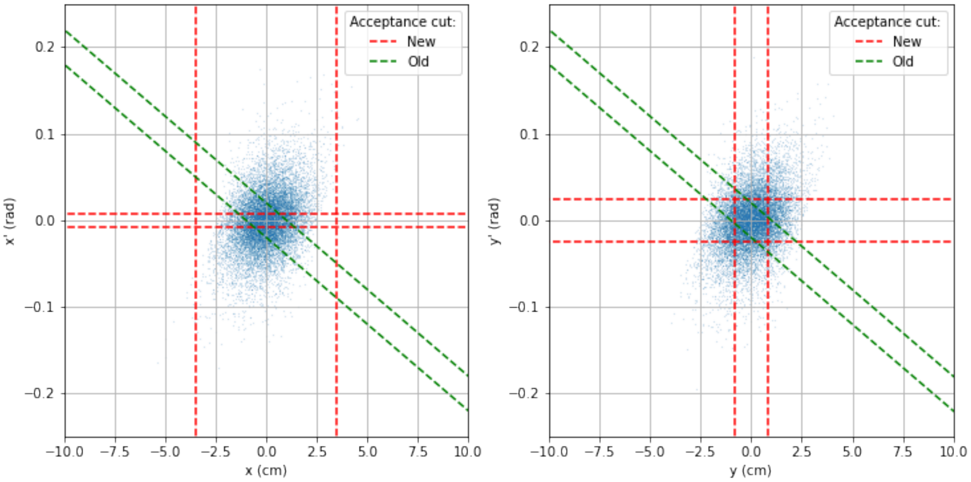

(a) Tungsten target

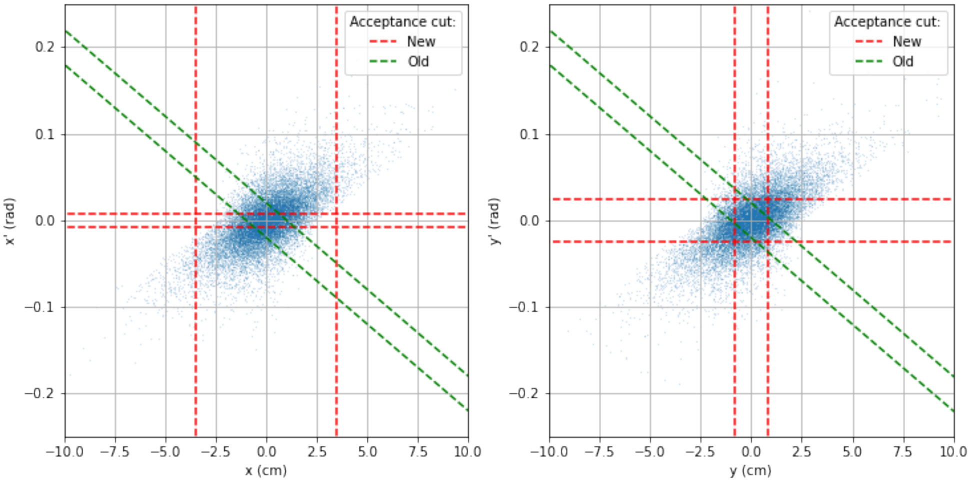

(b) Carbon target

Figure 3.9: Scatter plots of the production position against production angle of particles in the (*left*) horizontal and (*right*) vertical planes for (a) tungsten and (b) carbon targets at 13 GeV/c. The dashed lines represent the original and new phase space acceptance cuts.

on the suitability of a target and the cuts that have been used. Specifically, the tungsten target's performance drops by 58% and 48% at 13 and 2 GeV/c respectively, while the carbon target produces 41% and 28% fewer good particles at the same energies.

The reason for this is that the old and new acceptance cuts prioritise different aspects of the particle distributions in phase space. Specifically, focusing on the extremely asymmetric horizontal acceptance, the large spatial acceptance of the new cuts benefit much more the carbon target compared with the tungsten target due to the former's much larger positional spread which can be wholly accommodated by the new horizontal acceptance. Additionally, the small angular acceptance also has a more negative impact on the yields of the tungsten target, due to its larger angular spread. These two effects combined lead to the expected rate of a tungsten target at 13 GeV/c to drop much more significantly when compared to a carbon target.

What this shows overall is that, while the acceptance cuts may be useful in providing trends in the performance of the same target, the comparison of different targets may not be accurate if it is not done for the specific beamline being used.

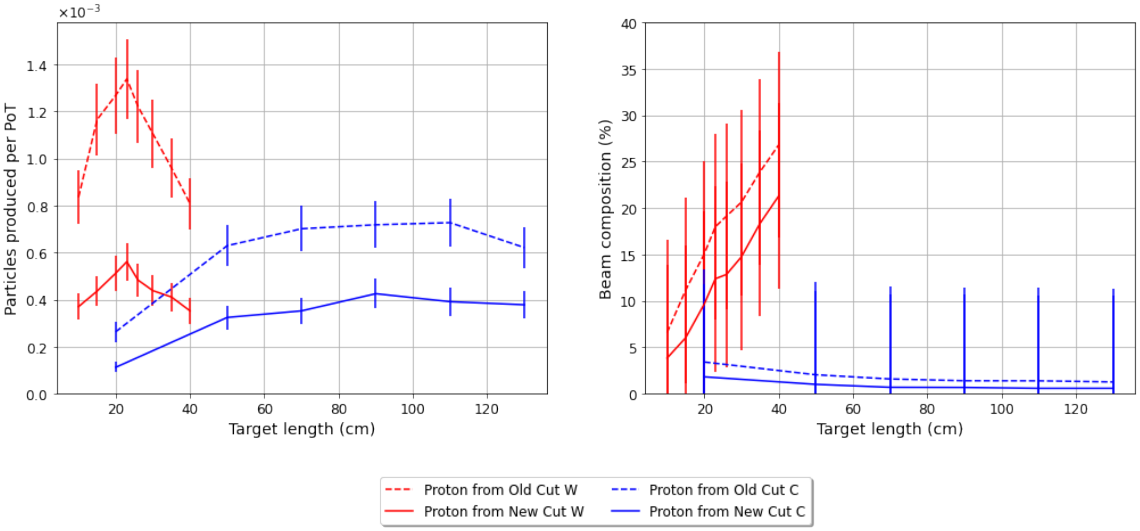

(a) 2 GeV/c

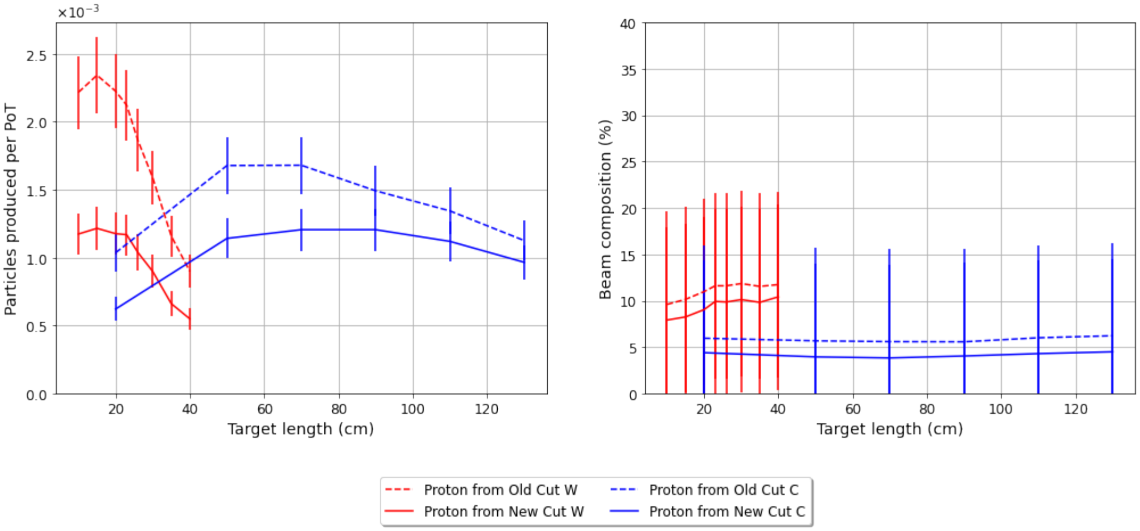

(b) 13 GeV/c

Figure 3.10: Effect of selection cuts on (a) the particle yields as a function of target length and (b) the beam composition as a function of target length.

3.4 Target Implementation

To be able to satisfy both a maximal rate requirement and an optimal composition requirement, it was decided to implement a target switching station, shown in *Figure* 3.11, to enable the use of several different targets in the beamline. Thanks to this, it will be possible to have up to three targets which the users of the beamline will be able to remotely switch between. This was done to provide future flexibility in terms of types of beam which will be transported in the low-energy beamline.

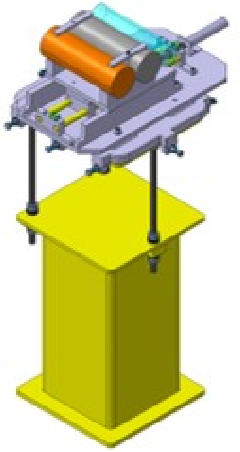

Figure 3.11: Schematic of the target switching station.

This may be useful if, for example, NA61/SHINE would require a change of target between a high-purity beam and a high-intensity run, rather than requiring access in a controlled radiation area, this switch could be done remotely, saving a significant amount of beam time. Additionally, while the initial three targets have been selected based on a combination of particle intensity and beam purity, as discussed previously, it is possible that in the future NA61/SHINE may want to optimise each target for a different type of particle beam, or for use at a different energy. With this target switching station, it will be possible to do this easily.

Chapter 4

Optics Design and Optimisation

This chapter describes the application of the beam dynamics theory described in Chapter 2. Specifically, how this has been used to develop a novel optimisation procedure based on a grid scan technique. This will be discussed in depth alongside the derivation of several important performance metrics. Finally, the application of this methodology to the development of a new low-energy beamline which will serve NA61/SHINE is described and compared to the results which would have been obtained using the more conventional matching technique.

4.1 Beamline Requirements and Constraints

There have been two sets of requirements and limitations imposed on the design of the low-energy beamline: the physics requirements on the beam parameters imposed by NA61/SHINE, and the infrastructure and engineering constraints needed for the beamline to be built in the North Area.

The first set of demands arising from NA61/SHINE is dictated by the desired measurements for which the beamline will be used, described in Section 1.2.3. These describe the minimum acceptable values for the key figures of merit of the beamline. To satisfy the physics programmes under consideration, the beamline must be capable of delivering protons, pions, and kaons within a momentum range from 2 GeV/c to 13 GeV/c. It must also be capable of delivering beams with momentum resolution better than 5%. Additionally, the rate of relevant particles delivered to the experiment must be at least 50 Hz or approximately 250 particles per spill to maintain a reasonably short data-taking period, while also ensuring that the total rate does not exceed 1.5×10^4 Hz, such that the NA61/SHINE detector is capable of maintaining a pile-up rate at a similar level as in the past. Finally, to ensure all secondary particles impinge onto the NA61/SHINE target, the size of the beam at the end of the beamline must be smaller than 20 mm RMS in both planes [17]. These requirements are summarised in Table 4.1.

The second set of constraints arises from the many infrastructure limitations, key amongst them being the limited time-frame for this beamline to be installed. In order to produce useful results for the experiments requesting data from NA61/SHINE, the beamline must be in place and collecting data before 2026. This limited the design of the beamline to the use of pre-existing dipole and quadrupole magnets, and standard connectors already available in the North Area, to maintain a rapid implementation and low costs. There are also other limitations imposed on the design of the beamline, such as Radiation Protection (RP) limits, and these will be discussed in depth in Chapter 7.

Parameters	Requirements
Desired particles	p, $\pi^{\pm}$, $K^{\pm}$
Momentum	2-13 GeV/c
$\Delta p/p$	$< 5\%$
Minimum rate	50 Hz
Maximum rate	$< 1.5 \times 10^4$ Hz
Beam-size RMS (at NA61/SHINE target)	20 mm

Table 4.1: The figures of merit necessary for the low-energy beamline measurements, from Ref. [17].

4.2 A Novel Algorithmic Approach to Beamline Design

In this section the current techniques for beamline design and optimisation are discussed alongside their shortcomings. Following this, a new methodology for designing beamlines is introduced, with a description of how it works, how various figures of merit are calculated and finally how this can be used to fully design a new beamline.

4.2.1 Current Design Techniques

To design a beamline, the usual approach followed at CERN and elsewhere is to start from the physical constraints present, such as the maximum quadrupole strengths kl_{ϵ} available, the maximal beamline length L_{tot} desired or the minimal inter-elemental distances d_{ϵ} and using these to best try to meet the experimental requirements, such as the necessary acceptance, momentum resolution, and the desired beam-spot size at specific locations. To meet these requirements, the specifications are essentially translated to a set of constraints to which the beamline is matched, using specialised software such as TRANSPORT [42] or MAD-X [43], while also considering the necessary layout of the line in terms of direction, bending angles, and shielding requirements. This matching is done using the point-to-point and the parallel-to-point beam transport conditions which have been introduced in Section 2.4.

While this works in producing solutions to a given problem, this process has several drawbacks. The first of these issues is that the matching routines used are, in general, minimisation algorithms (like the CERN-developed MINUIT [68]), hence the results to which they converge can be dependent on the initial values chosen. Further, given the complex interplay between parameters, the solution found can be a local minimum rather than the global minimum, meaning that the optimal solution may remain out of reach. Moreover, the approach of ray tracing and matching is restricted to first-order optics only, with second-order corrections often necessitating special treatment. Finally, when matching certain assumptions are usually made, especially on the source term, which affect the values to which a designer matches a beamline. While these are often reasonable assumptions, if they were to break down, they may lead to significant inaccuracies when designing a beamline. For example, assuming a point-like starting distribution is not fully accurate when considering momenta of approximately 2 GeV/c, as discussed in Section 3.1. Additionally, when optimising beamlines via matching, it is impossible to maximise the acceptance. This is because the acceptance is a function of the R-matrices throughout *the whole beamline*, whereas matching only fixes the R-matrix at one point, with no regard for the rest of the beamline.

E. Regenstreif undertook pioneering work addressing the acceptance maximisation problem [69–71], deriving analytical expressions as well as acceptance contours by taking into account several possible conditions for particles to graze the apertures of beamline elements. The formulas he derived are rather cumbersome for practical use and do not take into consideration any higher-order aberrations (chromatic or geometric) that can be important when $\Delta p/p$ exceeds ±5% and the deflection angles are larger than a few mrad. These make the direct application of these formulas a rather difficult task. The problem becomes even more complicated when the drifts in the beamline are not equal between the quadrupoles (non-symmetric n-tuples), further reducing the effectiveness of this approach. Finally, on top of these physics-driven difficulties, resource-driven constraints often need to be considered, e.g budgetary constraints or element availability, which may reduce the number of possible solutions. These cannot easily be implemented when considering a beamline from a purely mathematical point of view, and so it becomes clear that the matching approach, while useful for obtaining an insight into the challenges of optimisation, is limited in its direct impact in a beamline design environment. Due to these issues, oftentimes, the acceptance optimisation is left as a trial-and-error, experience-driven, endeavour.

4.2.2 Novel Methodology for Beamline Design

This new methodology tackles the issue of beamline optimisation from a fundamentally different direction than the standard matching approach. Here, instead of matching free parameters to obtain certain beam properties at specific positions, the design parameter space of the entire beamline is fully explored via an n-dimensional grid scan, with key figures of merit being calculated analytically for millions of different configurations. These configurations are then catalogued and presented to the accelerator physicist such that the one which best matches the requirements of the experiment can be identified and used. The design process is separated into two steps.

First, we consider the beamline as a series of *elements* which have parameters that are either free and lie within a certain range or are fixed. We then split each of the free variable's ranges into a number of user-defined steps and use these to investigate many possible beamline configurations. For each of these configurations several figures of merit are calculated and returned as a Python dataframe object[1] [72]. In this context, when discussing an *element*, we are talking about any optical element in a beamline which can be described via the R-matrix formalism, for example, drifts, dipoles, quadrupoles, or even collimators.

Following the creation of this dataframe, the second step leverages the generality used up to this point to be able to meet the design requirements placed on the beamline. To do this, configurations in the dataframe are removed according to the experimental requirements until only the most optimal solutions are present. These selection cuts are based upon the figures of merit calculated in step one, so, for example, if a beamline needs to transport a large number of particles, a selection cut applied may be one which only keeps the beamlines with the largest 10% acceptance, whereas, if a design needs good momentum resolution, a cut may be required to minimise the size of the beam at the position of the collimator. If a beamline needs both a high-acceptance and a good momentum resolution, it is straightforward to simply apply these two cuts sequentially. Each beamline configuration that passes this selection process is one which would come as close to satisfying the experimental requirements as possible, given the initial constraints on the beamline.

To complete the optimisation by taking into account both second-order effects and initial particle distributions, these configurations are then exported to a program like MAD-X PTC to run a full particle tracking simulation. With this information, it is then possible to select the beamline that best satisfies the design requirements while working within the real-world constraints placed on the beamline.

The main advantage of this optimisation scheme is that it not only provides an optimal beamline design given a set of metrics and objectives, but it establishes an accurate surrogate model for the beamline. This enables the modelling of various output features efficiently, and then, once these have been catalogued, these can be retrieved efficiently. Thanks to this, it is possible to rapidly modify the beamline design as design priorities

---

[1] A Python dataframe object is a two dimensional array, or a table, with rows, columns, and often headers.

were changed during the early development of the beamline.

4.2.3 Figures of Merit Calculated

The key advantage of the parameter scan algorithm over matching techniques is that using this approach, the figures of merit for many beamline combinations are known and these can guide the beamline selection. To provide sufficient information to the beamline designer, several different figures of merit are calculated. These are:

- The accepted phase space in the horizontal and vertical planes,
- The maximum angle and position of particles that can be accepted in both planes,
- The position of the focal point in a user-defined range,
- The beam size at several user-defined positions,
- The beam's spot-size at the end of the beamline,
- The total length of the beamline,
- The R-matrix at several user-defined positions,
- The R-matrix at the end of the line.

In this section, the definition of each of these figures is discussed, along with an explanation of how they are obtained. Each of these figures is calculated for millions of configurations, so a focus on efficiency was important. As such, whenever possible, functions from either the Pandas or Numpy Python libraries are used, as many of the functions included in these are integrated as C, C++, and Fortran codes in Python itself, thereby speeding up calculations.

Calculation of the Accepted Phase Space and Other Figures of Merit

The accepted phase space of a beamline is the area of phase space which can be successfully transported from the start of the beamline to its end. Particles on the perimeter of this shape graze at least one of the elements of the beamline, whereas those that are within the

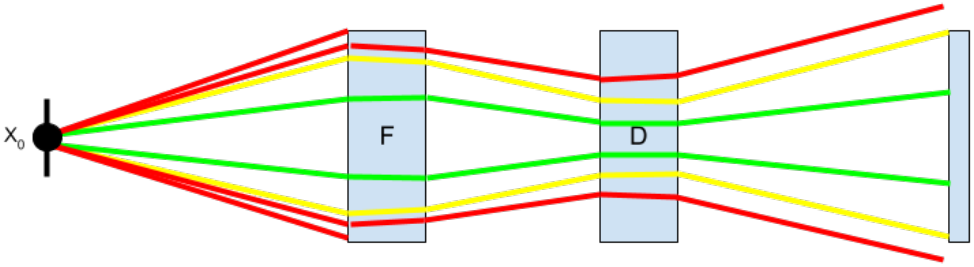

Figure 4.1: A sketch of a doublet system. The green rays are well within the accepted phase space as they do not touch any apertures. The yellow lines would be the maximum angle a particle starting from x_0 could have before being outside the beamline's acceptance. Rays in red will not reach the target. These values change as x_0 is varied over the whole object, and by storing the maximum angle for each starting position the accepted phase space can be calculated.

area are transported throughout the beamline without grazing any apertures. Similarly to Regenstreif [70], to calculate the accepted phase space of each configuration, we find the largest angle a particle with a given initial position x_0 can have before touching any element. This is done by rearranging

$$\pm a_\epsilon = R^\epsilon_{11}x + R^\epsilon_{22}x' \tag{4.1}$$

at each element ϵ with aperture a_ϵ and considering the angle with the smallest magnitude as the edge of the phase space. This is then repeated for a range of initial positions x_0, finding the whole accepted phase space. This process is shown schematically in *Figure* 4.1 and is done simultaneously for the horizontal and vertical planes.

Once the whole phase space has been calculated it becomes trivial to find the maximum angle and position of particles which can be accepted in both planes.

Some care has to be taken when considering focusing quadrupoles, as a particle may graze the aperture of the magnet part way through the quadrupole. A full expression for the phase-space contour caused by this consideration can be calculated [69–71], however this proved to be too cumbersome for the parameter scan algorithm; as such, to approximate this effect, quadrupoles were simply broken up into several user-defined steps.

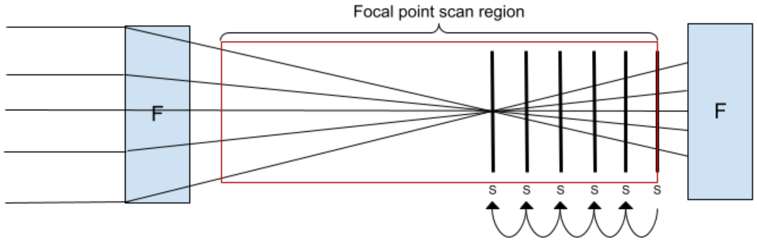

Figure 4.2: How the position of a focal point is calculated. To save computing power, when the beam size begins to grow again the position is saved and the scan in that plane ends.

Calculation of the Beam-Spot Size at a Given Location

Once the accepted phase space has been calculated, it is possible to calculate the size of the beam at any point along the beamline. By applying the R-matrix of the beamline up to the desired point as a transformation to the initial phase space, one obtains the phase space of particles at this new position. This then can be easily used to provide the size of the beam at any given point along the beam line.

It is often useful to have a beam focal point inside an aperture restriction, like a collimator, and the parameter scan also calculates and returns if any focal points are present near a collimator. It does this by calculating the size of the beam in a similar fashion as described above, but does this iteratively over the length of the collimator and adjacent drifts. As this calculation is underway, the program stores the z coordinate where the beam size is smallest, saving it as the position of the focal point. The step size of this scan can be chosen by the user. This procedure is illustrated in *Figure* 4.2.

As the beam could be focused in the x-plane, the y-plane, or both simultaneously, the user can decide if they would prefer a single focus or a double focus. In the latter case, the parameter scan will save both z coordinates where the beam was smallest in the x-plane and in the y-plane.

Length of the Beamline

The total length of a configuration on the other hand is simply obtained by summing the lengths of all elements and drifts in the beamline. It is useful to have this output as drift lengths can be varied as free parameters, as such the total length of the beamline is subject to change throughout the optimisation process.

R-Matrices Along the Beamline

Finally, as the R-matrices need to be calculated at each element to obtain the acceptance of the configuration, it is straightforward to return these too, if requested by the user. This feature has been included to enable useful comparisons to results which have been obtained using the standard matching techniques.

4.2.4 Performing a Parameter Scan

The initialisation of a parameter scan is a straightforward task. Using the Python code developed during this DPhil, one must only decide on the number and order of elements that will be used, decide which parameters will be free and which will be fixed, and either the value for these fixed parameters, or the range of the variable ones. It is possible to also test configurations with different combinations of magnet types and polarities.

As the number of configurations, N_{config}, to scan through grows exponentially with the number of steps, s, and free parameters used, f, according to the equation

$$N_{config} = s^f, \tag{4.2}$$

it is important to perform initial scans with a small number of steps to enable quick identification of unsatisfactory configurations. For example, by setting a rather low number of steps, between 5 and 10, it is possible to quickly assess the effect of different types of magnets on the figures of merit of a beamline, and decide on which of these are best suited for the problem at hand. This significantly speeds up the beamline design process.

Once the main layout of the beamline, namely the magnet types and polarities, has been decided, it is possible to run a finer scan, to find the optimal beamline configurations. For this, the number of steps can be increased to anywhere between 20 to 40 per parameter, depending on the computing resources available. As the program has been designed to be easily run in several batches, it is also possible to scale the number of beamlines analysed by parallelising the optimisation.

To further decrease the number of total configurations to analyse, it is often useful to split the design of a whole beamline into several smaller *stations*. This process is described in detail in the next section, where the process for designing the low-energy beamline for NA61/SHINE is described, but in brief *stations* are groups of elements of the beamline which work together to achieve a specific function, for example a momentum selection station consists of several dipoles which are used together to perform the momentum selection on the beam. If the beamline can be split into several *stations* these can be optimised individually, meaning that from having to explore all different free parameters in a beamline, one only has to focus on those of each *station*. This is necessary as, without this step, the total number of configurations would be far beyond what can currently be achieved with our computing power while using Python. An example of this process being implemented is in the separate optimisation of the front end of a beamline and the back end independently, as the back end can be shown to not have a large effect on the beamline's acceptance, and there are sufficient degrees of freedom in a triplet back end to focus a beam regardless of the initial phase-space distribution.

After each of these steps, it is possible to either compare the outputs of the program in a dataframe, being able to study the performance of beamlines rapidly, or one can feed these into MAD-X PTC. The latter provides more precise information on the performance of each configuration, but at the cost of a significantly longer analysis time.

The process of initialising and performing a parameter scan to obtain a working beamline can be seen in *Figure* 4.3.

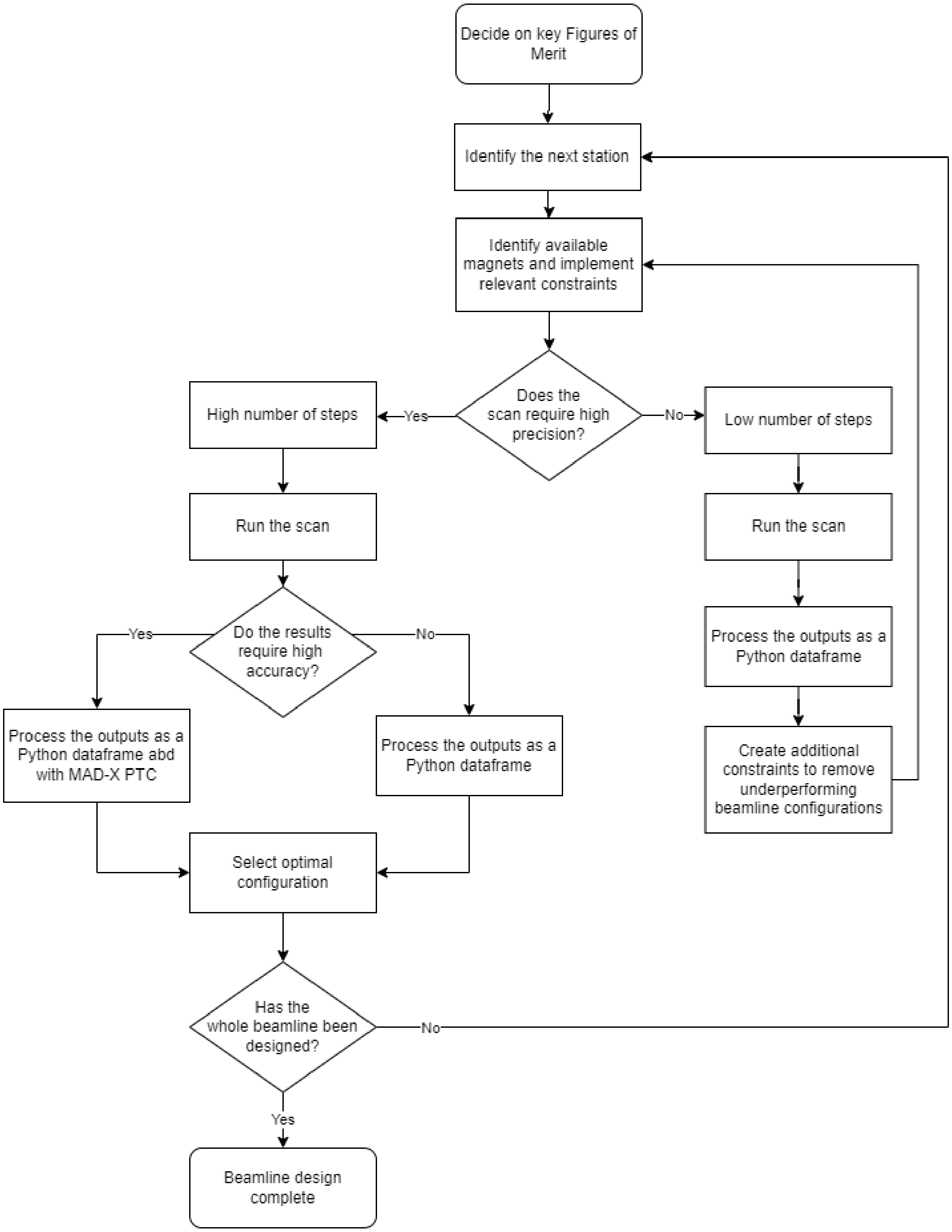

Figure 4.3: Flowchart of the beamline design process.

4.3 Designing NA61/SHINE's Low-Energy Beamline

As described in the previous section, the design of a beamline is underpinned by the constraints faced by the accelerator physicist. To this end, it is important to introduce the magnets available for use at CERN and other spatial constraints necessary for the installation of magnets. Following this brief discussion, the process via which the low-energy beamline for NA61/SHINE was designed is explained in detail.

4.3.1 North Area Magnets

As the North Area enables data-taking for many different experiments requiring extremely different beams, there is a great amount of flexibility in the magnets which are available to transport beams. A list of these magnets, both dipoles and quadrupoles, can be found in Ref [73]. These can be used in very low-energy, low-intensity beams to high-energy, high-intensity beams, and anything in between.

Out of all of these magnets, it was important to focus on the most relevant ones for the design of a high-acceptance low-energy beamline. Such a beamline requires both sufficiently high gradients, to maintain a short focal length, and large apertures, to maximise acceptance and particle rates. At the same time, however, to minimise the cost and reduce the preparation time, necessary to adhere to the requirements of NA61/SHINE [17], only readily available magnets were considered in this thesis. Because of these constraints, the most relevant magnets used in the North Area are the QPL, QNL, and QWL quadrupoles and the MBPL family of dipoles, with their various apertures.

The quadrupoles, shown in *Figure* 4.4, mainly differ in aperture and maximum achievable magnetic field gradient. The main properties of these magnetic elements can be found in *Table* 4.2. In addition to these 3 different quadrupoles, it was also possible to use QPL's short variant, denoted QPS. This magnet is identical to its long counterparts except that it is half as long.

The family of MBPL dipole magnets, one of which is shown in *Figure* 4.5, only differ in their apertures and in the peak magnetic fields these can achieve. The details can be found in *Table* 4.2, with the general trend being that as the aperture is increased, the

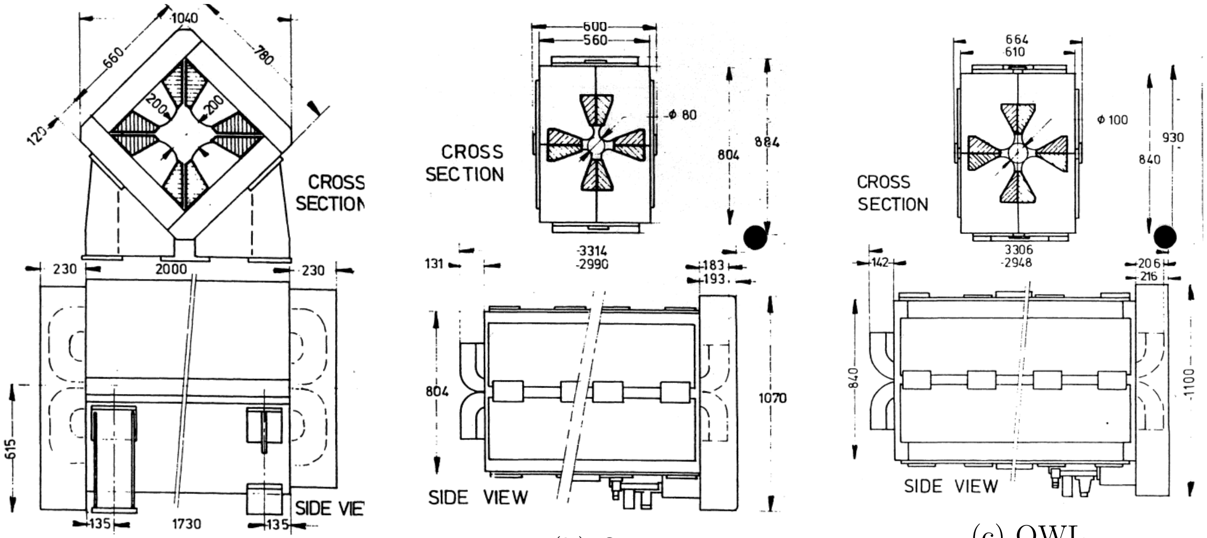

(a) QPL (b) QNL (c) QWL

Figure 4.4: Technical drawings of three common quadrupoles used in the North Area. (*top*) the x-y cross section, (*bottom*) the side view of the magnet [73].

maximum field decreases, leading to a trade off between maximum momentum resolution achievable and particle rates.

4.3.2 Beamline Design Process

As explained in Section 4.2, while the parameter scan approach provides immense flexibility, the number of configurations to analyse increases exponentially with the number of steps and free parameters. While up to 7 free parameters can be analysed in a reasonable amount of time and with sufficiently small steps, more free parameters begin to become difficult and overly time consuming. In this project, the minimum number of total free parameters was 9, as is shown in *Figure* 4.6, so it was important to break up the optimisation process into smaller, more manageable steps. This figure is reached as following: the front end must be capable of focusing the particle beam in the 4-bend achromat while not losing too many particles. This requires a minimum of two quadrupole magnets. On the other hand, to simultaneously focus the beam in both planes, while maintaining the possibility of moving the beam's focal point, three quadrupoles are required for the back end. Considering these magnets and the drifts between them, we arrive at the beamline shown in *Figure* 4.6.

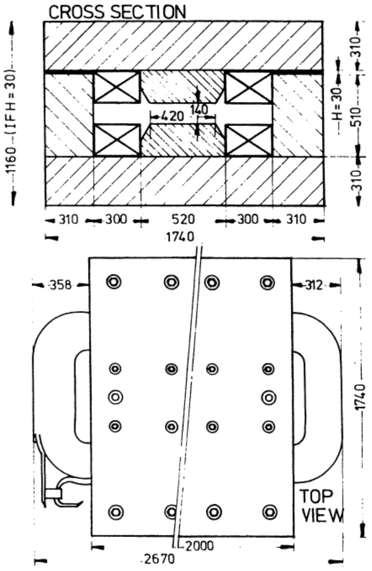

Figure 4.5: Technical drawings of an MBPL dipole used in the North Area. (*top*) the x-y cross section, (*bottom*) the side view of the magnet [73].

The beamline was separated into a front end, consisting of the initial acceptance section and the momentum selection station, composed of a 4-bend achromat, which would be optimised first. This was followed by the optimisation of the back end, the final focusing section, and would include the entire front end as a beamline as a fixed section with no free parameters.

This two-stage optimisation design was chosen as the strengths of the quadrupoles in the front end dictate the position of the focal point of the beamline, meaning that the front end and the momentum selection station could not be separated. On the other hand, after the momentum selection, the behaviour of the final focusing back end is relatively independent of the type of beam which it receives, as there are enough degrees of freedom to provide a focused beam, so it makes sense to optimise this separately. The only additional challenge was to not decrease the acceptance of the beamline with the back end but due to the large apertures used, this was achieved during the parameter scan.

The original nine free parameters already do not include some values which have been chosen due to specific requirements in this project. For example, the drifts between

Magnet type	Nominal peak gradient or magnetic field ($^{\mathrm{T}}/_{\mathrm{m}}$ or T)	Inscribed diameter (mm)	Aperture height (mm)	Useful aperture width (mm)	Core overall length (m)
QPL	10.5	200	-	-	2.000
QPS	10.5	200	-	-	1.000
QNL	24.0	80	-	-	2.990
QWL	19.5	100	-	-	2.948
MBPL-110	1.94	-	110	300	2.000
MBPL-140	1.75	-	140	300	2.000
MBPL-200	1.48	-	200	300	2.000

Table 4.2: The parameters for several magnets of interest [73, 74].

Quad_2-Bend_1, and Bend_4-Quad_3, have been chosen to be the shortest possible distance, as otherwise the acceptance of the line will significantly decrease, as will be discussed in the coming sections. The magnetic strengths of the dipoles are also always maximised, to achieve the best momentum resolution possible and finally, the last drift, up to the NA61/SHINE target is fixed by the requirement of a focal point in the optics, the location of which is determined by the previous quadrupole strengths.

4.3.3 Designing the Front End

Constraints

As the beamline is to be implemented in the North Area as a modification to the H2 beamline, both the optics upstream of the new beamline and the location of the NA61/SHINE experiment cannot be modified. While there was flexibility on the overall length of the beamline, as the optics of H2 could be modified significantly, the direction at which particles arrive cannot be changed. This has important consequences for momentum selection. As discussed in Section 2.6, there are three main setups via which one can introduce and subsequently remove dispersion. These are the two-bend, three-bend, and four-bend achromats. As is discussed in Chapter 2, of these three, the four-bend achromat is the

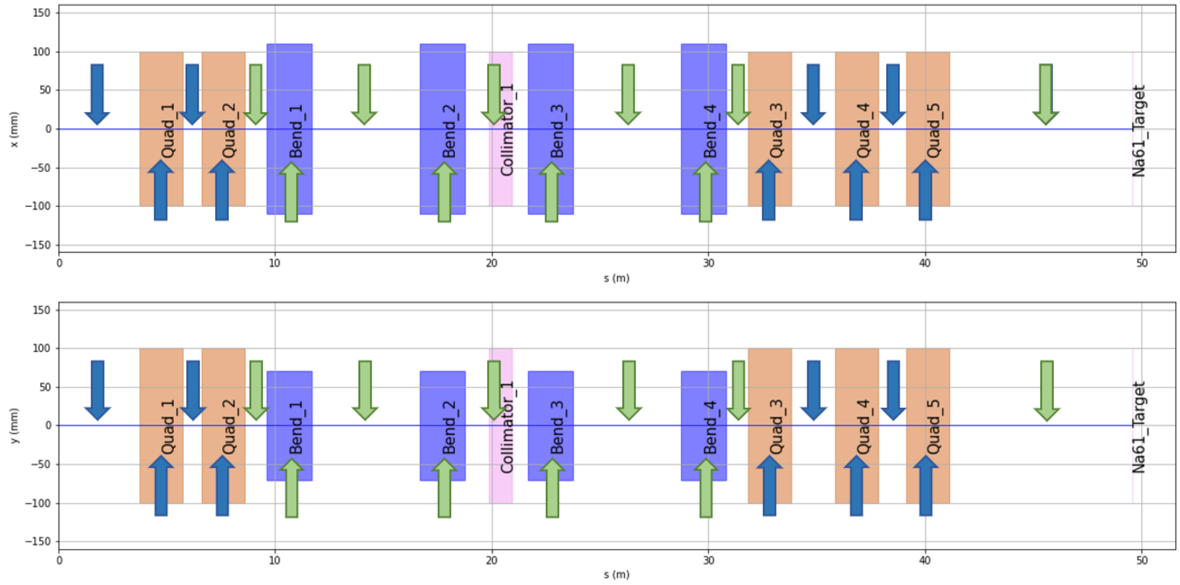

Figure 4.6: A sketch of the (*top*) horizontal and (*bottom*) vertical planes of a beamline, with the minimum number of necessary magnets to meet the NA61/SHINE requirements. Two magnets in the front end for focusing the beam at the collimator and a triplet at the back end to focus in both planes. The free parameters are shown in *blue* are either drifts or magnetic gradients, while the fixed parameters in *green* are either drifts or dipole strengths.

only one in which the outgoing beam is travelling in the same direction as in the original beamline, as such, it is the only one which can be used to deliver the beam to NA61/SHINE.

In addition to this constraint, there are minimum distances between magnets which must be respected. These are necessary to have some space between the magnets' coils and to place connectors for the vacuum tubes between magnets. The latter are important they can become quite large when attaching two beam-pipes of different sizes, as is the case when going from a quadrupole magnet to an MBPL magnet, and so must be carefully accounted for when deciding the range of possible drift lengths.

Scans performed

Once the constraints are set in place, namely the types of magnets with their associated maximum fields, and the drift lengths, it was possible to perform coarse parameter scans. With these, the aim was to assess the performance of different setups and to highlight whether a type of magnet would meet the specifications set out by the experiment and which combination of these would provide optimal results. These initial scans involved simulating the beamline up to the end of the four-bend achromat, to gain information on the overall beamline structure that would perform best. The requirements for configurations to be considered in this initial selection were simply that the beamline be well focused (with a beam-spot size smaller than 3 cm) within the collimator.

In the case of a high-acceptance low-energy beamline, the results showed the QPL magnets were the optimal choice. This clearly implies that when designing a high-acceptance beamline the main emphasis ought to be placed on the aperture of the magnets rather than the gradient strength. The QPL magnets, with an aperture which is more than twice as large as some of the other options were capable of transporting a much larger phase space through the beamline, and so will be able to transport a much greater number of secondary particles. This can be seen in *Figure* 4.7, where a scatter plot of the accepted phase spaces in both planes for three Focusing-Defocusing-Focusing (FDF) triplets comprised of either two QPL magnets, two QNL magnets or two QWL magnets is shown.

Following the magnet selection, it was necessary to decide whether the beamline's front end would be comprised of a doublet, a triplet, or something else, and the polarities of the magnets. When running this coarse scan, it was important to already include any collimators, bending magnets or any other devices which may introduce asymmetry between the horizontal and vertical planes, as otherwise any results for DF beamlines would have been identical to those of an FD configuration (and similarly for the triplet configurations).

The configuration chosen for the low-energy beamline was a Defocusing-Focusing (DF) configuration (using the horizontal plane polarities as reference and assuming positive particles). While this did not have the highest accepted phase-space area when requiring a focus in the bending plane, as can be seen in *Figure* 4.8, and is expected due to the FDF having more degrees of freedom, the difference in performance between a DF and an FDF configuration was minimal, on the order of a few tens of mrad mm in the horizontal

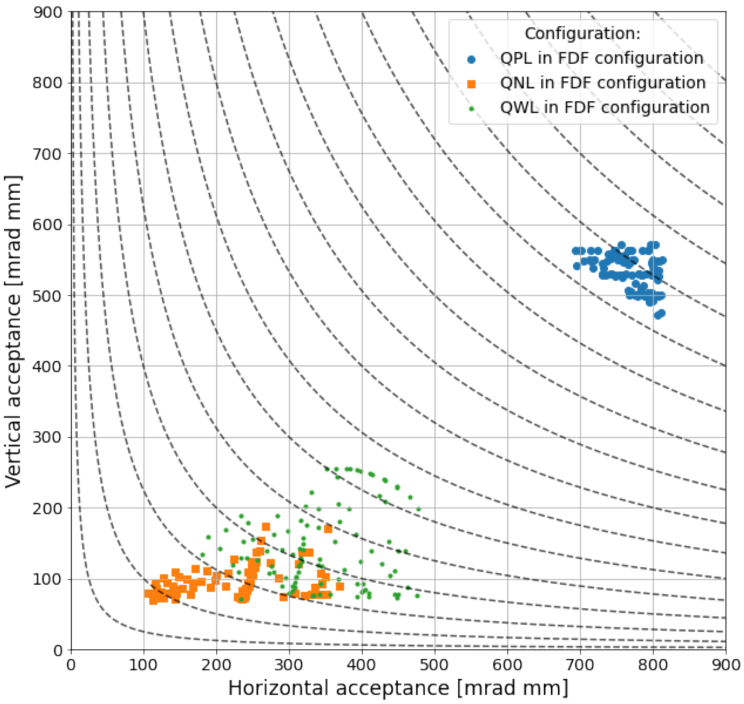

Figure 4.7: A scatter plot of the horizontal and vertical phase-space acceptances for the 100 best-performing beamlines using different magnet types. The dashed lines show contours with an equal product of horizontal and vertical acceptances.

plane only. This small gain in acceptance would also have to be considered against the monetary gains from using one less magnet. Additionally, *Figure* 4.8 disproportionately shows configurations with 3 quadrupoles as performing well since for these, 6 parameters have been scanned versus the 4 of the doublet configurations, meaning that many more configurations that perform well could be found for the triplets. The main downside of the doublet is the asymmetric acceptance in the horizontal and vertical planes, which may be an issue in certain specific applications, however, these are not a concern for the applications of this low-energy beamline [75].

After this, a finer parameter scan was run, using the optimal magnets and configuration. This achieved a higher resolution compared to the coarse scans, ensuring that the relevant configurations are not lost to a large step size in the scans. A number of the

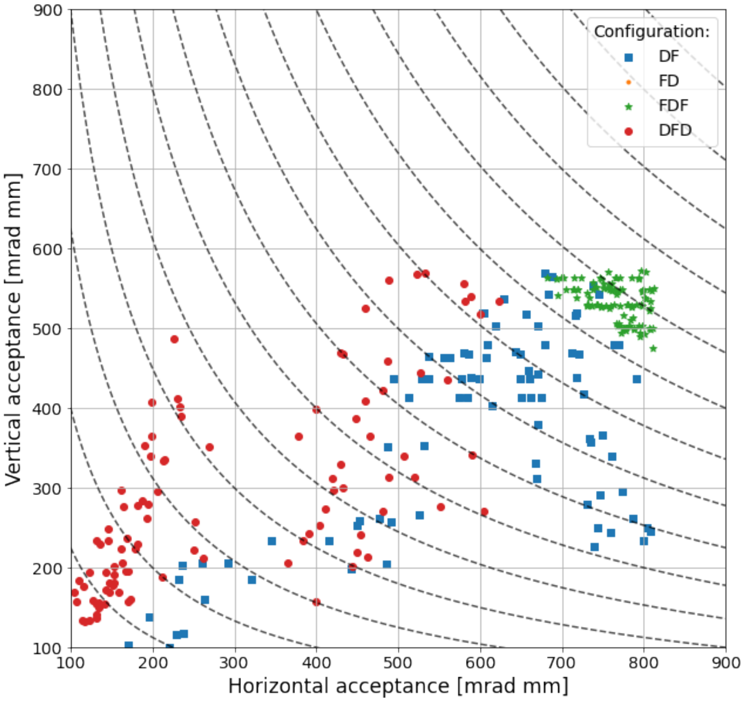

Figure 4.8: A scatter plot of the horizontal and vertical phase-space acceptances for the 100 best-performing beamlines using different configurations. The FD configuration is not present in the image as the required focus ($<$ 30 mm beam-spot size in the horizontal plane) comes at a large cost in terms of phase-space acceptance. The dashed lines show contours with an equal product of horizontal and vertical acceptances.

beamlines whose figures of merit best matched the desired values were then assessed using MAD-X Polymorphic Tracking Code (MAD-X PTC), ensuring that the optimal beamline is selected even when accounting for higher order effects. As particle rate was such a key parameter for NA61/SHINE, the beamlines selected were those with the highest acceptance which also had a beam-spot size of less than 20 mm between the second and third bending magnets, where the collimator could be placed.

To maximise the acceptance, we considered the product of the area of accepted phase space in the x-plane and in the y-plane, which is expected to be proportional to the probability of a particle being transported to the end of the beamline. The underlying assumption to this technique is that the accepted phase space is wholly populated by particles produced at the target, which unfortunately may not be the case. To solve this issue, the configurations which were selected as being suitable for high-precision PTC tracking were those which were either in the subset of beamlines which have the largest product of phase spaces, the 50 with largest phase spaces in either plane, or those with the 50 largest angular acceptances. With these broad conditions, it was unlikely that the configuration with the highest particle rate would be missed in the pre-PTC selection.

For these PTC studies, particle tracks were initialised using the initial conditions obtained during the beamline's target studies. Specifically, each particle used for PTC corresponds to a particle produced by the secondary target, ensuring that the beamline would be optimised for the correct targets and using realistic particle distributions. Following PTC, the configuration for the front end which best suited the low-energy beamline was finally selected. This, alongside the optimised back end, can be found in Appendix B.

4.3.4 Designing the Back End

Constraints

The design of the back end was limited by the same constraints in terms of magnet type and magnet spacing as the front end of the beamline, limiting the scans to have the same values. To maintain the large accepted phase space, the same QPL magnets were used in the back end. Additionally, due to the long distance without a focusing magnet in the horizontal plane and the subsequent loss in phase-space acceptance this may lead to, it was necessary to use an FDF configuration for the back end to ensure sufficient flexibility for the future and to provide a much smaller beam spot than what would have been achieved using a simple doublet back end.

Beyond these constraints, NA61/SHINE also requested at least 7 m of instrumentation space after the last quadrupole magnet, to equip the area with instrumentation for track reconstruction and the trigger system, further constraining the parameters scan.

Scans performed

Once a front end was selected, a back end had to be added. For this, the front end was fixed to what was previously selected and a parameter scan was run on the back end to find the most suitable configuration. As the configuration and magnets were already in place, no coarse scans were necessary and only a fine parameter scan was run.

For the back-end optimisation we required the area of the accepted phase space of the whole beamline configuration, that is front end and back end, to not be smaller than 5% compared to the front end alone. This was done as the back end cannot increase the beamline's acceptance, hence ensuring that it does not decrease it is sufficient. Following this, the 100 configurations with the highest acceptances and smallest beam-spot sizes at the NA61/SHINE target, defined as $\sigma_{tot} = \sqrt{\sigma_x^2 + \sigma_y^2}$, where σ_i is the beam-spot size in the i direction.

In the specific case of the low-energy beamline for NA61/SHINE, as particle rate was of the utmost importance and the greatest difficulties were expected to be had in the low-energy regime at 2 GeV/c, the beamlines which was selected at the end was one which had the best low-energy particle transmission while still having better than 5% momentum resolution and a beam-size of less than 20 mm RMS in both planes, as requested by NA61/SHINE. The final values for the magnetic field strengths and the drift lengths can be found in Appendix B.

4.4 Performance of the Optics

Once the optics were designed, their performance was first investigated using MAD-X PTC. By using the initial distribution of particles obtained during the target studies, it was possible to understand the behaviour of particles in the low-energy beamline and study the chromatic effects in the beamline. These studies, in conjunction with those presented in Chapter 5, describe fully the behaviour of the low-energy beamline.

The beamline was first studied with MAD-X and then at a later stage with G4BL as MAD-X cannot take into account particle decays nor the effects of particles interacting with various elements. For example, protons interacting with the iron core of a quadrupole, hence, while the particle rates could be estimated using PTC exclusively, there would likely be significant differences with the real performance. Additionally, MADX does not take into account the magnets in the most precise way. In the code, the elements are idealised and do not fully reflect their real life counterparts, which may have an effect on the results obtained and on the particle rates expected. On the other hand, MAD-X is superior in presenting the behaviour of the particles as they travel within the beamline, hence results for the optics, rather than the beamline's figures of merit, are more enlightening when using MAD-X PTC. In this section, results for the optics, position of particle losses and the chromatic aberrations in the beamline are presented.

4.4.1 Nominal Momentum Behaviour

To study the overall behaviour of the optics, it is useful to begin by ignoring the effects of momentum spread and then, at a later stage, reintroduce them. This can be easily done by using the results of the simulations from the target optimisation studies and artificially re-scaling the momentum of each particle to be equal to the nominal momentum. These particles can be used in MAD-X PTC to study the evolution of each particle travelling in the beamline, and the output of this can then analysed using custom-made Python code. Following the understanding gained from this, it is trivial to then reintroduce the momentum spread.

The low-energy beamline's optics when no chromatic aberrations are present can be seen in *Figure* 4.9. Here, the elements of the beamline are all shown, with different colours corresponding to different types of elements, alongside the particles' tracks. In the figure, each blue line corresponds to the track of a single particle which has been produced in the target and which reaches the NA61/SHINE experiment. Importantly, the image shows that the beamline focuses particles in the horizontal plane, and so it will be possible to effectively perform momentum selection, as was requested during the parameter scans. Furthermore, we can also see several other important details very clearly, such as the small beam spot at the end of the beamline and the need for the smallest possible distance between the last bending magnet and the third quadrupole to limit the number of particles lost.

By ignoring the aberrations arising from the momentum spread in the beam, it is also

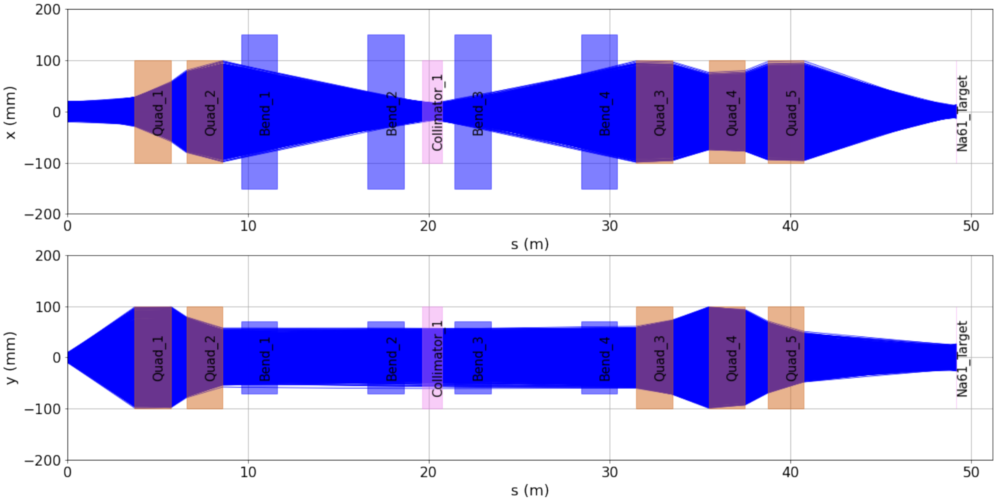

Figure 4.9: The tracks of monochromatic 13 GeV/c particles transported by the beamline. With this, it is possible to visualise the behaviour of the beam both in the horizontal plane (*top*) and in the vertical plane (*bottom*). The NA61/SHINE experiment target is at the end of this beamline. Only tracks which reach the NA61/SHINE target are shown in this figure.

possible to understand where the majority of the particles are lost as they are transported along the beamline. To this end, *Figure* 4.10 shows the percentage of beam surviving after each element, as a function of position along the beamline. This image shows the importance of maximising the acceptance of the front end, as the majority of particles lost are lost here, and justifies the separation of the parameter scan into the two stations which have been chosen.

4.4.2 Momentum Selection and Chromatic Aberrations

Having investigated the idealised behaviour of particles travelling through the beamline, the next step is to reintroduce the momentum spread of particles and assess its effects. To this end, *Figure* 4.11a, shows how particles with a momentum offset of +10%, 0%, and a −10% $\Delta p/p$ are transported along a beamline and how these errors on momentum affect the position of the focus in the beamline. As expected from the theoretical discussion on chromaticity presented in Chapter 2, the position of these focal points is shifted along the direction of the beam by an amount which is proportional to the momentum offset.

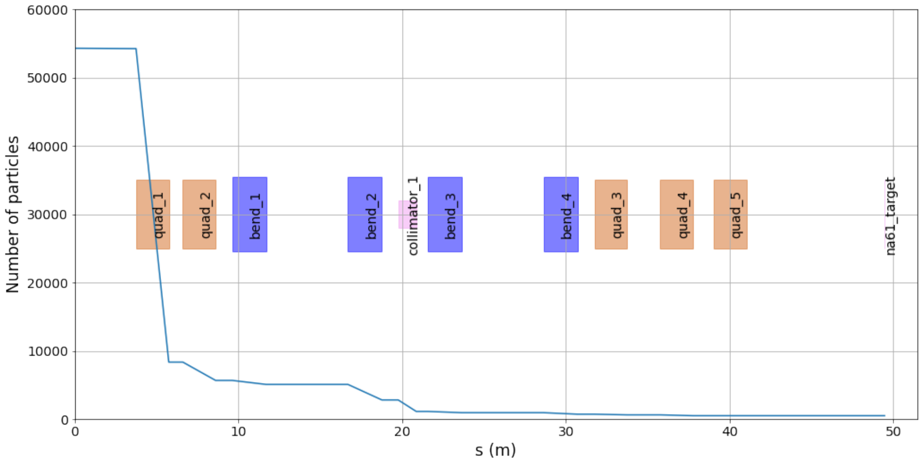

Figure 4.10: The total number of particles per 4.8 second long spill, as a function of position along the beamline. It can be seen that the majority of particles are lost in the acceptance defining front end.

The effects of chromaticity can be seen in both planes, with different-energy particles always focusing at different positions, however particularly significant is the fact that in the bending plane this effect causes a growth of the beam-size near the collimator, meaning that off-momentum particles may be able to pass through the collimator jaws even if theoretically this should not take place.

Furthermore, as shown in *Figure* 4.11b, the combination of chromaticity and a collimator may introduce some correlations between a particle's position and momentum offset, leading to an asymmetric beam spot at the end of the beamline.

This happens because, after dispersion is introduced and off-momentum particles are displaced horizontally, if a collimator is present this will remove particles asymmetrically. Specifically, if the image is positively displaced, the collimator's slit will firstly remove the most positively displaced particles and vice-versa for negatively displaced particles. This leads to only part of these images arriving at the end of the beamline, and hence the overall beam spot will be asymmetric. These effects can be reduced by more aggressive collimation as shown in *Figure* 4.11c, leading to reduced particle rates. The asymmetry introduced by these effects can be clearly seen in *Figure* 4.12. Here, the originally symmetric beam in *Figure* 4.12a, at first becomes asymmetric as highly off-momentum particles are removed, as can be seen in *Figure* 4.12b, however, when most of these particles are removed, the asymmetry decreases, as shown in *Figure* 4.12c.

With these effects in mind, it is possible to better understand the behaviour of the particles from the Monte-Carlo target studies travelling in the beamline. These are shown in *Figure* 4.13. The beamline behaves as expected, displaying the correct focusing and successfully delivering particles to the NA61/SHINE target. As expected from the previous discussion, there are correlations between a particle's position at the end of the beamline and its momentum offset.

It is important to investigate the extent to which it is possible to improve the momentum resolution of the beamline by closing the collimator jaws. This can be seen in *Figure* 4.14. The data points are given by the standard deviation of $\delta p/p$ of all particles reaching the end of the beamline at different collimator openings whereas the fit is given by

$$\mathrm{Std}\Big(\frac{\delta p}{p_{ref}}\Big) = \frac{1}{R_{16}} \cdot \sqrt{\frac{C^2}{12} + \mathrm{Std}(\nu)^2}, \tag{4.3}$$

fitted with R_{16} and $\mathrm{Std}(\nu)$ as free parameters. This equation was derived in Section 2.5. The values for these parameters for the optimal fit were 5.06 ± 0.02 and 7.15 ± 0.30 respectively and were somewhat in agreement with the real values of 5.64 ± 0.01 and 7.49 ± 0.13 from PTC data. These discrepancies likely arose due to the non-zero collimator length and the presence of second-order effects, seen above. However, it is clear that the beam is well-focused in the collimator and it will be possible to meet the experimental requirements of NA61/SHINE in terms of momentum resolution simply by closing the collimator jaws. Further studies of the momentum resolution the beamline will be capable of achieving have been performed using Monte-Carlo simulations and are presented in Chapter 5.

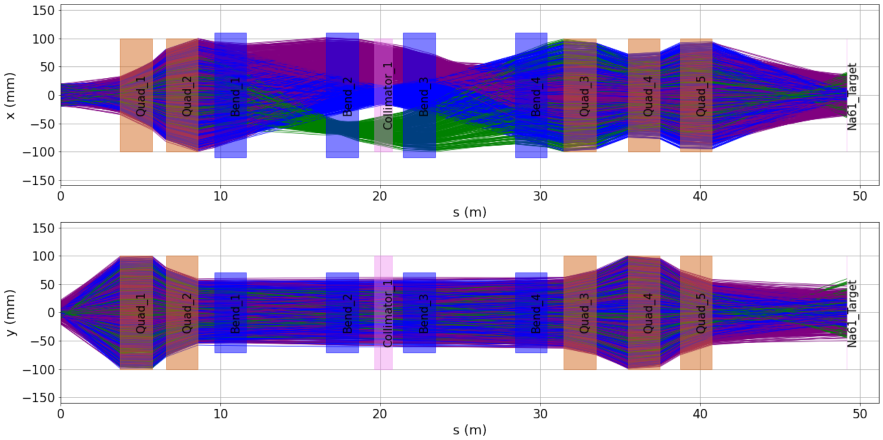

(a) Fully open jaws.

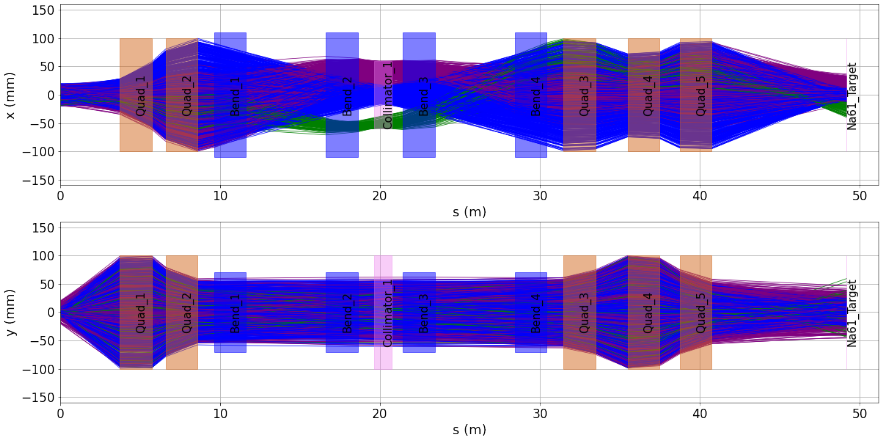

(b) Jaws closed to ±60 mm.

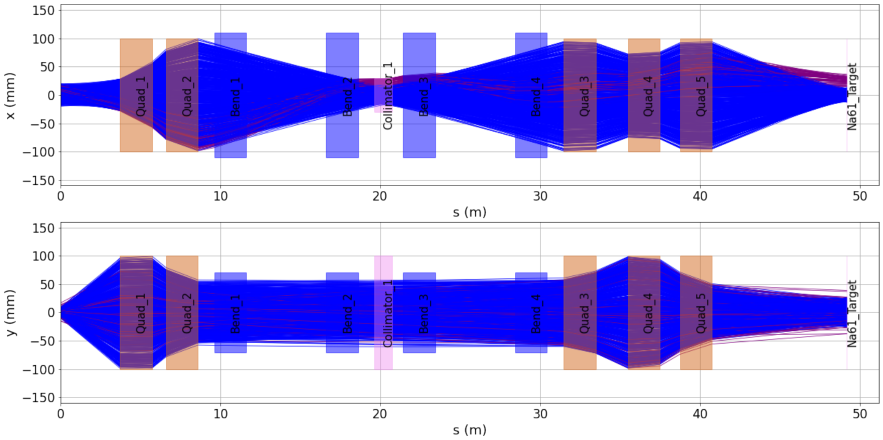

(c) Jaws closed to ±30 mm.

Figure 4.11: The tracks of particles with $\Delta p/p = -10\%$ (green), $\Delta p/p = 0\%$ (blue), and $\Delta p/p = +10\%$ (purple) which survive collimation in a four-bend achromat when the jaws are (a) fully open, (b) closed to ±60 mm, and (c) closed to ±30 mm.

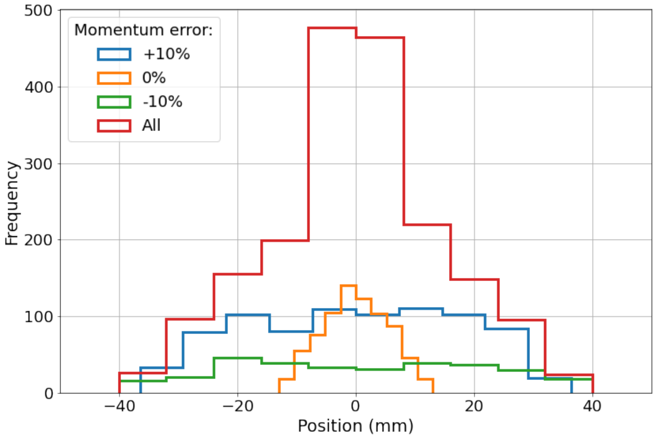

(a) Fully open jaws.

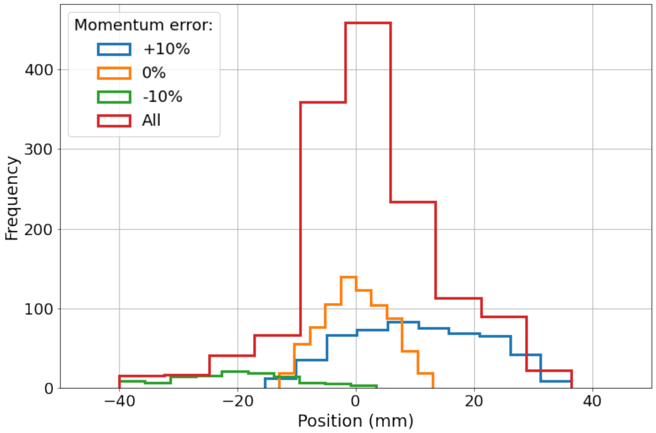

(b) Jaws closed to ±60 mm.

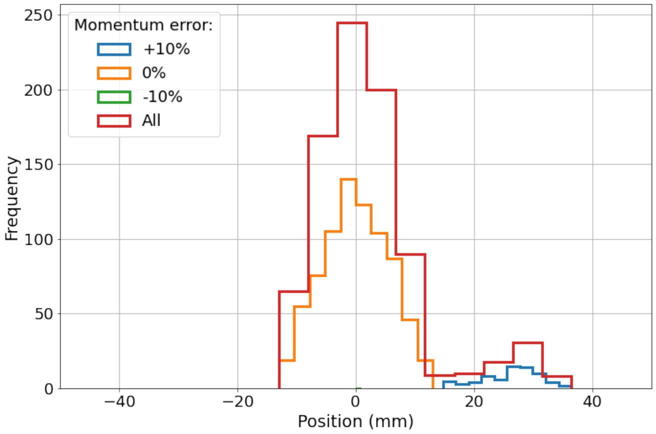

(c) Jaws closed to ±30 mm.

Figure 4.12: Histograms showing the position of particles with +10% $\Delta p/p$ (*blue*), 0% $\Delta p/p$ (*orange*), and -10% $\Delta p/p$ (*green*) after a four-bend achromat, and how these contribute to the asymmetry in the overall beam spot (*red*). This is shown in the cases when the jaws are (a) fully open, (b) closed to ±60 mm, and (c) closed to ±30 mm.

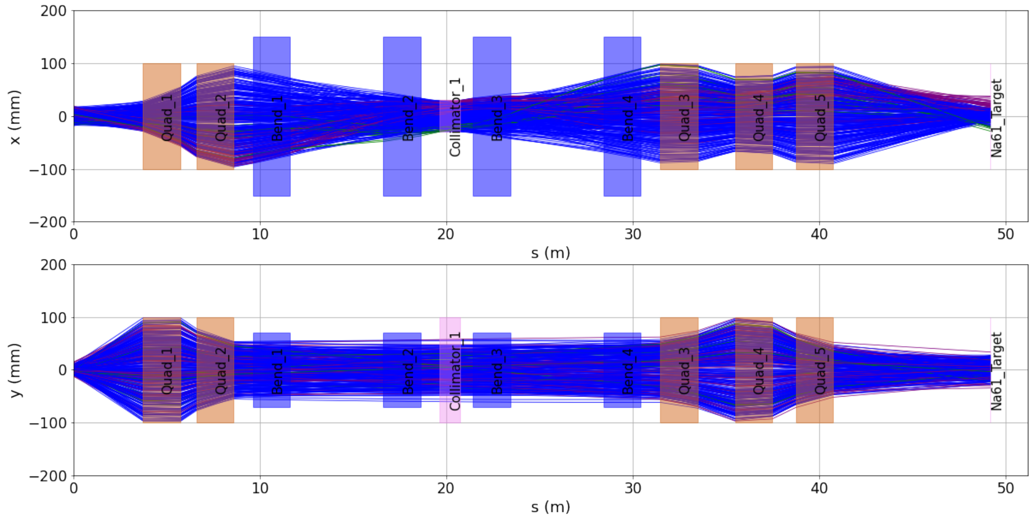

Figure 4.13: The tracks of particles being transported by the beamline at a nominal momentum of 13 GeV$/c$. With this, it is possible to visualise the behaviour of the beam both in the horizontal plane (*top*) and in the vertical plane (*bottom*). The NA61/SHINE experiment target is at the end of this beamline. A track's colour represents the percentage difference, $\Delta p/p$, between that particle's momentum and the nominal momentum. For blue lines $\Delta p/p < 5\%$, for green lines $5\% \leq \Delta p/p < 10\%$, and for orange lines $10\% \leq \Delta p/p < 20\%$.

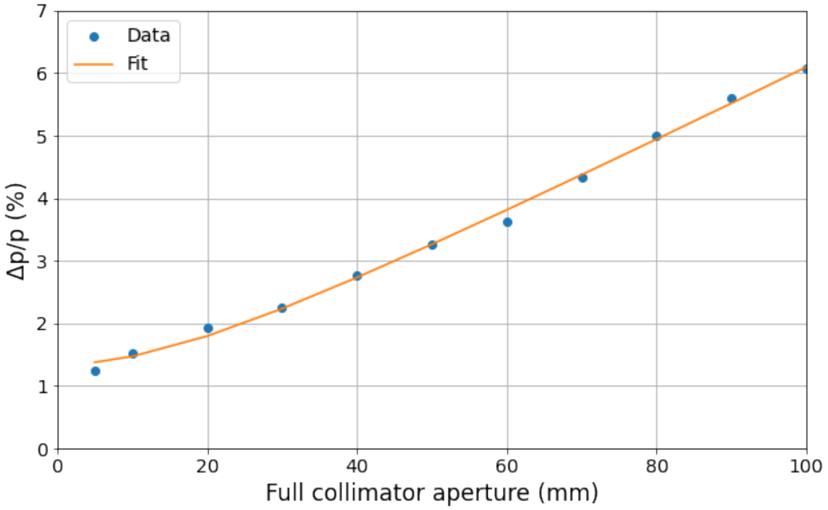

Figure 4.14: The momentum error of particles arriving at the NA61/SHINE target as a function of the aperture of the collimator. The dots are the values obtained from PTC data whereas the line represents the theoretical fit.

4.5 Comparison of the Parameter Scan to Matching Techniques

The best way to show how the parameter scan methodology improves the results that can be obtained when designing beamlines is to compare a beamline optimised with this technique to one obtained via matching. In this section this is done by comparing and contrasting the front end obtained for the low-energy beamline to one obtained via matching.

Matching

To begin this comparison, new possible optics for the front end of the low-energy beamline were calculated using TRANSPORT due to its ease of use with matching techniques. Here, the starting quadrupole strengths for both quadrupole magnets were arbitrarily set to unity and allowed to vary freely by the computer program. Additionally, the starting drift lengths were minimised between Q1 and Q2 and between Q2 and B1. This has been done following the recommendations found in Ref. [76] and Ref. [77]. The drift between the target and Q1 has been set to 4 m but allowed to vary freely. Finally, the matching conditions selected were: $R_{12} = 0$ and $R_{44} = 0$ to have a point-to-point focusing in the horizontal plane and point-to-parallel transfer in the vertical plane, what would be done conventionally when matching.

TRANSPORT was able to match these requirements as shown in Fig. 4.15, without needing to vary the distance between the target and Q1.

Parameter Scan

The optics obtained using the parameter scan technique, whose methodology is described in previous sections, can be seen in *Figure* 4.16.

4.5.1 Comparison of the Two Results

While the two optics may at first glance seem rather similar, there are actually some significant differences when comparing how they behave using PTC. In this specific case, when using simulations of particles having been produced by the high-intensity tungsten

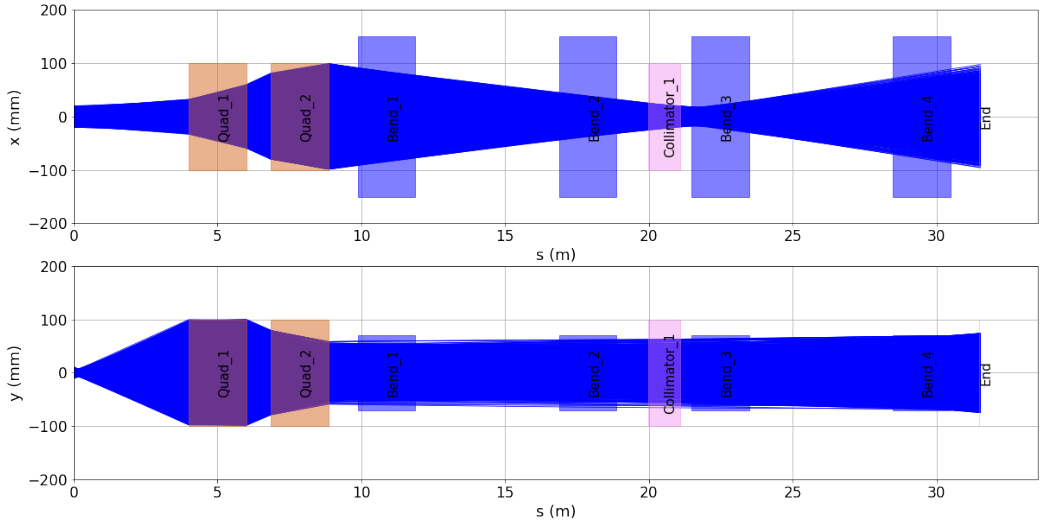

Figure 4.15: The optics calculated using matching routines. *Top*: horizontal plane, *bottom*: vertical plane.

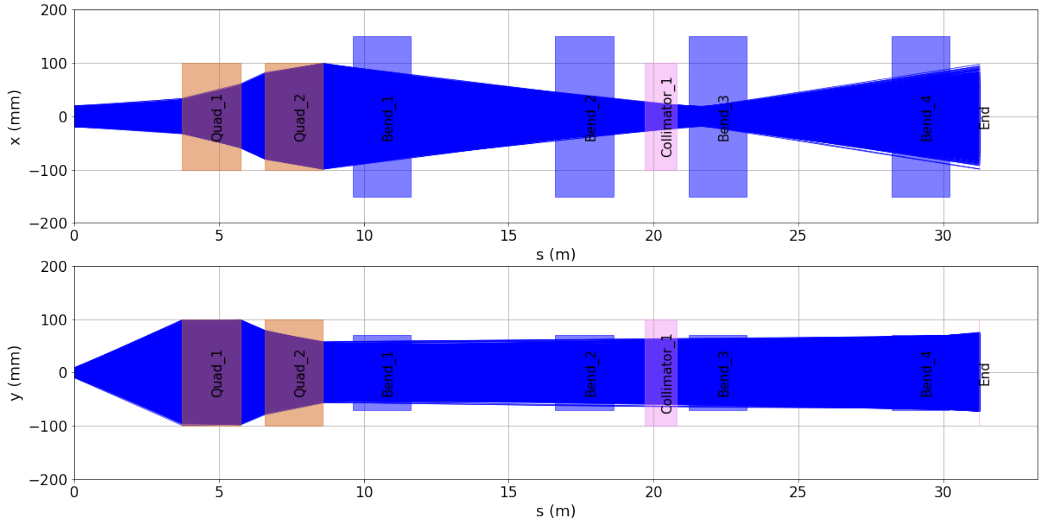

Figure 4.16: The optics calculated using the parameter scan methodology. *Top*: horizontal plane, *bottom*: vertical plane.

target, one finds that the parameter scan methodology produces a beamline which accepts approximately 10% more particles than the one obtained using TRANSPORT. Using this specific target file, 10% more particles were transported when the beamline obtained using the parameter scan was simulated.

The difference arises from the different phase spaces these two beamlines are capable of transporting to the end of the beamline, which are shown in *Figure* 4.17a and in *Figure* 4.17b.

It is important to note that the overall acceptance of the beamline is not sufficient for assessing the number of particles that will be transported to the end of the beamline. One must also convolve this acceptance with the distribution of particles produced by the target. For the optimal target of the NA61/SHINE low-energy line, developed in this thesis, the initial phase-space distribution can be seen in *Figure* 4.18, and this distribution's effect on the accepted phase space of the optimised front end can be seen in *Figure* 4.19. From this image, it is clear that there are significant areas of phase space that are accepted by the beamline and yet do not contain any particles. Future work will attempt to address this by attempting to maximise the area of phase space weighted by the distribution of particles, however the latter is dependent on the energy being studied, so to not lose generality, this was not attempted when first designing this methodology.

Additionally, when using matching techniques no considerations whatsoever are given to chromatic aberrations and second-order effects. These however can have a large effect on both the particle rates and other figures of merit, as has been discussed in Section 4.4.2, and so significant effects may be completely missed when designing beamlines.

Overall, the parameter scan technique, despite being slower, offers a more accurate way of optimising the beamline around the desired figures of merit, tackling simultaneously second-order aberrations that may significantly affect the beamline's overall performance, especially when large momentum spreads ($> 10\%$) and large angles (> 10 mrad) are present.

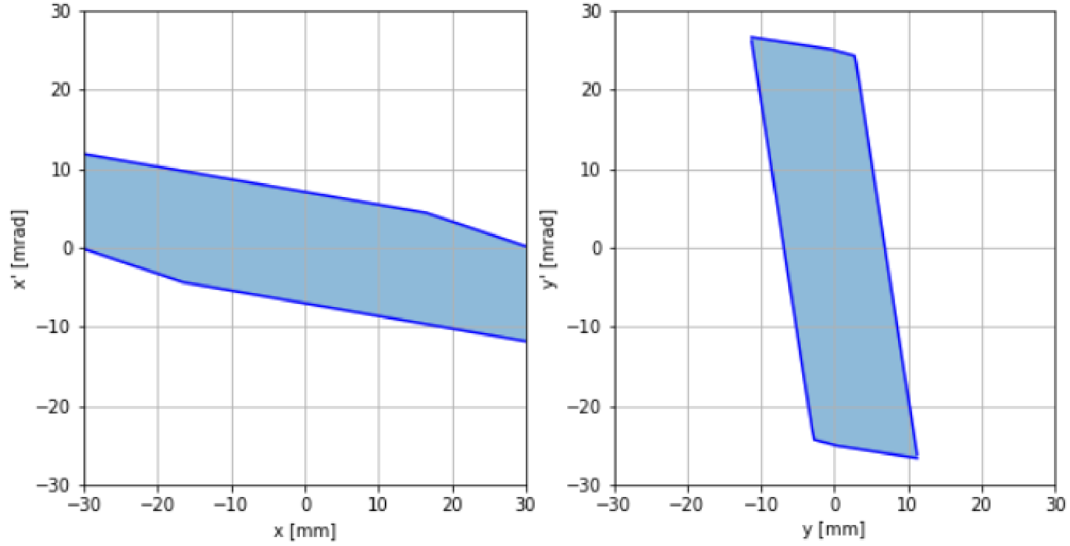

(a) Phase space from TRANSPORT

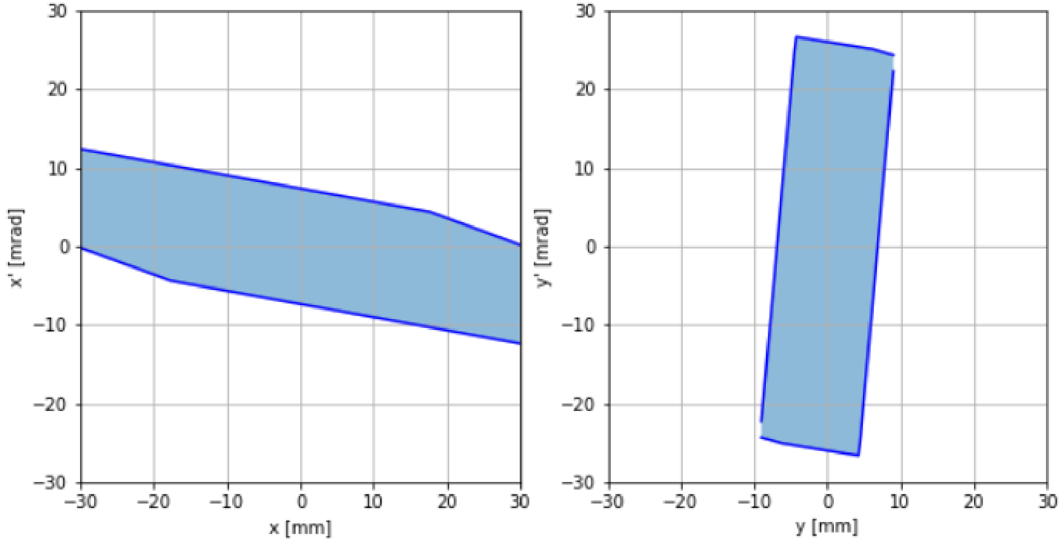

(b) Phase space from the parameter scan

Figure 4.17: The approximated theoretical acceptance of the beamline obtained using (a) TRANSPORT and (b) the parameter scan. Even if numerically the two accepted phase space areas are similar, the difference in the orientation of these leads to a higher particle rate in the beamline obtained using the parameter scan.

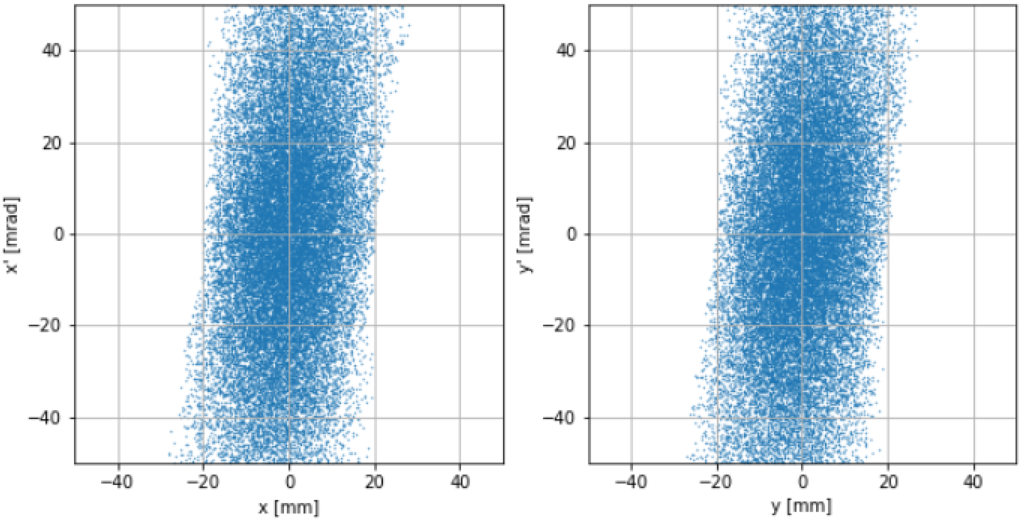

Figure 4.18: The phase-space distribution of particles immediately after the secondary target

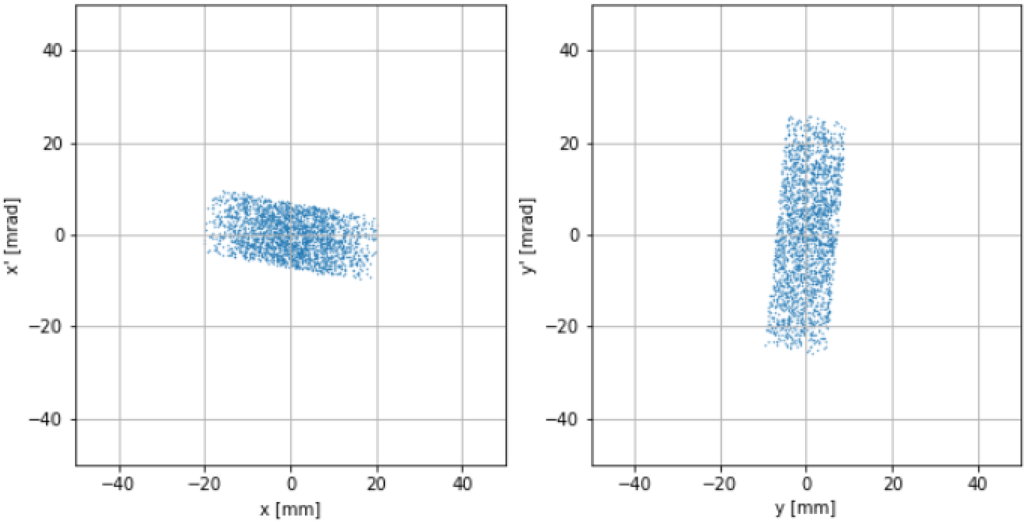

Figure 4.19: The acceptance of the beamline obtained using the parameter scan

Chapter 5

Beamline performance

Once a beamline has been designed it is important to understand how it will perform. With data obtained with MAD-X PTC it is possible to understand the trajectories of particles in the beamline, however, more specialised Monte-Carlo based simulations are necessary to understand the expected performance of the beamline. Specifically, in this chapter, G4Beamline simulations of the newly designed low-energy branch will be presented after this has been implemented in the existing H2 beamline's Monte-Carlo simulation model. This will enable the accurate simulation of the production of particles, their transport, including particle decays, interactions with apertures, and material effects on the size of the beam. Additionally, magnetic field maps and their effects on the beam will be addressed in this chapter, alongside a beam dump needed to intercept the 400 GeV/c primary protons. The importance of this is only apparent when using accurate dipole models.

5.1 Implementation of the Low-Energy Beamline in H2

The first necessity was to modify the existing simulations of the H2 beamline to include the low-energy beamline. This not only involved removing the section of H2 which will be modified, but also developing new optics to deliver a focused beam from the beginning on H2, in TCC2, to the low-energy target which will be the start of the low-energy optics.

5.1.1 A Combined G4BL Input for H2 and the Low-Energy Line

The low-energy beamline had to be included into the existing models of the H2 line in the North Area. To do this, significant modifications had to be performed to the existing input to remove all the magnets, collimators and instrumentation that will be displaced for the low-energy line while also maintaining the equipment that will not be removed, namely everything before the sixteenth quadrupole of H2. G4BL's graphical output of the setup of the currently used H2 and the modifications which have been performed can be seen in *Figure* 5.1.

5.1.2 Tuning the H2 Beamline

To focus the primary beam onto the new, low-energy target, discussed in Chapter 3, the beamline elements of H2 which will not be modified by the low-energy beamline have been used to calculate new optics. These elements consist of all magnets up to Q16, a QNL quadrupole magnet located at s=480. The new optics will be necessary to focus the 400 GeV/c beam, ensuring all delivered particles will impinge onto the low-energy target.

To calculate these optics, simple matching techniques have been used in TRANSPORT, by modifying the magnetic gradients of the last four quadrupoles in H2 before the low-energy target, such that the point-to-point matching conditions, $R_{12} = 0$ and $R_{34} = 0$, were met. These were sufficient as the H2 beam can be assumed to arrive from a point-like source [78]. These new optics can be seen in *Figure* 5.2. All magnetic strengths which are required for these optics can be easily achieved by the QNL and QWL dipoles used in H2.

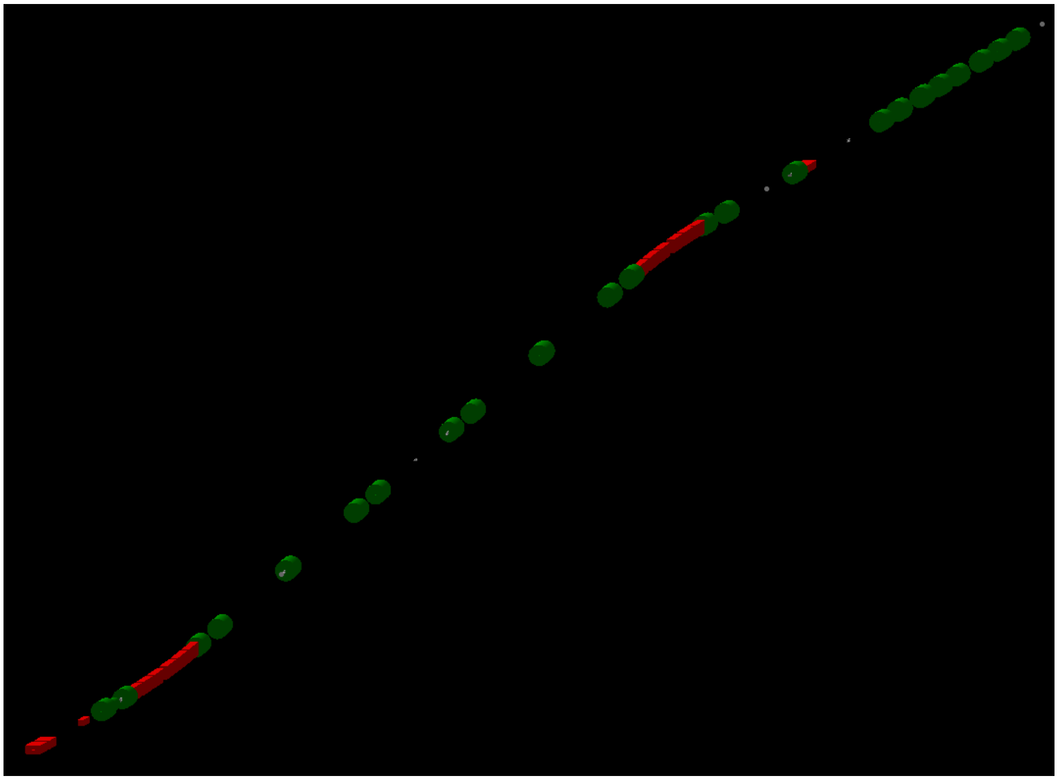

(a) Existing H2

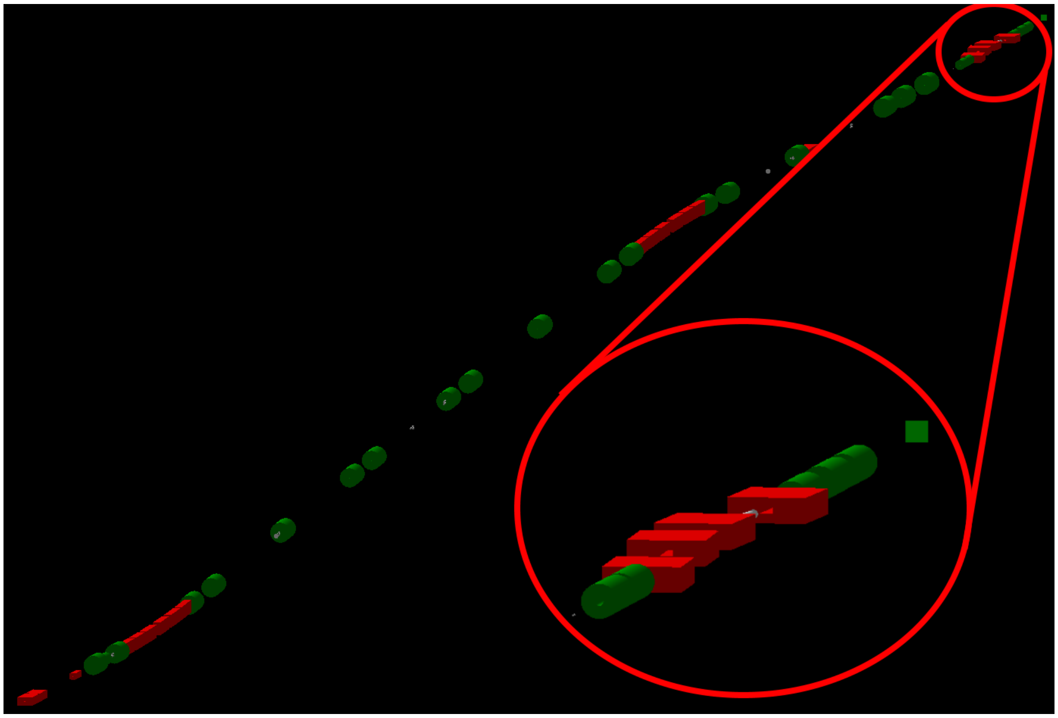

(b) H2 including the new low-energy branch.

Figure 5.1: The G4BL model of (a) the H2 line and (b) the H2 line with the low-energy line. Dipole magnets are shown in red while quadrupole magnets are shown in green.

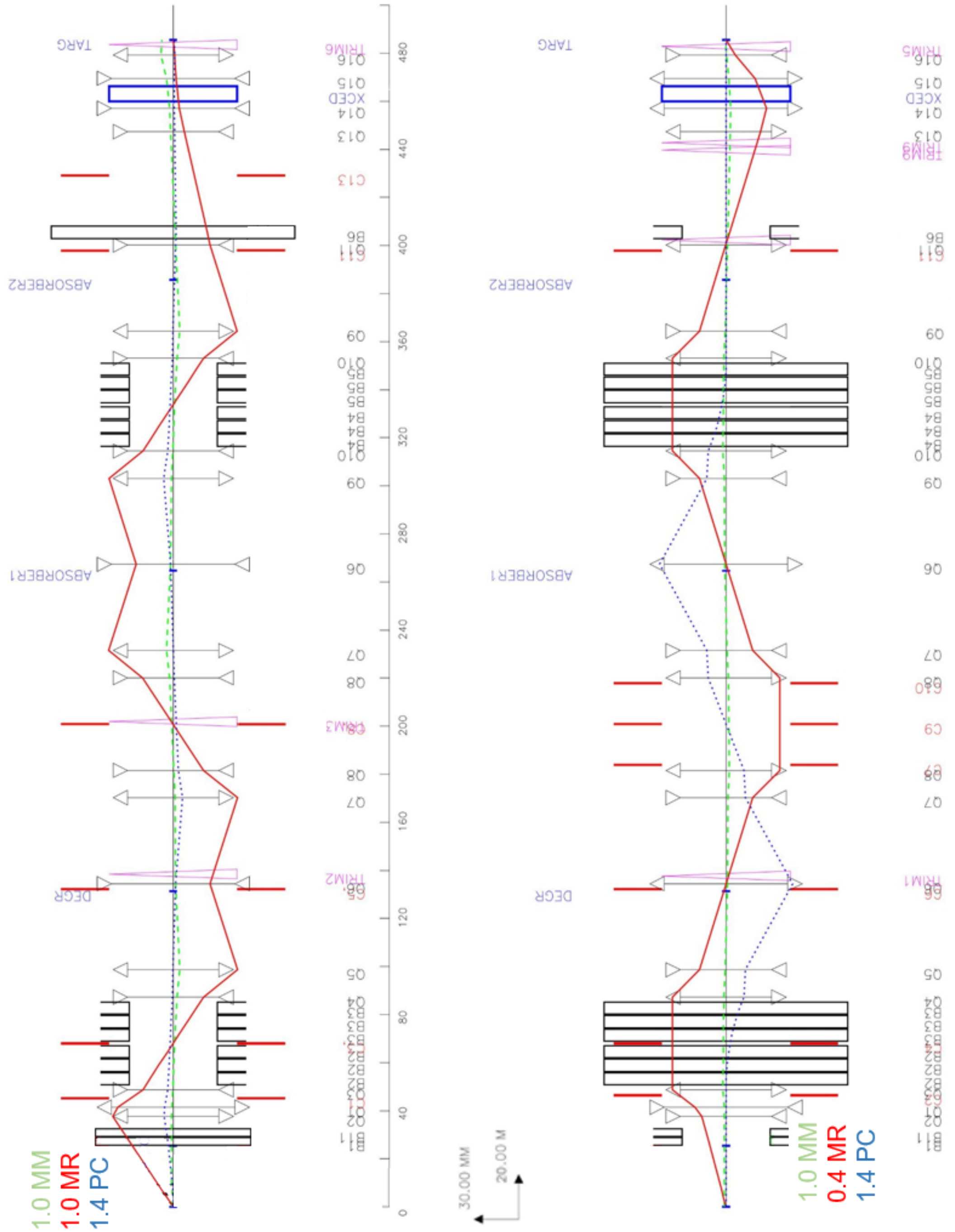

Figure 5.2: The optics of H2 which will be used during low-energy operation. *Top:* the horizontal plane with the R_{11}, R_{12}, and R_{16} terms shown in green, red, and blue respectively. *Bottom:* the vertical plane with the R_{33}, R_{34}, and R_{36} terms shown in green, red, and blue respectively.

5.2 Beamline Performance

Having created a model of the beamline in both MAD-X and in G4BL, it was now possible to simulate it and ensure that it would meet the requirements set out by NA61/SHINE described in Section 4.1 and repeated here for convenience in *Table* 5.1. Using G4BL, and measuring the properties of all particles reaching the NA61/SHINE target, it was possible to obtain estimates for the particle rates, the beam-spot size, and the momentum spread of particles. Chromatic aberrations and asymmetries in the momentum distribution can also be seen here, as predicted by the MAD-X PTC simulations from the previous chapter.

Parameters	Requirements
Desired particles	p, $\pi^{\pm}$, $K^{\pm}$
Momentum	2-13 GeV/c
$\Delta p/p$	$< 5\%$
Minimum rate	50 Hz
Maximum rate	$< 1.5 \times 10^4$ Hz
Beam-size RMS (at NA61/SHINE target)	20 mm

Table 5.1: The figures of merit necessary for the low-energy beamline measurements, from Ref. [17].

5.2.1 Monte-Carlo Simulations Overview

In order to simulate the beamline, the input file described in the previous section has been used. This uses an accurate description of the beam produced in TCC2, with the beam properties described in *Table* 5.2. The simulations were performed with the FTFP_BERT physics list and simulated 10^6 initial primary 400 GeV/c protons, the optimal primary energy found during the target studies and a reasonable, albeit likely underestimated number of protons per spill, to be conservative with the radiation protection rules. The target used to produce the secondary particles was a 20 cm long tungsten target with a 30 mm radius, the high-yield target found in the target studies.

Parameter	Value
δx	0.5 mm
$\delta x'$	0.3×10^-3 mrad
δy	0.5 mm
$\delta y'$	0.3×10^-3 mrad
$\Delta p/p$	3%

Table 5.2: The initial beam distribution used in simulations [79].

5.2.2 Momentum Selection

The first figure of merit which must be discussed is the beamline's momentum resolution, as it has an important effect on the rate of delivered particles. NA61/SHINE required a narrow momentum spread, within 5%, however a better resolution can be achieved at the cost of decreased particle rates. *Figure* 5.3 shows the relative momentum distribution of particles simulated in G4BL which reach NA61/SHINE at both 2 GeV/c and 13 GeV/c nominal momentum. The distribution of particles is peaked near $\Delta p/p = 0$, with the peak a few MeV/c lower than the nominal momentum and not symmetrically distributed. This however is to be expected as there are significant second order effects, such as chromaticity, which affect how particles of different energies behave in a beamline when the collimator jaws are not closed sufficiently. As will be demonstrated later, these effects disappear as the collimator jaws are closed further, leading to a symmetric distribution centred on $\Delta p/p = 0$.

The beamline is able to achieve the desired momentum resolution of a $\Delta p/p$ of less than 5% already with a collimator opening of ±30 mm, as the above distributions have a momentum resolution $< 4\%$ at both 2 and 13 GeV/c. However, better resolutions can also be achieved, at the cost of particle rate, by further closing the collimator jaws. The effects of closing these on the achievable momentum resolution can be seen in *Figure* 5.4. In this plot only protons, pions, kaons and positrons are considered. Below a full collimator aperture of 20 mm, the particle rates begin to decrease significantly, leading to large uncertainties in the results. Additionally, particles with the correct momentum begin to be removed, further leading to a possible growth in $\Delta p/p$.

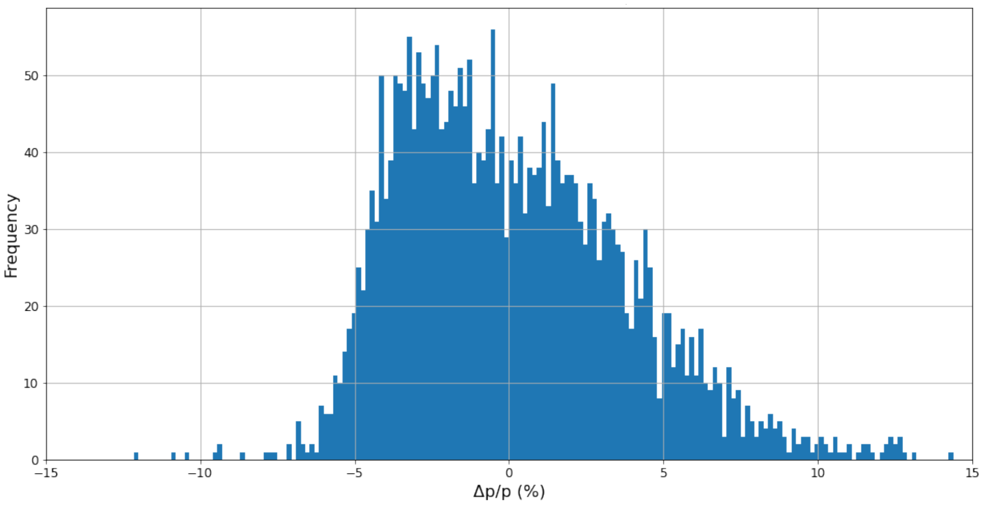

(a) 2 GeV/c

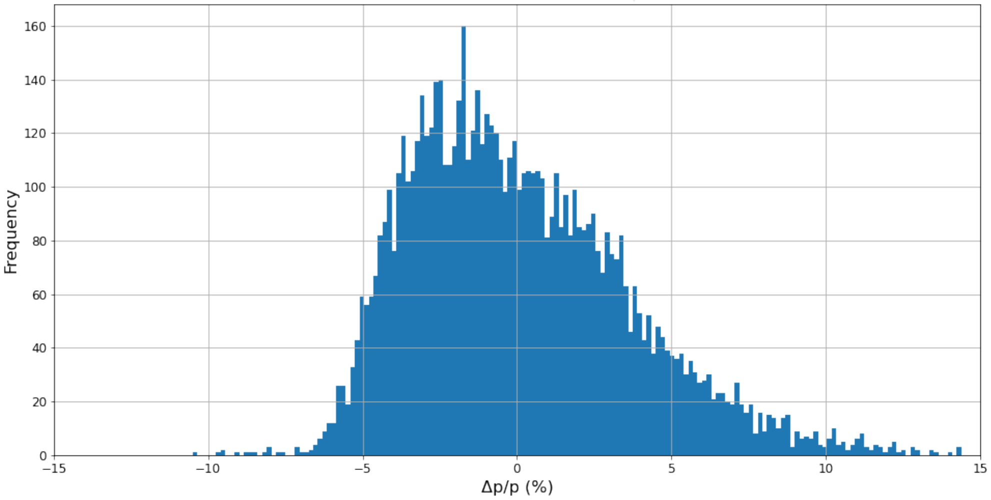

(b) 13 GeV/c

Figure 5.3: The relative momentum distribution of particles at the NA61/SHINE target. Here the collimator jaws were opened to ±30 mm, leading to a $\Delta p/p$ of (a) 3.5% at 2 GeV/c nominal momentum and (b) 3.5% at 13 GeV/c nominal momentum.

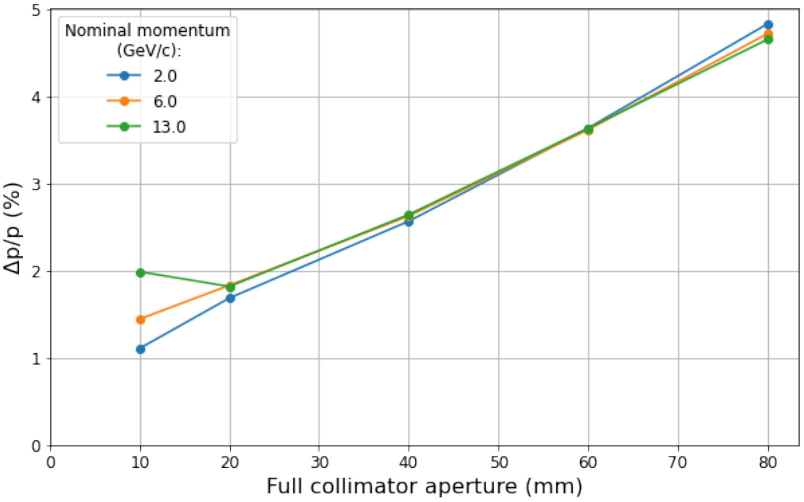

Figure 5.4: The momentum resolution of particles reaching the NA61/SHINE target as different collimator jaw openings are used to perform momentum selection.

Additionally, by plotting the momentum error on particles reaching the NA61/SHINE target, *Figure* 5.5, it is possible to clearly see how closing the jaws reduces the momentum spread by removing off-momentum particles. The figure also shows how, beyond a certain point, ±10 mm, further closing the collimator jaws does not significantly improve momentum resolution but rather it begins to simply remove on-momentum particles. This effect begins to take place when the aperture is opened to 20 mm. This is a slightly worse limit than the one predicted by PTC in Chapter 4, however, this is not surprising as the Monte-Carlo simulation includes more effects, such as particle decays and beam interactions which may broaden the beam-spot size at the collimator. Combining the results from *Figures* 5.4 and 5.5, shows that collimation of off-momentum particles up to $\sim 2\%$ can be achieved without having a significant reduction of on-momentum particles. These results have been shown for particles with a nominal momentum of 13 GeV/c, but hold for all momenta ranging from 2 to 13 GeV/c.

5.2.3 Beamline Behaviour and Particle Rates

Following this discussion of momentum resolution and its effect on particle rates, the expected yields of particles at the NA61/SHINE target can be discussed. These are pre-

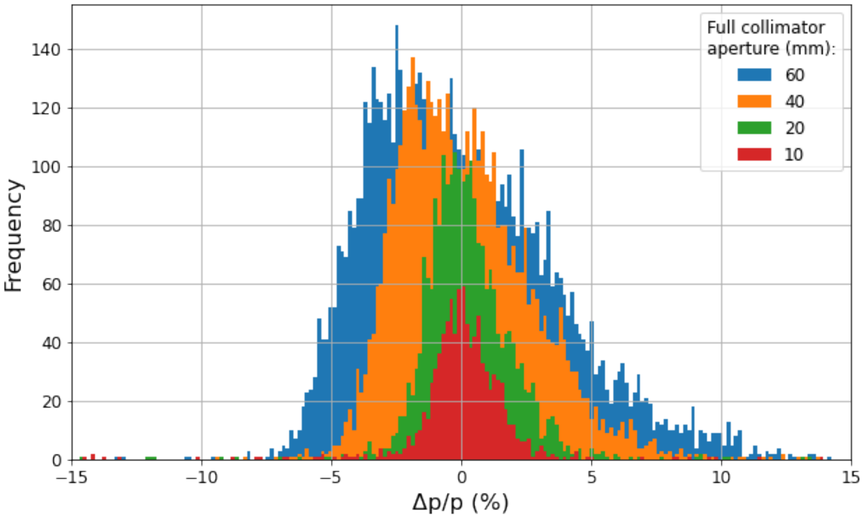

Figure 5.5: The relative momentum spread of particles reaching the NA61/SHINE target as the collimator jaw openings are varied to perform momentum selection.

sented for nominal momenta ranging from 2 to 13 GeV/c, and with a ±30 mm collimator aperture can be seen in *Figure* 5.6. This collimator aperture has been chosen as it provides a sufficiently small momentum spread, however, later particle rates for a ±10 mm collimator aperture are also presented. In this section, error bars can be estimated to be approximately 10%, as discussed in Chapter 3.

As can be seen, the particle rates change significantly over the momentum range of the beamline, due to the different initial distributions of particles and particle decays. The histogram shown in *Figure* 5.6 has also been converted into a table showing the particle rates at a nominal momentum of 2, 6 and 13 GeV/c by dividing by the 4.8 second long SPS spill. This can be seen in *Table* 5.3 and can be used to compare the expected rates with NA61/SHINE's requirements. In addition, this table also presents the particle rates with the collimator jaws closed to ±10mm, to achieve the smallest momentum spread.

At 13 GeV/c, pions dominate the beam composition, with a significant number of protons and kaons also reaching the target. Here, the number of interactions from the leptons, namely the positrons and muons are a small background, which will be easily identified and rejected via particle tagging, discussed in Chapter 6, and vetoing of the

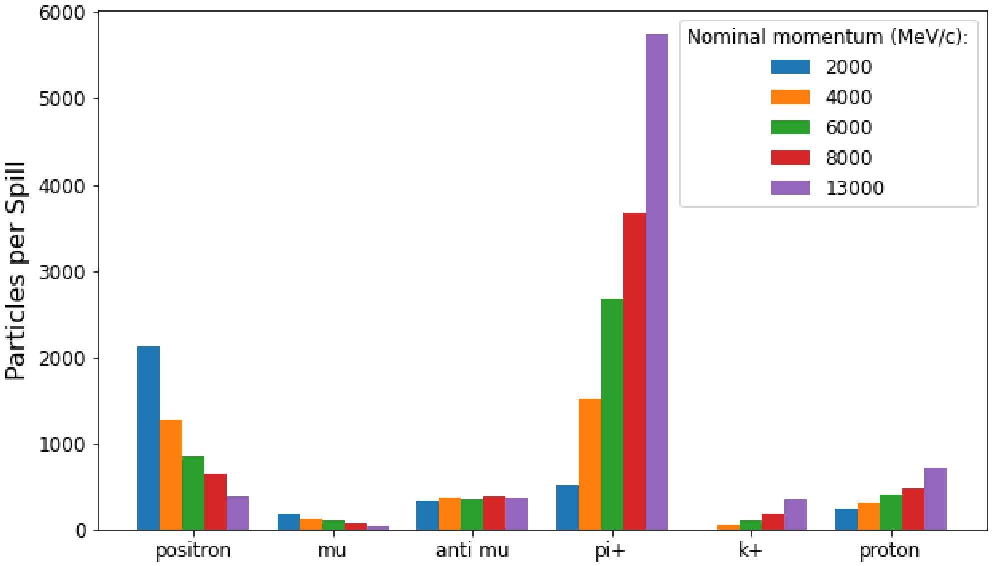

Figure 5.6: The number of particles from 2 to 13 GeV$/c$ reaching the NA61/SHINE target from one SPS spill of 10^6 primary protons.

event. At lower energies, on the other hand, the signal from pions is lower and the signal from kaons is zero. This is expected as the lower momentum particles are more likely to decay in the beamline and also, since these particles experience a smaller Lorentz boost, they are produced already in a larger area of phase space, meaning that low energy particles are less likely to be produced within the phase-space acceptance of the beamline. In the low-momentum regime, the signal arising from positrons is larger. This is likely due to how these particles are produced, mainly from bremsstrahlung, a process producing exponentially more low-energy particles. Even with these considerations, however, the rates presented above are well within the requirements of NA61/SHINE.

5.2.4 Beam-Spot Studies

NA61/SHINE have requested a beam with an RMS size in both the horizontal and vertical planes of less than 20 mm. These requirements, as can be seen in *Figure* 5.7, can be met at both 2 and 13 GeV$/c$ and therefore at all intermediate values too if the material budget incurred from the instrumentation for particle-by-particle identification is not included.

Collimator opening (mm)	Particle	Rate at 2 GeV/c (Hz)	Rate at 6 GeV/c (Hz)	Rate at 13 GeV/c (Hz)
60	π^+	107	559	1196
	Proton	49	85	149
	K^+	0	22	74
	e^+	445	177	79
	μ^+	69	73	78
20	π^+	31	174	378
	Proton	19	23	45
	K^+	0	4	22
	e^+	139	57	25
	μ^+	50	42	41

Table 5.3: The expected particle rates at the NA61/SHINE target at a range of useful momenta per 10^6 primary protons. A ±10% error can be assumed on these figures.

These material effects are discussed in Chapter 6. With these results, along with those shown in the previous sections, it can be concluded that this beamline design is suitable to meet all the requirements of NA61/SHINE.

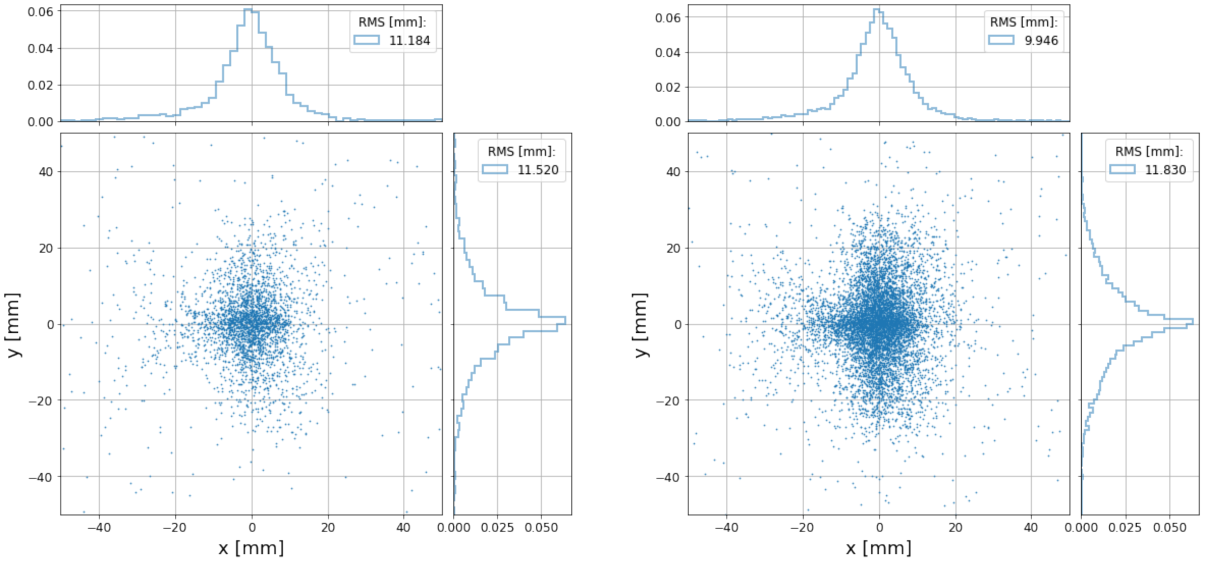

(a) 2 GeV/c

(b) 13 GeV/c

Figure 5.7: Scatter plots of the (x, y) coordinates of particles at the NA61/SHINE target at (a) 2 GeV/c and (b) 13 GeV/c. In these simulations, the collimator jaws were opened to ±30 mm.

5.3 Using Magnetic Field Maps in Simulations

In G4BL particles travelling through the iron yoke of magnets are suppressed by default [80] as the program does not model magnetic fields within the magnet iron. It is possible to keep these particles, however this introduces inaccuracies in the simulations due to the lack of magnetic fields . This behaviour, while acceptable for initial approximations, is not ideal and does not provide a sufficiently adequate description of how the beamline will perform in reality. In this section, the development of accurate magnet models and magnetic field maps to be used in G4BL is outlined, followed by a study of the effects of using them on the beamline's figures of merit. Further, in-depth analyses of tuning factors, scalar values used to re-scale magnetic fields to account for differences between idealised magnets and more realistic field maps, are also included.

5.3.1 Models of CERN Magnets in G4BL

The default *genericbend* and *genericquad* dipole and quadrupole magnets generated by G4BL are rather simple models of the magnets. These are shown in *Figure* 5.8, and are,

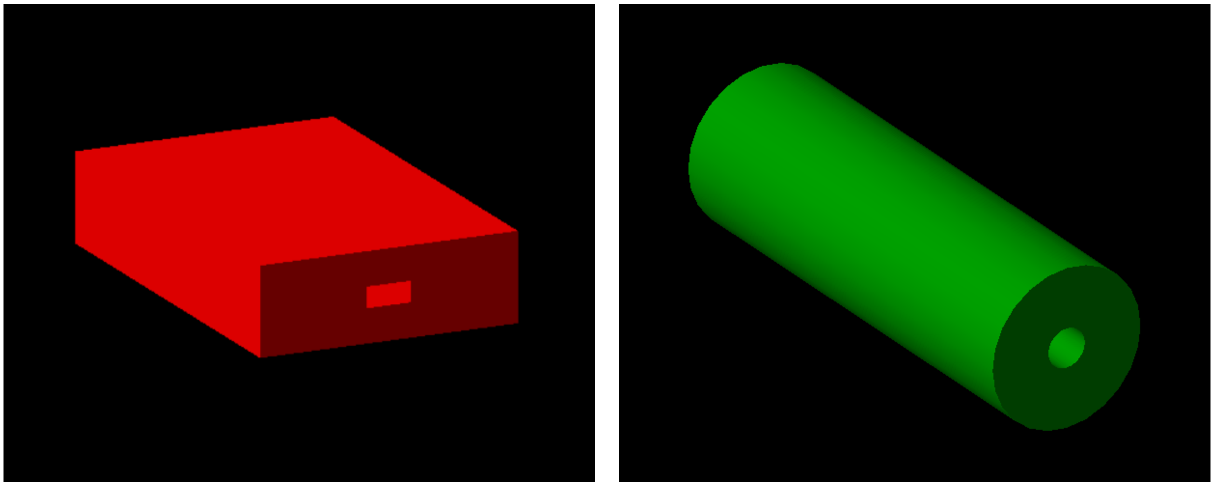
(a) (b)

Figure 5.8: The default (a) dipole and (b) quadrupole magnets generated by G4BL.

geometrically speaking, as simple dipoles and quadrupoles as possible. The *genericbend* is a rectangular box whose material, size, and aperture size can be selected by the user, however it is limited to being made of one material and, as mentioned earlier, particle tracking within the yoke of the magnet is not performed by default. While this can be changed, the magnetic field in the iron is nonetheless not simulated, and therefore of limited use. The *genericquad* is a similarly simple cylinder whose material, inner and outer radii can be modified by the user. These, while good initial approximations of the MBPL and QPL magnets, can be significantly improved.

To this end, G4BL provides a quite extensive framework for the creation of custom elements by adding, subtracting and rotating some fundamental 3-D shapes, which can be used to generate much more accurate models of the magnets used in the beamline. This process has been used to generate models of QPL and MBPL magnets which have the same dimensions and materials as the ones used at CERN. These magnets can be seen in *Figure* 5.9. The different colours are to show the different materials used in these magnets. These models have been designed following the specifications given in CERN's magnet guide [73].

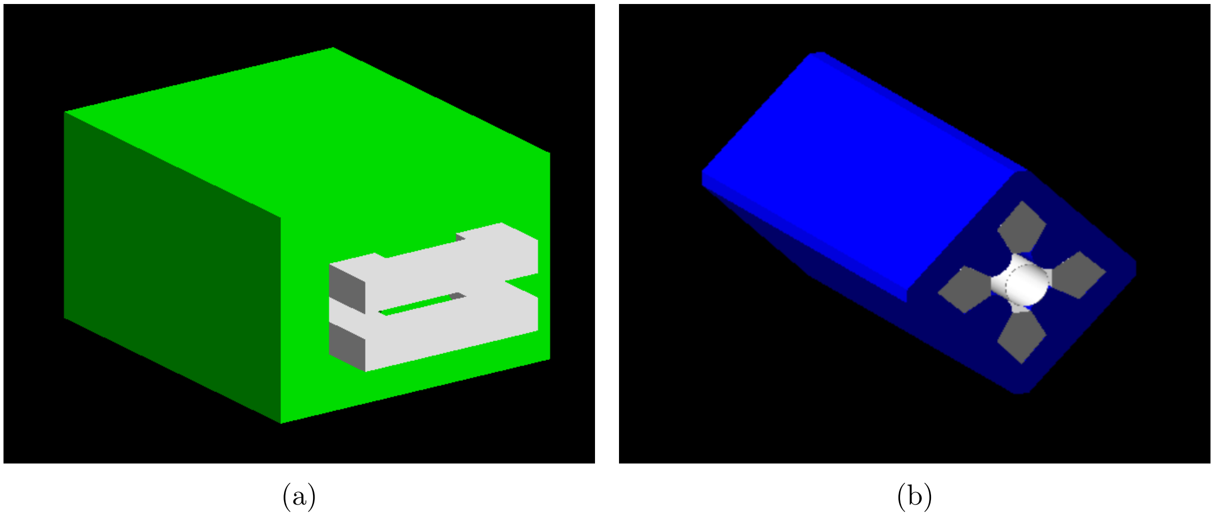

(a) (b)

Figure 5.9: The custom models developed in the framework of this thesis for (a) an MBPL dipole and (b) a QPL quadrupole.

5.3.2 The Field Maps

The geometric models are not the only simplification in G4BL's approach of magnetic simulations, but there are also significant differences between the the magnetic fields which are simulated and reality. In the core of dipoles, the magnetic field is modelled as a pure, idealised, $\bar{B} = (0, B_y, 0)$ and the quadrupoles have their fields modelled via $\bar{B} = (K \cdot y, K \cdot x, 0)$, while in the iron, the field is always assumed to be zero. This is not the case in real magnets, both in terms of the idealised fields and in the iron. Additionally, while G4BL attempts to model the fringe fields using a model based on Cosy Infinity [80], this depends on six parameters which cannot be determined straightforwardly for the magnets used in the beamline, leading to inaccuracies in the tracking. To avoid issues which may arise from incorrect tracking of particles travelling within the beamline, and of muons and other backgrounds, rather than relying on the inbuilt field maps used in G4BL it was important to also assess the low-energy beamline's performance when using accurate field maps generated specifically for the QPL and MBPL magnets. These were produced in OPERA [81][1] and provided the value of the magnetic field at several points along a grid.

---

[1] The simulations were performed by Philip Schwarz in CERN's Technology Department

For the QPL magnets, field maps spanning the whole length of the magnet were not available, however highly precise field maps of the centre of the magnet were available alongside an equally precise field map of the ends of the magnet, to account for the fringe fields. These field maps provided the field in the x and y directions from the centre of the magnet to $x, y = 600$ mm, well beyond the magnet iron, with the central field map presenting the magnetic field in the centre of the magnet, and the fringe field map providing data from $z = 800$, far from the effects of the fringe fields, to $z = 1300$, where the magnetic fields approach 0. These two field maps were then scaled and combined to provide a full field map of the quadrupole magnets. Entire field maps for the MBPL magnets on the other hand were available, and so these were used directly.

The vertical and horizontal magnetic fields of the G4BL *genericbend* magnets and the MBPL field maps can be seen in *Figure* 5.10. Here, both magnetic fields have been scaled to have a peak field of 1 T, and as can be seen generally behave rather similarly with only minor differences near the end of the magnet, at $z = \pm 1000$ mm. In the transverse plane, the fields are similar in the central region, however, the MBPL field map has a larger region of good field and drops off more slowly than the G4BL map. Finally, the latter also lacks any simulation of the magnetic field in the iron, which the MBPL map attempts to simulate.

The differences between the magnetic fields of the G4BL *genericquad* magnets and the QPL field maps were also rather small within the magnet's centre, however these become more significant at the edge of the quadrupole. These can be seen in *Figure* 5.11, where the percentage difference between the total magnetic fields at different points along the quadrupoles is shown. In the image, the locations in white correspond to the iron core of the quadrupole, and have been ignored as G4BL does not provide values for the magnetic fields in these locations. The percentage difference in magnetic field was chosen as it was the easiest to visualise when considering the more complicated magnetic field of quadrupoles compared to dipoles, however the difference between the individual components of the magnetic field can be found in Appendix C. As can be seen in the

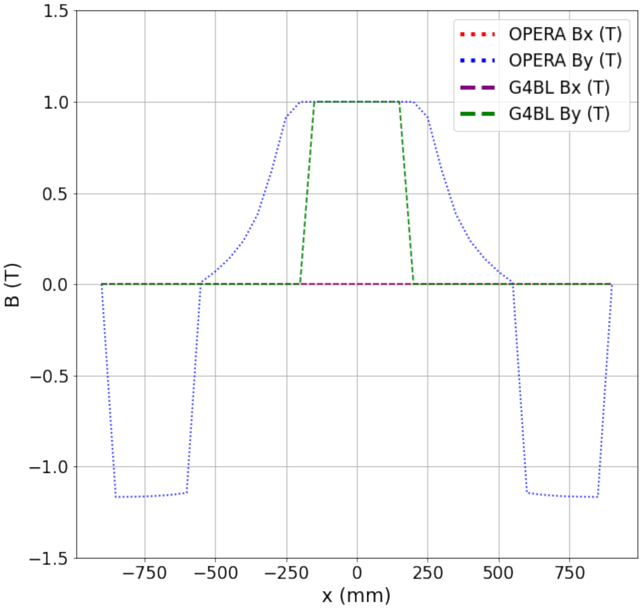

(a) Magnetic field as a function of transverse position.

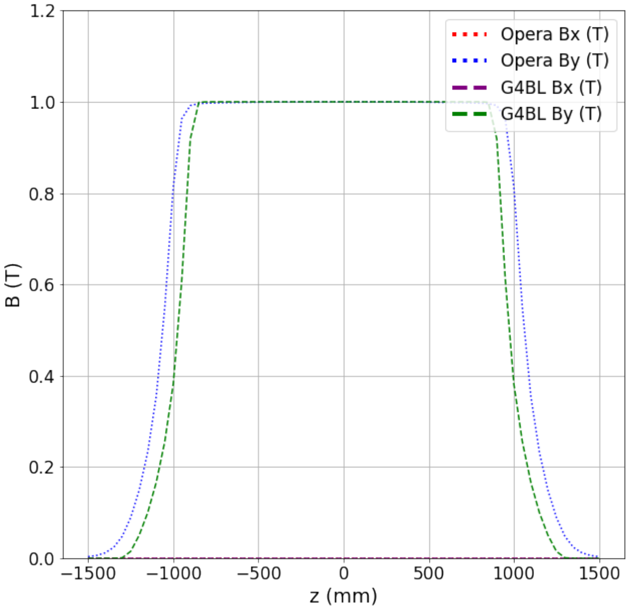

(b) Magnetic field as a function of longitudinal position.

Figure 5.10: Comparison of the vertical and horizontal magnetic fields of the G4BL *genericbend* magnets and the MBPL magnets.

image, there is good agreement between the two simulations when more than ~ 100 mm from the edge of the quadrupole, located at $z = \pm 1000$ mm. As one approaches the end of the quadrupole, the differences between these maps increase, reaching at times errors over 100% at the edges of the magnet before then beginning to decrease again.

These discrepancies are mostly a product of the magnetic fields in the x and y directions at the very end of the magnet, as here the differences are on the order of up to ~ 0.5 T, however smaller discrepancies in the magnetic field in the z direction are also present. These differences lead to changes of the beamline's optics and the transport of particles.

5.3.3 Magnet Tuning

Due to the differences between the generic and the realistic field maps, the optics in the beamline may be different between the idealised and real-world scenarios. This is because, due to the different focusing and bending, the location of the focal point of the optics and the reference particle's trajectory may change. To counteract these effects, it is customary to *tune* the magnets, meaning that rather than running at the previously defined optimal current, these magnets would run at a new *working current.* To calculate this new working current two different techniques were used for dipoles and quadrupoles.

For the dipoles, the process was straightforward. As the main concern with these is to ensure that the reference particle's trajectory is unchanged, a good first approximation of the scale factor between the two is simply given by the ratio of the integrated magnetic field of the *genericbend* and the MBPL field map. Additional fine tuning can then be performed by modifying modifying this starting value to ensure that the beam is centred as desired. With these two techniques, the scaling factor for dipoles was first found to be 0.9208, and then improved to 0.9212, until sub mm agreement was achieved between simulations performed using the two different field maps.

The tuning for the quadrupoles on the other hand is more complex, due to the different focusing and de-focusing effects in the two planes. Because of this, a custom Python script has been created which numerically calculates a scale factor to ensure the closest agreement between the R-Matrix of the idealised and realistic magnets. While the R-Matrices of quadrupoles and dipoles are well known, those of the magnets which have been generated via a field map are rather different and need to be determined numerically in simulation. To this end, several particles with starting 6-D phase-space vector given by

$$X = \begin{bmatrix} x \\ x' \\ y \\ y' \\ \delta s \\ \frac{\delta p}{p_{ref}} \end{bmatrix} = \delta_{ij} \text{ for } j = 1, 2, 3, 4 \tag{5.1}$$

were simulated and transported through the field map to extract the R-Matrix elements of the new magnet. With these values, it was then possible to numerically solve for the magnetic strength, k, corresponding to each element of the R-matrix, R_{ij}, and from this new k, it was possible to find a tune factor such that $k_0 = \alpha k$, where k_0 is the original, theoretically optimal, magnetic field strength for an ideal quadrupole. This process had to be repeated for each element of the R-matrix, as often a tuning factor was not sufficient to make the two R-matrices identical. When this was the case, α was chosen such that average error was minimised.

The values of α which minimised the difference between the focusing of real and idealised quadrupole was $\alpha \approx 0.95$, meaning that to maintain the same optics, the real magnets will need to be run at a roughly 5% lower strength. This value is in agreement with what was found in previous experiments [82].

To further optimise α, several simulations were run to find the value which created simulations which most closely matched the results obtained using *genericquads*. For these simulations it was important to see whether different tuning factors had an adverse effect on the acceptance of the beamline, and more importantly the effect these have on how the optics focus the beamline. The results for particle rates using different tuning factors can be seen in *Figure* 5.12.

While the value of $\alpha = 0.97$ gives the highest particle rate, it is also important to ensure that the tuning factor does not produce an out-of-focus beam. The size of the beam spot at the NA61/SHINE target can be seen in *Figure* 5.13 for the same tuning factors as the previous figure, alongside the beam spot obtained using G4BL's default magnets. A tuning value of 0.97 maintains a sufficiently small beam spot, while having a similar particle rate as the default behaviour, as such it was chosen as the tuning factor for future simulations.

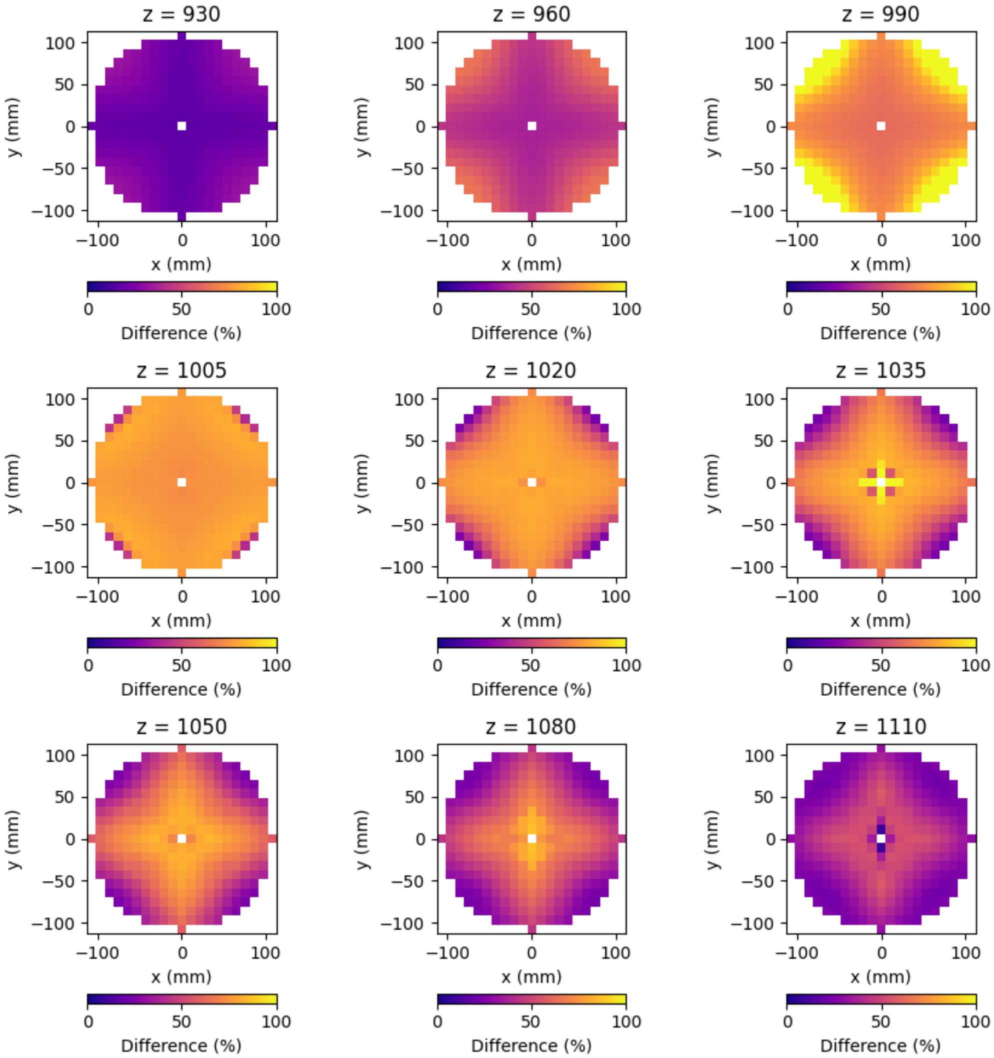

Figure 5.11: Comparison of the magnetic field maps of the G4BL *genericquad* magnets and the QPL magnets. The figure shows the percentage difference between $|\overline{B}|$ of the two quadrupoles for slices of the magnetic field at different values of z (in mm).

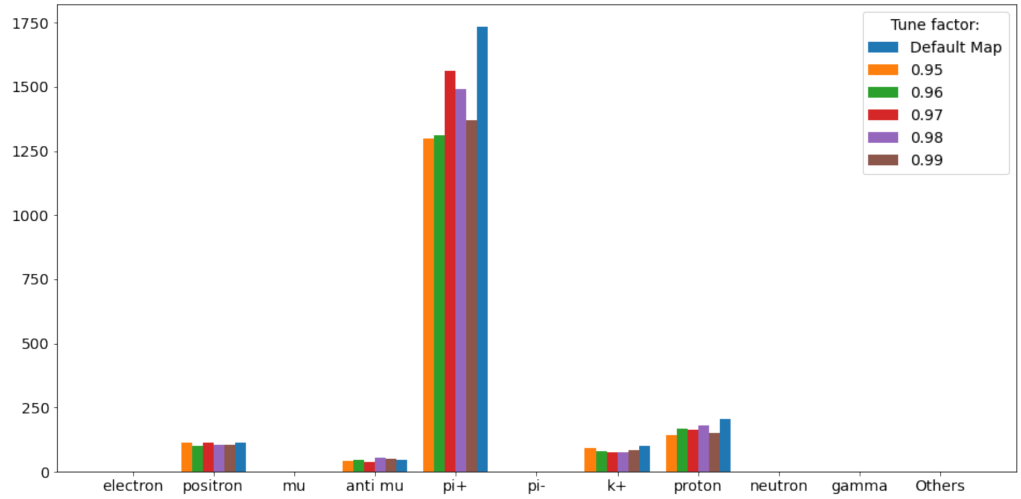

Figure 5.12: The effect of using different tuning factors with the custom field maps on the rates of several particles at 13 GeV/c.

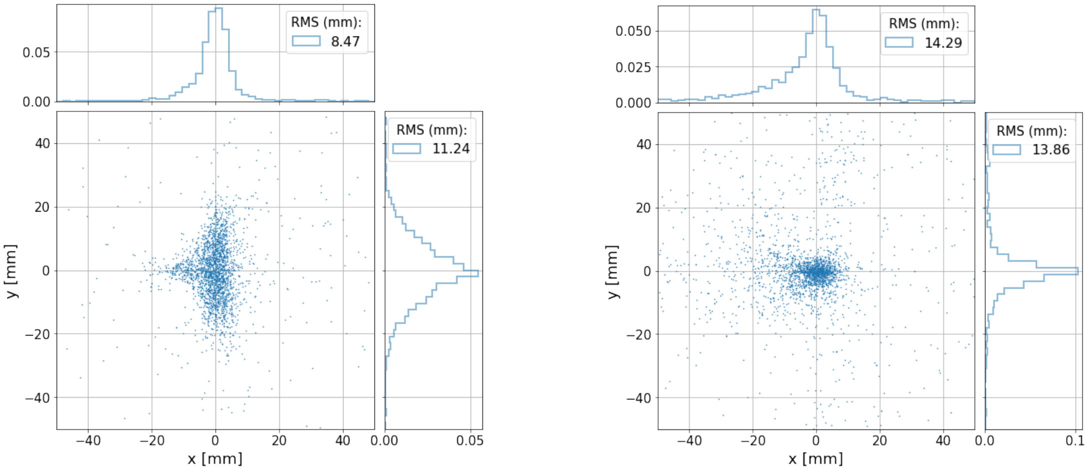

(a) G4BL default

(b) $\alpha = 0.96$

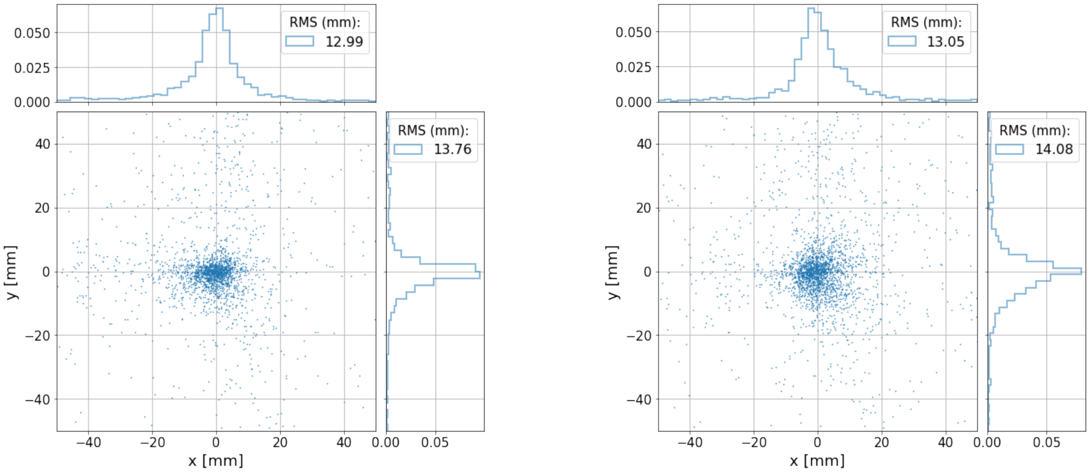

(c) $\alpha = 0.97$

(d) $\alpha = 0.98$

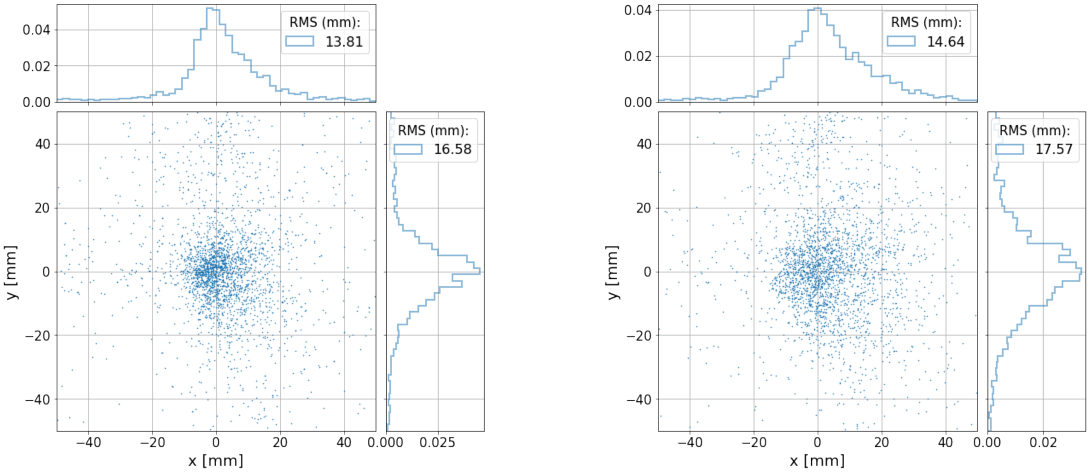

(e) $\alpha = 0.99$

(f) $\alpha = 1.00$

Figure 5.13: The $(x,\, y)$ coordinates of particles detected at the end of the beamline using G4BL's generic magnets (a), and as the tune factor is varied from 0.96 to 1 (b-f).

5.4 Beamline Performance with Field Maps

With the tune factors in mind, the simulations of the low-energy beamline using the accurate field maps were then repeated to obtain a more precise estimate of the muon background and more precise particle rates which will be delivered to NA61/SHINE. To assess the muon background at the NA61/SHINE TPC, the suppression of very low-energy particles (< 0.5 MeV/c), which was present for the other G4BL simulations, was removed. This ensured that all muons produced via pion decays would be appropriately simulated. This exponentially increased the simulation time due to the particles produced in electron showers when positrons and electrons interacted in the iron of the magnets, as such, these magnets have been set to immediately suppress any positron or electron interacting in them. This is not expected to have an effect on the muon background, however it drastically improved the simulation time.

As all quadrupoles were running at different currents, a different field map was used for each, to properly address any saturation issues which may arise. All of these field maps were within 50 A of the necessary current for the beamline, and were re-scaled to the appropriate value for use in the beamline's simulation.

It is important to note that in these simulations, a large iron beam dump has been added between the first and second dipole magnets, intercepting the path of the straight 400 GeV/c beam but off the axis of the low-energy beam. This was necessary as the 400 GeV/c primary beam, which would previously interact with the dipole magnets, now travels through their aperture, due to the more realistic magnet models. The beam dump included in the G4BL simulations is a large iron block, 1 meter tall, one meter wide, and two meters long, however further studies may optimise the dimensions further.

5.4.1 Effect of Field Maps on Particle Rates

While there is some small disagreement between the G4BL and simulated field maps, it is expected that there would be good agreement between the particle rates seen using either method, as these differences have been tackled by tuning and were only present at the ends of the magnets. This is indeed the case and can be seen in *Figure* 5.14, where the

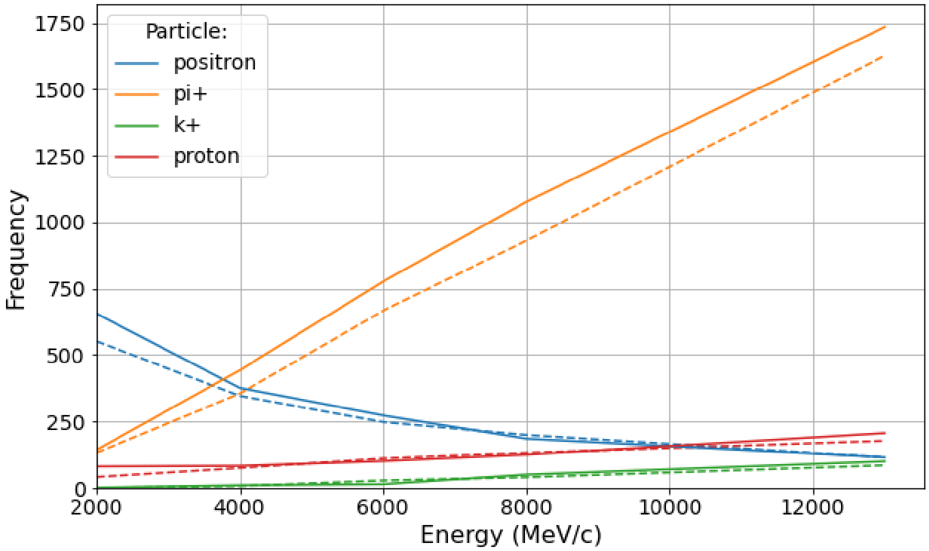

Figure 5.14: A comparison of the particle rates as a function of secondary beam energy obtained when using G4BL's generic field maps and magnets (solid line) and the custom models and field maps developed in the framework of this thesis (dashed line).

particle rates of secondaries arriving at the NA61/SHINE target (within a 25 mm radius) are considered when the collimator is opened to ±10 mm. The differences which can be seen between the two particle rates are small, generally on the order of less than 10%, and can be explained by several factors. First, the field maps may not have been scaled to the exact same values as the magnetic field maps used by G4BL. Secondly, there are differences in the geometries of magnets, especially the MBPL dipoles. Finally, there are statistical effects which may also contribute to the differences seen. Overall, these effects are not expected to cause any significant problem if the beamline were to be implemented.

5.4.2 Backgrounds at the NA61/SHINE Experiment

The other reason for implementing the realistically simulated magnets and magnetic fields is to track any muons produced by pion decays which may travel through a magnet's iron core and which may reach the NA61/SHINE TPC, rather than secondary target, causing backgrounds and possibly overwhelming the desired interactions.

To ensure that the background rate is acceptable, in these simulations the TPC has been included and simulated as a 5×5 m^2 detector placed a few metres behind the

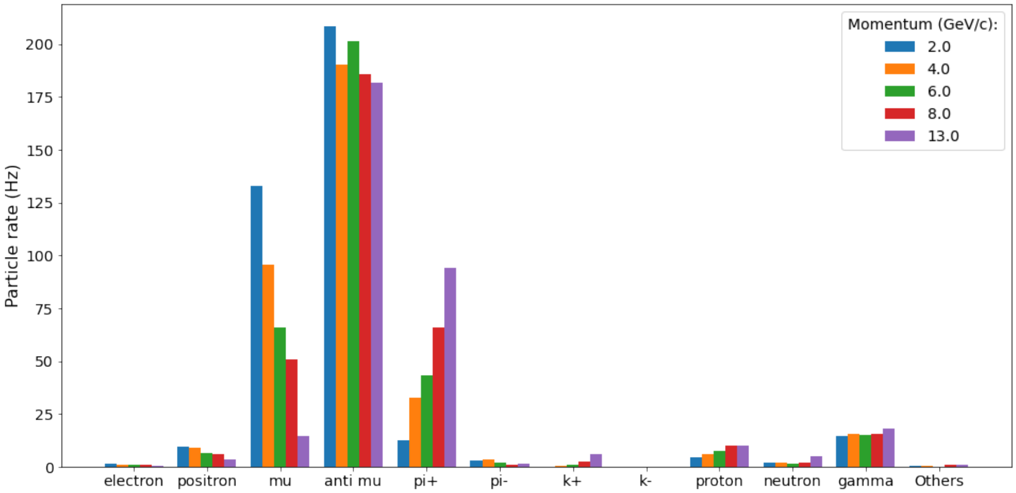

Figure 5.15: Background rates for several of momenta at the NA61/SHINE TPC detector.

NA61/SHINE target. Here, interactions have been scored as a function of beam energy to calculate a background rate by considering the 4.8 second long SPS spill.

The results can be seen in *Figure* 5.15. In these results, only particles detected outside a 25 mm radius circle have been considered background, as particles within this area are either desired particles produced by interactions with the NA61/SHINE target, or will be easily vetoed by the NA61/SHINE trigger system, described in Chapter 1. These simulations show that the backgrounds, even when overestimated, as much of the shielding in the H2 beamline was not included in the G4BL model of the beamline, are well within the 1.5×10^4 Hz limit imposed by NA61/SHINE.

5.5 Comparison of NA61/SHINE's Requirements with the Simulations

Having completed the Monte-Carlo simulations for a range of nominal momenta, it is now possible to compare the beamline's expected figures of merit with NA61/SHINE's requirements. These have been summarised in *Table* 5.4, where the specifications and the beamline's performance at 2 and 13 GeV/c have been summarised. The particle rates and momentum resolutions have been obtained using a ±10 mm collimator opening, but as discussed in Section 5.2.3, the rates are subject to change depending on the desired momentum resolution and therefore collimator opening.

All requirements set out by the experiment have been met with this beamline design, with the exception of the delivery of kaons below 4 GeV/c, which is not possible due to the small production cross section and extremely short lifetime. Aside from this, the beamline delivers all desired particles at an appropriate rate, with an acceptable momentum resolution and beam-spot size.

Parameters	Requirements	Simulation Results (2 GeV/c)	Simulation Results (13 GeV/c)
Desired particles	p, $\pi^{\pm}$, $K^{\pm}$	p, $\pi^{\pm}$	p, $\pi^{\pm}$, $K^{\pm}$
$\Delta p/p$	$< 5\%$	$< 2\%$	$< 2\%$
Minimum rate	50 Hz	> 150 Hz	> 1400 Hz
Maximum rate	$< 1.5 \times 10^4$ Hz	500 Hz	2000 Hz
Beam-size RMS (NA61/SHINE target)	20 mm	13 mm	11 mm

Table 5.4: Comparison of the figures of merit requested by NA61/SHINE and the results of G4BL simulations.

Chapter 6

Instrumentation Studies

Delivering a beam to NA61/SHINE, while important, is not the only objective that must be achieved, as all of the delivered particles must be tagged and identified to be used in later analyses. To this end, extensive studies have been performed to create a scheme which will enable particle-by-particle identification, and this, along with the effects of the instrumentation on the beam's figures of merit, will be discussed in depth in this chapter.

6.1 Particle Identification Requirements

In all of NA61/SHINE's future analyses, knowing which particle species is causing an interaction in their target will be of great importance. Therefore, a new scheme for particle identification has been developed during this DPhil, to enable particle-by-particle tagging of all relevant particle species throughout the low-energy beamline's momentum range, from as low as 2 GeV/c to 13 GeV/c.

In this section, a brief overview of the proposed particle identification scheme is given, followed by an in-depth description of the detector technologies involved.

6.1.1 Overview of the Particle Identification

The specific range of momenta at which the beamline will operate has proven to be particularly challenging, as two different types of technologies will need to be used to ensure full particle identification. Specifically, the lower end of the momentum range can be addressed using a time of flight (ToF) system, while for the upper end, a system of threshold Cherenkov counters can be used. The intermediate energies will be addressed by the use of a combination of the two systems, which has been designed specifically to address the requirements of NA61/SHINE while also minimising the material budget in the beamline, as this otherwise could cause a significant emittance growth and a larger beam-spot size, as discussed in Section 2.7.

6.1.2 Time of Flight

A time of flight system works by taking advantage of the fact that particles of different masses, when travelling with the same momentum, have different velocities. So, by measuring the time taken to travel between two triggers separated by a known distance d, it is possible to identify a particle.

This time difference in terms of the two particle's masses can be calculated using some simple relativistic formulae, namely,

$$\begin{aligned} \Delta t &= d \cdot \Big(\frac{1}{v_1} - \frac{1}{v_2}\Big) \\ \Delta t &= \frac{d}{c} \cdot \Big(\frac{E_1}{p_1 c} - \frac{E_2}{p_2 c}\Big) \\ \Delta t &= \frac{d}{c} \cdot \left(\sqrt{1 + (\frac{m_1 c^2}{pc})^2} - \sqrt{1 + (\frac{m_2 c^2}{pc})^2}\right) \end{aligned} \tag{6.1}$$

where m_i is the rest mass of the i-th particle and p is the nominal momentum of the beam, assumed to be the same for both particles in the third step. A pair of particles are said to be resolvable if the time difference in their arrival Δt is greater than the resolution of the ToF, σ_{ToF}. Generally, to account for different paths particle take and the momentum acceptance of the line a multiple of σ_{ToF} is used to consider the particles resolved. Throughout these studies, particles have been defined as resolved if $\Delta t > 4\sigma_{ToF}$.

It is possible to plot the difference in travel time of several particle pairs at different momenta, to assess whether such a pair would be resolvable. This is shown in *Figure* 6.1. As can be seen from the plot, as the energy increases and the particles become more relativistic, the ability of the ToF to separate particle pairs decreases. Additionally, a ToF works best if the difference in mass of the particles is large, for example, it is rather straightforward to separate a proton from a pion due to the very different masses, while it is extremely difficult to separate a pion and an electron.

From these plots, it is clear that a ToF can be used to resolve particles as long as they are in the low end of the momentum range, where particles can be separated by an amount greater than 4-σ. However, a different technology must be used to separate

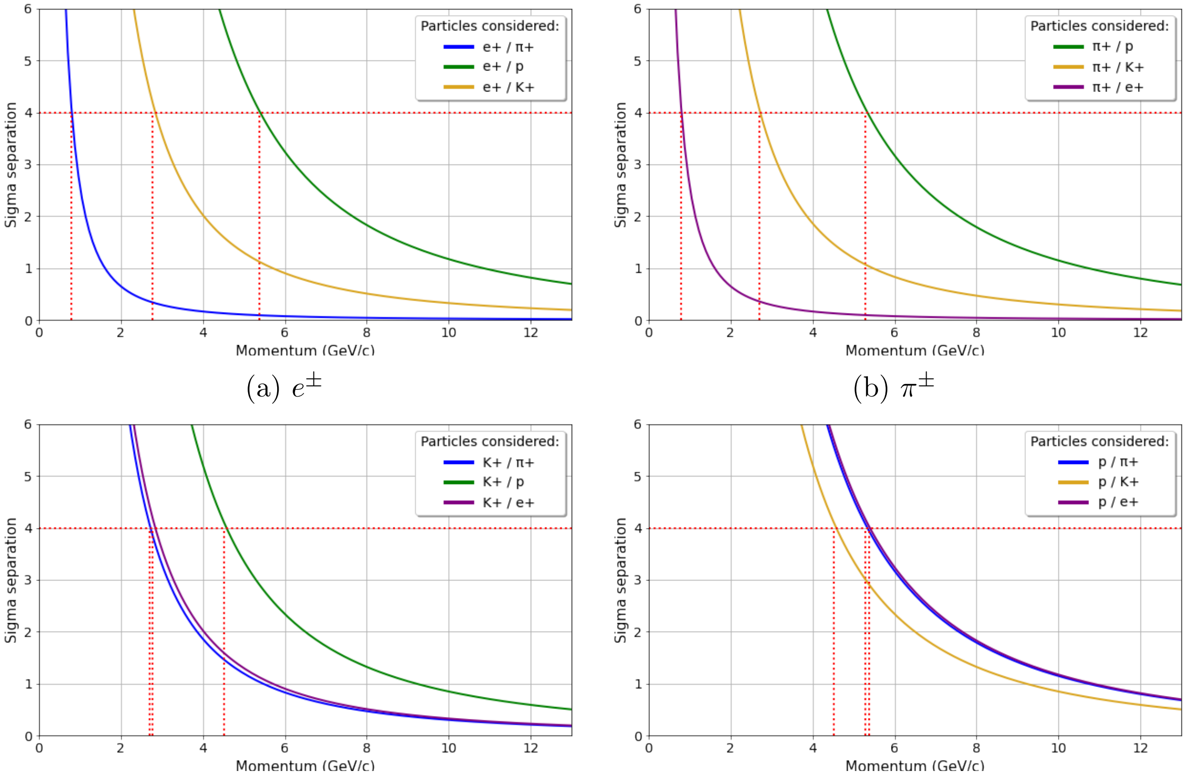

(a) $e^{\pm}$ (b) $\pi^{\pm}$

(c) $K^{\pm}$ (d) Proton

Figure 6.1: The separation in terms of arrival times of (a) electrons (b) pions (c) kaons and (d) protons with respect to other particles as a function of momentum. The red lines indicate the momenta at which particle pairs have a 4 sigma separation. At momenta lower than this the relevant pair is resolvable. The y-axis is scaled to be in terms of the number of σ_{ToF}, equal to 500 ps in this specific example.

particles in the travelling with momenta above a few GeV/c.

6.1.3 Threshold Cherenkov Counters

Threshold Cherenkov counters are used for the identification of relativistic charged particles by detecting and amplifying photons which are produced via the Cherenkov effect. A particle travelling in a medium may travel with a velocity v greater than the speed of light in the medium, given by c/n. When this takes place, Cherenkov light is emitted with an opening angle given by

$$\cos(\theta) = \frac{c}{n\beta}. \tag{6.2}$$

It is useful to relate the refractive index of a gas to its pressure. This can be done using the Lorentz-Lorenz equation [51, 83], and leads to the relationship

$$n \approx \sqrt{1 + \frac{3AP}{RT}} \approx 1 + \frac{3AP}{2RT} \tag{6.3}$$

where A is the molar refractivity, P is the gas pressure, R is the universal gas constant, and T is the absolute temperature. The Taylor expansion to first order in the last step follows as in gases, in general, the refractive index can be written as $n \approx 1 + \delta$ where $\delta << 1$.

The refractive index at the standard 1 atm pressure and 20 °C room temperature, n_{20}, can be measured, and from this a general refractive index can be calculated as a function of the gas pressure at room temperature P_1 and the room temperature itself T_{20}, leading to

$$\begin{aligned} n_{20} &= 1 + \frac{3AP_1}{2RT_{20}} \\ n(P) &= 1 + \frac{3AP}{2RT_{20}} \\ n(P) &= 1 + \frac{P}{P_1}(n_{20} - 1) \\ n(P) &= 1 + P(n_{20} - 1) \end{aligned} \tag{6.4}$$

where the last step follows as $P_1 = 1$ atm. By combining this last equation with Equation 6.2, one arrives at

$$P_{th} = \frac{m^2}{p^2} \cdot \frac{1}{2(n_{20} - 1)}, \tag{6.5}$$

the threshold pressure in a gas at which a particle of mass m and momentum p begins emitting Cherenkov photons. Several values for n_{20} are readily available in the literature [41].

The threshold pressures for CO_2 and He can be seen in *Figure* 6.2. Here, the solid, horizontal, red line represents the maximum pressure achievable with the standard Cherenkov counters used at CERN, whereas the dashed, horizontal, red line represents the minimum pressure, these are 15 and 0.5 bar respectively. Particles can emit photons as long as the pressure is greater than the threshold pressure at a certain momentum, given as the coloured lines.

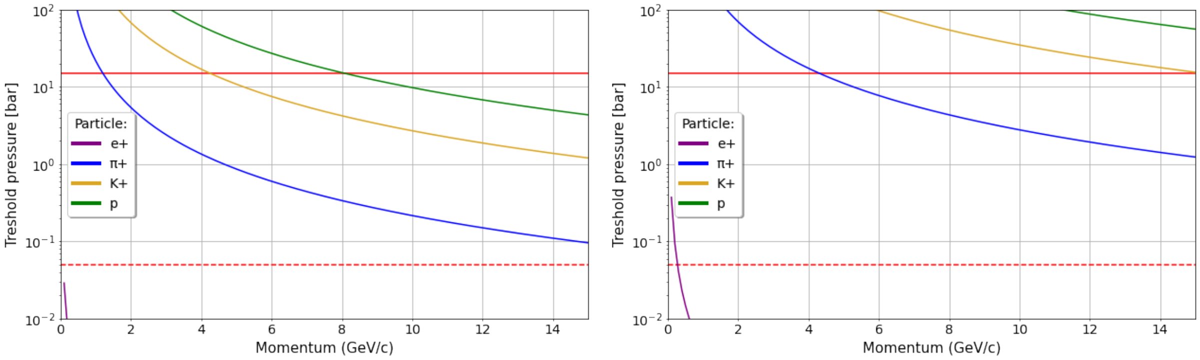

(a) Carbon dioxide in Cherenkov counter.

(b) Helium in Cherenkov counter.

Figure 6.2: The threshold pressure for several particles with momenta ranging from 0 to 15 GeV/c in (a) carbon dioxide and (b) helium.

Producing a single photon however would not be sufficient to tag a particle with sufficient certainty. Therefore, it is useful to be able to estimate the number of photons a particle will produce. This can be done using the formula [84]

$$N_\gamma = AL\theta^2. \tag{6.6}$$

Here A is a numerical constant which can be empirically measured, while L is the length of gas through which the particle travelled. Using this equation, alongside Equation 6.2 and Equation 6.5, one can arrive at the expected number photons as a function of pressure,

$$N_\gamma = 2AL(n-1)(P-P_{th}). \tag{6.7}$$

Assuming a Poissonian distribution, a minimum number of 5 photo-electrons is necessary to obtain over 99% certainty of particle tagging, hence, the production of 5 photons was chosen to be the minimum for a particle to be considered detected in the low-energy beamline's instrumentation scheme. The dependence of the number of photons produced at the maximum pressure achievable of 15 bar on the beam's momentum can be seen in *Figure* 6.3. As can be seen, the threshold momenta for identifying particles are only slightly higher than those needed to produce a single photon.

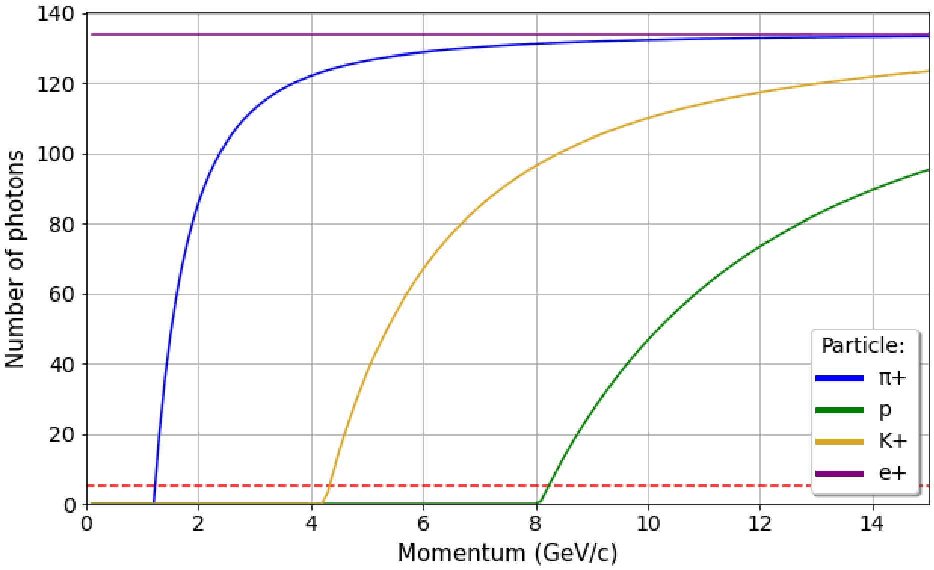

Figure 6.3: The number of γ produced as a function of beam momentum in CO_2 at 15 bar. The red line indicates the 5 γ necessary for particle identification.

As can be seen from the above plots, threshold Cherenkov counters are capable of tagging particles in the medium to high momentum ranges of the low-energy beamline. In the upcoming section, the way in which ToF and the Cherenkov counters can be combined to fully tag particles will be outlined

6.2 Overall PID Scheme

In this section, the overall particle identification scheme will be introduced, specifying the available distances for the ToF detectors, the gases available, and the expected performance of the future instrumentation for NA61/SHINE.

6.2.1 Capabilities of the Instrumentation Used

The minimum instrumentation necessary for complete particle identification over all momentum ranges will be: one ToF system, three threshold Cherenkov counters, and one scintillating detector, with the possibility of using either one of NA61/SHINE's counters or the second ToF detector for this, to minimise material budget.

In general, the idea is that at low energies, the ToF system will be sufficient for PID. As the nominal momentum of the beam is increased and the time difference between arrival of particles is decreased, the Cherenkov counters will be activated to individually tag particles. Eventually, the ToF system will no longer be used, and particles will be exclusively tagged via the Cherenkov counters.

By considering a 40 metre long distance between the ToF plates and a 500 ps resolution, the target resolution NA61/SHINE is aiming to achieve for the ToF [85], one obtains the particle timing separation curves already shown in *Figure* 6.1. It is possible to plot the maximum momenta at which particle pairs are resolvable as a function of momentum, and this is done in *Figure* 6.4a.

On the other hand, a 2 m long Cherenkov counter, filled with CO_2 gas at a pressure of 15 bar can scintillate at the momenta shown in *Figure* 6.4b, as differently coloured regions for each particle species. These Cherenkov counters are what is currently used at CERN, with the gases having been chosen such that there would be no health and safety overhead, as would have been the case had a gas like Freon been used.

Figure 6.4c shows the combined coverage of the ToF system and the Cherenkov counters at maximum pressure. The gaps are regions where neither detector system can directly identify the particles.

However, by using these together, it is possible to cover a larger range of momenta. An example of this is shown in *Figure* 6.5, where two groups of particles resolvable by ToF can be seen. The first of these is made up exclusively of protons, whereas the second group is made up of kaons, pions, and positrons, not resolvable with a ToF system exclusively. If, in this example we assume that only the pions and positrons are able to emit photons in a threshold Cherenkov counter, not all species can be identified using a type of instrumentation exclusively, but by combining the two, it is possible to obtain the number of all desired particles. This can be done by obtaining the number of protons from the ToF, n_p, and then using two Cherenkov counters to obtain n_π and n_e, the number of pions and positrons respectively. By using the total number of charged particles, n_{tot} obtained from a scintillator, it is then trivial to obtain the number of kaons, n_k, as $n_k = n_{tot} - (n_p + n_\pi + n_e)$. In this case, even though only three particles were detectable with each type of instrumentation, *all* particle species were resolvable. The combined effect of the instrumentation is shown in *Figure* 6.4d as the additional shaded region.

6.2.2 Designing the Identification Scheme

Figure 6.4d shows that by using several Threshold Cherenkov counters filled with CO_2 at a maximum pressure of 15 bars, combined with a 40 m long ToF with a 500 ps resolution, it is theoretically possible to identify and tag all relevant particle species in the low-energy beamline. However, this does not yet present a usable scheme for tagging particles at various momenta.

In such a scheme, pressures and gases in the Cherenkov counters must be selected such that one is able to calculate the number of particles of each species, while also attempting to minimise the material budget within the beamline, as this may otherwise have adverse effects on the emittance of the beam, as described in Section 2.7. The minimum number of Cherenkov counters to achieve this is three, such that at high momenta the first counter can tag all the positrons, the second is used to tag the pions, the third the kaons, and the number of protons is obtained by subtracting these particles from the total number of charged particles measured in one of the triggers or the second ToF. The muons can simply be vetoed by NA61/SHINE's detectors, as discussed in Chapter 1.

The pressure at which the Cherenkov counters can be run to identify particles can be seen in *Figure* 6.6. In these plots, error bands have been added for $\Delta p/p = \pm 10\%$ and $\pm 20\%$. This has been done as the low-energy beam will not be monochromatic, and so, by considering the combination of off-momentum particles and the uncertainty in the gas pressure measurement, it could have been possible for the wrong particles to be tagged.

As can be seen from these figures, it is generally possible to find pressures of carbon dioxide where each particle can be well identified. This is done by setting the Cherenkov counter's pressure higher than the particle that one wants to identify and lower than the next one in terms of mass. For example, at 6 GeV/c, one can imagine setting the first counter at 1.0 ± 0.1 bar, to detect all positrons with ±10% $\Delta p/p$, the second at 2.0 ± 0.1 bar, to detect pions and positrons, and the third counter at 10.0 ± 0.1 bar to tag kaons, pions and positrons. To obtain the number of individual particles, one can then take the number of hits in their counter and subtract the number of other particles obtained from the preceding one.

Difficulties arise in the separation of pions and positrons above 7 GeV/c due to the similar masses of these particles and the limited precision with which Cherenkov counters can be filled. Therefore, beyond these energies, the relevant Cherenkov counters will be filled with helium gas. The minimum pressures at which helium produces photons can be seen in *Figure* 6.6b. As helium gas is less effective at producing photons, pions and electrons scintillate at distinct threshold pressures, and so a pressure at which one species produces photons while the other does not can be found.

Putting together these insights and tabulating the results, one arrives at the complete instrumentation scheme shown in *Table* 6.1.

Momentum (GeV/c)	Detector	Gas and pressure	Particle Identified
2	Time of flight	-	π^+, k^+, p
	Thr. Cherenkov Counter 1	CO_2 at 8 bar	e^+
	Thr. Cherenkov Counter 2	-	
	Thr. Cherenkov Counter 3	-	
	Scintillator	-	
4	Time of flight	-	p
	Thr. Cherenkov Counter 1	CO_2 at 1.1 bar	e^+
	Thr. Cherenkov Counter 2	CO_2 at 2.3 bar	π^+
	Thr. Cherenkov Counter 3	-	
	Scintillator	-	k^+
6	Time of flight	-	
	Thr. Cherenkov Counter 1	He at 8.0 bar	e^+
	Thr. Cherenkov Counter 2	CO_2 at 2.5 bar	π^+
	Thr. Cherenkov Counter 3	CO_2 at 10 bar	k^+
	Scintillator	-	p
8	Time of flight	-	
	Thr. Cherenkov Counter 1	He at 8.0 bar	e^+
	Thr. Cherenkov Counter 2	CO_2 at 1.5 bar	π^+
	Thr. Cherenkov Counter 3	CO_2 at 6 bar	k^+
	Scintillator	-	p
10	Time of flight	-	
	Thr. Cherenkov Counter 1	He at 8.0 bar	e^+
	Thr. Cherenkov Counter 2	CO_2 at 1.3 bar	π^+
	Thr. Cherenkov Counter 3	CO_2 at 4 bar	k^+
	Scintillator	-	p
13	Time of flight	-	
	Thr. Cherenkov Counter 1	He at 8 bar	e^+
	Thr. Cherenkov Counter 2	CO_2 at 1.2 bar	π^+
	Thr. Cherenkov Counter 3	CO_2 at 3 bar	k^+
	Scintillator	-	p

Table 6.1: The instrumentation scheme to identify particles in each relevant momentum range. In this table, identification means implies a $>$ 99% detection efficiency. For all pressures an uncertainty of ±0.1 bar can be assumed to arise from the gas supply [86].

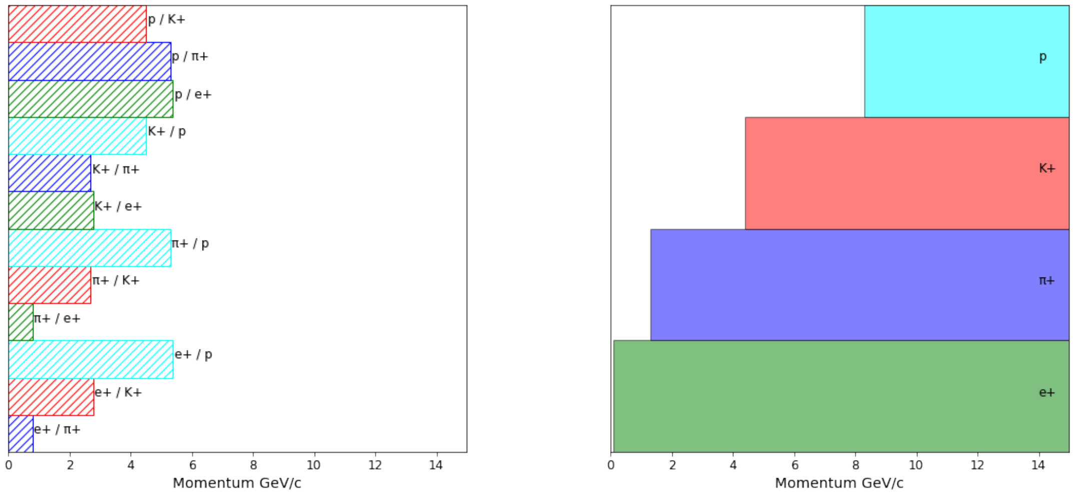

(a) Momentum range over which particles can be separated by ToF.

(b) Momentum range over which particles can be detected by Cherenkov counters.

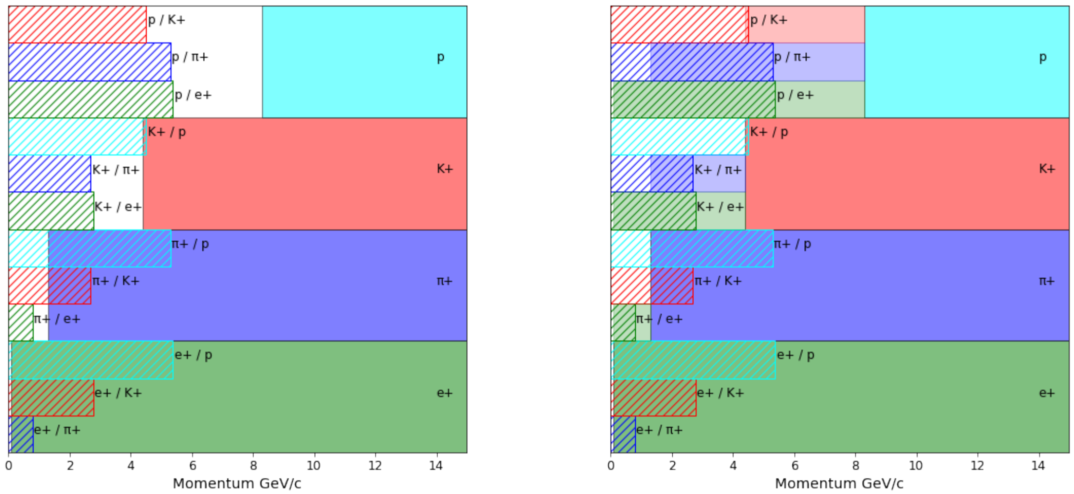

(c) Momentum range over which particles can be tagged by the ToF and Cherenkov counters if these are used individually.

(d) Momentum range over which particles can be tagged by the combined ToF and Cherenkov counters if these are used together.

Figure 6.4: The momenta at which particles can be tagged by the instrumentation in the the low-energy beamline. The particles have been plotted vertically in order of increasing mass. The momentum region in which pairs of particles can be resolved by the ToF is shown by hatched regions, whereas the regions in which each particle species emits photons is represented by solid colours, with the particle name shown on the right. Areas in which certain particles can only be detected by the combined use of the ToF and Cherenkov counters are represented by lightly shaded regions.

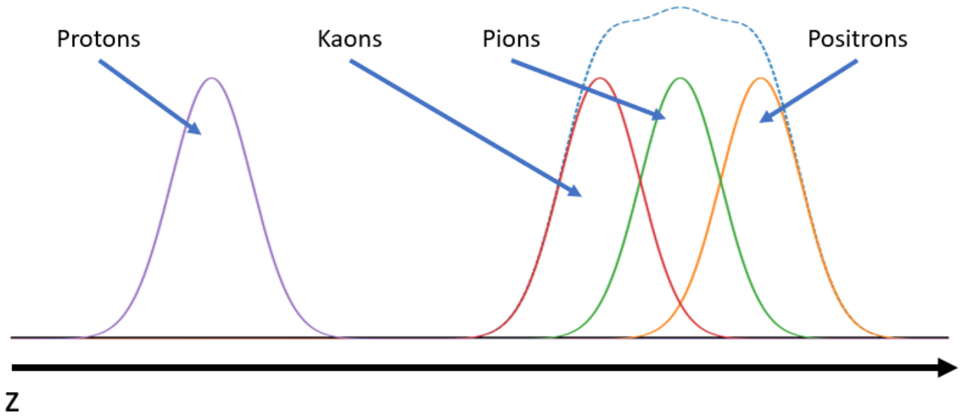

Figure 6.5: A situation in which only the protons are resolvable by ToF, whereas the three other particles are seen as a single signal by the ToF (seen as a dashed line). If only the positrons and pions emit photons in two separate Cherenkov counters, all four particle species will be resolvable.

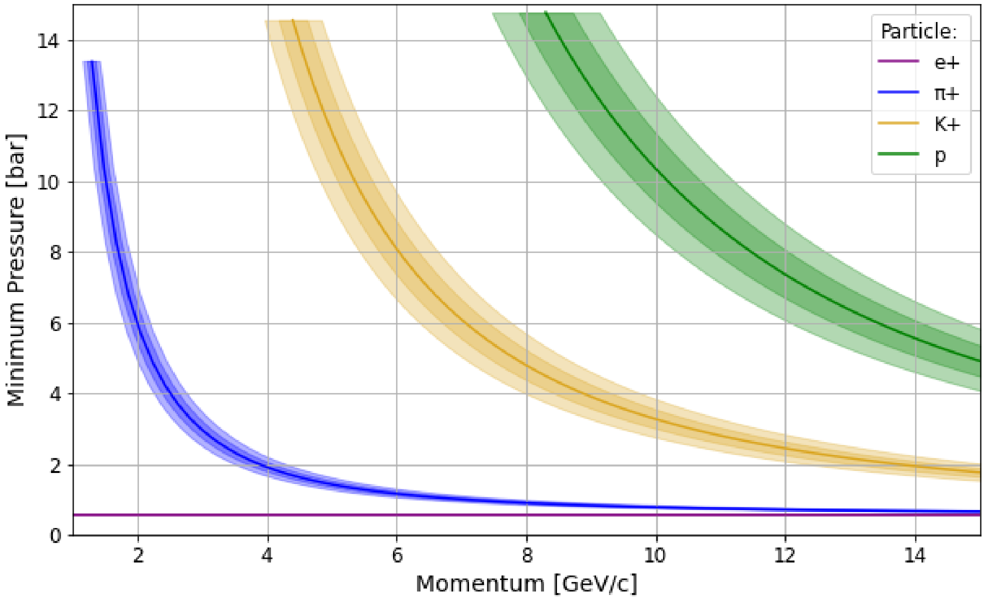

(a) Carbon dioxide.

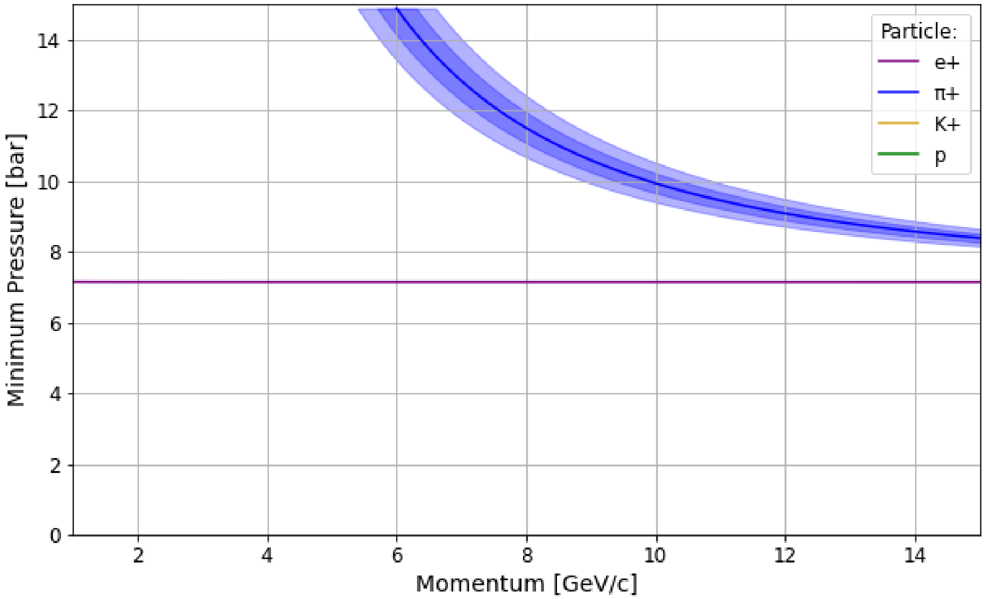

(b) Helium.

Figure 6.6: The threshold pressure in a 2 m long Cherenkov counter filled with (a) CO_2 and (b) He at different momenta for several particles. Bands have been added to consider the effect of particles with momentum spread $\Delta p/p = \pm 10\%$ and $\pm 20\%$.

6.2.3 Placing the Instrumentation

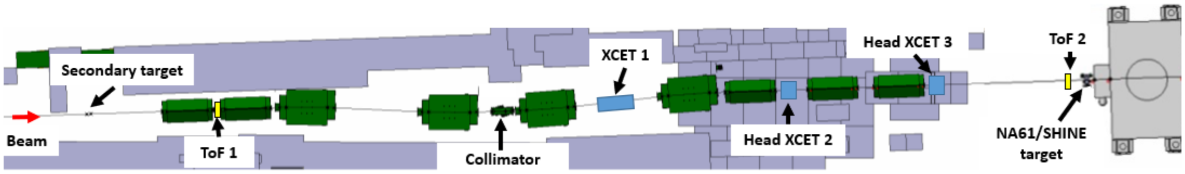

Figure 6.7: The location of the two time of flight detectors and the three threshold Cherenkov counters (XCET).

The location of all pieces of instrumentation for the low-energy beamline can be seen in *Figure* 6.7. As the scintillating plates need to be as far as possible from one another, the first is placed between quadrupole 1 and quadrupole 2 of the beamline, while the second is placed just before NA61/SHINE's target. This gives a total distance for the particles to travel of just over 40 metres. The first detector is not placed before quadrupole 1 to attempt to shield it from some of the secondary showers and to ensure mainly relevant particles are detected.

The three Cherenkov counters on the other hand are all placed after the momentum selection of the low-energy beamline. This was done to ensure an accurate count of the secondary particles, only tagging those which both have the correct momentum, and are likely to arrive at the NA61/SHINE detector. The first Cherenkov counter will be placed between dipole 3 and dipole 4, with its 2 metre long tube comfortably occupying the over 4 metre long drift. On the other hand, the tubes that will contain the gas of counter 2 and counter 3 will be placed inside quadrupole 3 and quadrupole 5, to minimise the space occupied, while the head of the detectors will be just outside of the magnets.

6.3 Effects of Instrumentation on Beam Properties

To simulate the effects of the instrumentation on particle rates and beam-spot size, G4BL simulations were run at different energies using the instrumentation described in *Table* 6.1. The instrumentation was changed in each run to include the relevant Cherenkov counters, be it the high or low-pressure devices, and gas pressures, including accounting for thicker beam windows in case the pressure required exceeded the 5 bar limit of the low-pressure Cherenkov detectors used at CERN. In these simulations 10^6 primary 400 GeV/c protons were simulated, and included particle cuts for particles with energies below 0.5 MeV/c.

The ToF detectors were simulated as two 5 mm long, 200-by-200 mm blocks of scintillator, whereas the Threshold Cherenkov counters were simulated as columns of gas in the path of the beam at the correct location, with beam windows before and after. The specific gas and density was varied depending on the beam's nominal momentum according to the values given in *Table* 6.1. Finally, some of the instrumentation which will be used by NA61/SHINE was also included, namely the BPD monitors the experiment is currently developing and intending to use in future runs. These are three silicon detectors 0.6 mm thick and with a height and width of 200 mm.

The effect of the instrumentation has been considered at the end of the beamline, by assessing the effects on the particles impinging on the NA61/SHINE target. To better contextualise the results with the material that has been added to the beamline, *Table* 6.2 presents the various instrumentation configurations and the percentage of radiation length, X_0, which the instrumentation adds.

6.3.1 Effect on Particle Rates

Any material placed in the beam and the subsequent emittance growth caused by this must be carefully monitored in a low-energy beamline, to ensure that the particle rates are still satisfactory when any additional potential losses are considered. To this end, *Figure* 6.8, shows the particle rates without the instrumentation and with the addition of the instrumentation, when the collimator jaws are opened to 20 mm.

As is clear in the figure, the addition of the instrumentation has a small but consistent effect over the beamline's momentum range on the particle rates which can be expected to reach the NA61/SHINE experiment.

While one may expect these losses to be more significant in the low-momentum regime of the beamline, they appear to be small at 2 GeV/c and relatively constant at momenta of 4 GeV/c and beyond. This happens because below 4 GeV/c, a ToF with a very

Momentum (GeV/c)	Detector	X_0 from Detector (%)	Total X_0 (%)
2	Time of flight	3.3	6.8
	Thr. Cherenkov Counter 1	1.8	
	Thr. Cherenkov Counter 2	0	
	Thr. Cherenkov Counter 3	0	
	Scintillator	1.7	
4	Time of flight	3.3	11.7
	Thr. Cherenkov Counter 1	1.8	
	Thr. Cherenkov Counter 2	1.8	
	Thr. Cherenkov Counter 3	3.1	
	Scintillator	1.7	
6	Time of flight	3.3	13.1
	Thr. Cherenkov Counter 1	3.1	
	Thr. Cherenkov Counter 2	1.8	
	Thr. Cherenkov Counter 3	3.1	
	Scintillator	1.7	
8	Time of flight	3.3	13.1
	Thr. Cherenkov Counter 1	3.1	
	Thr. Cherenkov Counter 2	1.8	
	Thr. Cherenkov Counter 3	3.1	
	Scintillator	1.7	
10	Time of flight	3.3	13.1
	Thr. Cherenkov Counter 1	3.1	
	Thr. Cherenkov Counter 2	1.8	
	Thr. Cherenkov Counter 3	3.1	
	Scintillator	1.7	
13	Time of flight	3.3	13.1
	Thr. Cherenkov Counter 1	3.1	
	Thr. Cherenkov Counter 2	1.8	
	Thr. Cherenkov Counter 3	3.1	
	Scintillator	1.7	

Table 6.2: The percentage of a radiation length each component of the instrumentation scheme contributes to. The contribution from the Cherenkov counters is dominated by the aluminium windows, changed in each configuration depending on the pressure used. Not included in the table are the BPDs, and the scintillators used by NA61/SHINE, as these are not part of the instrumentation scheme.

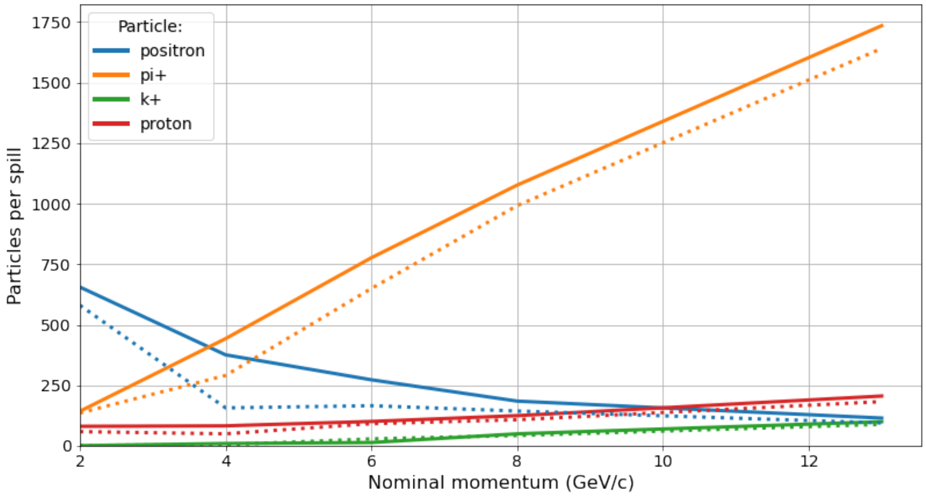

Figure 6.8: The effect of instrumentation on the number of particles reaching the NA61/SHINE target as the nominal momentum is varied and with collimator jaws set to ±10 mm, with a spill size of 10^6 400 GeV/c protons. The solid lines depict the particle rates without instrumentation, whereas the dashed lines show the number of particles when instrumentation is present.

small material budget is sufficient for particle identification, whereas at momenta above 4 GeV/c, one must start to rely on using the Threshold Cherenkov counters. This nearly doubles the amount of material in the beam, in terms of X_0, mostly due to the beam windows.

While there are statistically significant drops in the particle rates, the numbers obtained in these simulations are still well within the acceptable rates for the experiment.

6.3.2 Effect on Beam-Spot Size

The beam-spot size at the NA61/SHINE target is also expected to grow due to the instrumentation's material in the beam, and it is important to ensure that this too is within the requirements of the experiment. Using the simulations discussed earlier, it has been possible to obtain values of the new beam-spot size at different momenta in the 2 to 13 GeV/c range, which were then compared to those obtained without the instrumentation present. These effects can be seen in *Figure* 6.9, where the beam-spot sizes with and without instrumentation in the horizontal and vertical planes can be compared. As expected, the most significant growth takes place in the lowest momenta, especially at 4 GeV/c, where the high-pressure Threshold Cherenkov Counters and the thicker aluminium windows had to be placed.

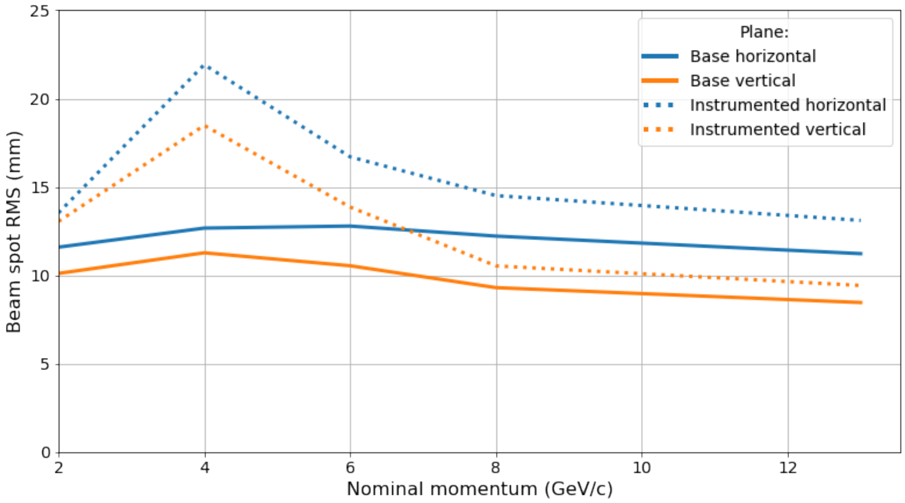

Figure 6.9: Comparison of the beam-spot size in the horizontal and vertical planes with instrumentation present (dotted lines) and without instrumentation (solid lines) over the beamline's range of operational momenta.

While the sizes of the beam have increased at all energies, they are generally below the 20 mm RMS limit imposed by NA61/SHINE. For NA61/SHINE's most important physics cases, at 2 and 13 GeV/c, the beam is within the limits, whereas, issues only arise at 4 GeV/c a momentum of secondary importance. These in general are unlikely to cause difficulties for the experiment's datataking. Additionally, in the future, it may be possible to lower the pressure of the Threshold Cherenkov Counters by using a higher resolution ToF detector. If this becomes a reality, it may be achievable to have a sub 20 mm RMS beam-spot size at all nominal energies.

Chapter 7

Implementation of the Beamline in CERN's North Area

After having studied the low-energy beamline's targets, optics and design, and instrumentation, the next key milestone was the development of plans and procedures for the implementation of this line into the North Area. This chapter describes this process and all the steps necessary to go from a theoretical design to a finalised, ready to be installed, beamline. Specifically, this chapter describes how the beamline could be installed into H2 without losing the current capabilities of the line at 400 GeV/c, considerations on the powering of the magnets, and studies on the radiation footprint the beamline will have in the North Area, including possible changes to the shielding currently present in EHN1 the beamline may require.

7.1 Placing the Beamline in CERN's EHN1

The first step in realising this new beamline into the North Area was to integrate it with the currently existing H2 line. This had to be done carefully to ensure that all magnets could be installed without issues and that the high-energy capabilities of H2 would be maintained. This section explores the modifications to the H2 line which will be necessary for the low-energy beamline to be installed, the scheme for switching between configurations, and finally, the new optics that have been calculated for the H2 beamline to ensure comparable behaviour to what can be currently achieved.

7.1.1 Combining H2 and H2-VLE

At CERN, the main program currently used to generate coordinates of beam line elements using the CERN global coordinate system is BEATCH [87]. The software is essential for the correct installation and alignment of elements for all of the machines present at CERN. BEATCH models of the H2 line have existed for many years, and a key step in advancing the low-energy beamline was to create a BEATCH file which combined the new beamline with H2.

A graphical representation of the BEATCH file of the current H2 beamline can be seen in *Figure* 7.1a, while how the beamline will look during low-energy operation can be seen in *Figure* 7.1b. The magnets in these figures follow the naming convention adopted at CERN of “magnet code" followed by “X.", then the “beamline code" and finally the “s-position". For example, a QPL magnet placed at s=123 for the H2 line would have the code QPL.X021123. Quadrupole and dipole magnets are shown in blue and green respectively. As can be seen from the figure, the H2 line is unchanged up to element QNL.X021479, while afterwards all elements will be removed and replaced by those of the low energy line.

The figure also contains other elements of secondary importance in the overall installation of the beamline, such as the MDXV and MDXH vertical and horizontal trim magnets, the XCON target and the XCSH horizontal collimator, used for momentum selection. The MDXV and MDXH trim magnets have been moved upstream to enable the steering of the beam in both low and high-energy operation and to ensure that there is no loss in phase space acceptance. Additionally, sufficient space for any additional beam position measurement instrumentation has been left in both H2-2024 and H2-VLE configurations, for example in the space before MBPL X021516 or after QPL X021527.

7.1.2 Ensuring Continued High-Energy Operation

The configuration shown in *Figure* 7.1b is suitable for transporting particles with momenta up to 13 GeV/c, as per NA61/SHINE's requirements, however, it is also important that the H2 beamline can continue to transport other particles at high energies for the continuation of the other branches of NA61/SHINE's physics programme.

Due to time constraints, it would be impossible to change between low-energy operation and standard operation by removing and replacing the magnets used in the two cases, as this would take approximately two weeks to perform [88], which would cause significant problems in terms of beam scheduling. Because of this, a solution where the

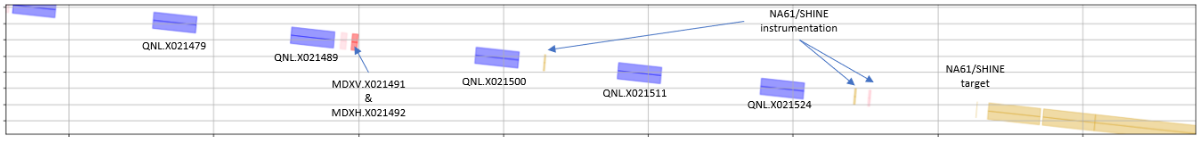

(a) The H2 beamline

(b) The H2-VLE beamline in H2

(c) The H2-2024 beamline

Figure 7.1: The position of beamline elements in the CERN coordinate system.

low-energy beamline and a modified version of H2, called H2-2024, coexist and are available at almost the same time has been envisioned. To achieve this, a rail system will be used. Specifically, two of the low-energy beamline's quadrupoles and two dipoles will be movable in and out of the beam. This will be done so that the large aperture QPL magnets used in the low-energy beamline can be replaced by the high gradient QNL quadrupoles used in H2 and the dipoles can be moved out of the path of the 400 GeV/c beam. For high energy operation, not only will the two QPL magnets be replaced by two QNL magnets, but a third QNL magnet will be placed between the first MBPL magnet and the second, also on rails. The first and last dipoles in the low-energy beamline will not need to be moved out of the beam during high energy operation as these dipoles can simply be switched off when not needed. Additionally, the other QPL magnets can stay in place, as due to their large apertures, if switched off they will not affect the acceptance and performance of the H2-2024 beamline.

The two BEATCH outputs for the H2-VLE line and the H2-2024 line can be seen and compared in *Figures* 7.1b and 7.1c. For the rail system to be used, the position of the QNL magnets had to be fixed to be identical to those of the QPL magnets they will replace, so that these could be installed on one shared rail system, decreasing costs.

While the graphical output of the BEATCH files can be useful for understanding exactly how all the magnets will be placed, a CAD drawing[1] of the current H2 line alongside H2-VLE and H2-2024 can help visualise better the position of the magnets and the switching scheme. These images can be seen in *Figure* 7.2. The colours of the quadrupoles of the H2-VLE line and H2-2024 line represent whether or not they will stay in place. Elements in green correspond to the H2-VLE line and some will be moved out of the beam, quadrupole magnets in blue stay fixed when changing mode, and those in red are only present in the H2-2024 configuration.

7.1.3 New H2-2024 Optics

Having a system to change between low-energy operation and high-energy operation is of great importance to NA61/SHINE, however simply being able to place magnets suitable for transporting a high-energy beam is not sufficient, one must also show that new optics exist which perform in a comparable way to those previously used. To this end, the H2-2024 beamline configuration has been extensively tested to ensure that the beam quality delivered to NA61/SHINE and other downstream experiments is similar to what can currently be achieved for 450 GeV/c beams, for ions, and other downstream experiments, all this while also respecting the constraints currently placed on the beamline. Some of these are, for example, magnets which share a power supply and therefore must maintain identical currents, magnets which cannot be used due to instrumentation, such as beam position detectors used for track reconstruction, and maximum magnet currents and fields.

These new optics can be found in Appendix D. These optics show that with the three new QNL quadrupoles, in addition to the already present quadrupoles in H2, it is possible to calculate equivalent optics which bring the beam into focus at the same positions as can be currently achieved, with no loss of performance, for all previously utilised configurations of H2.

---

[1] Many thanks to S. Girod and V. Clerc for the help in generating these images.

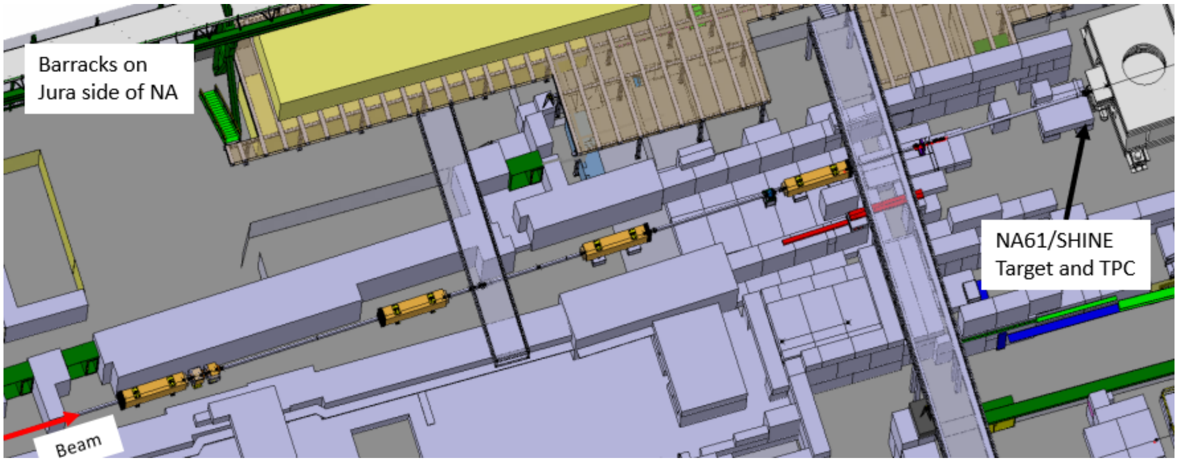

(a) The H2 beamline.

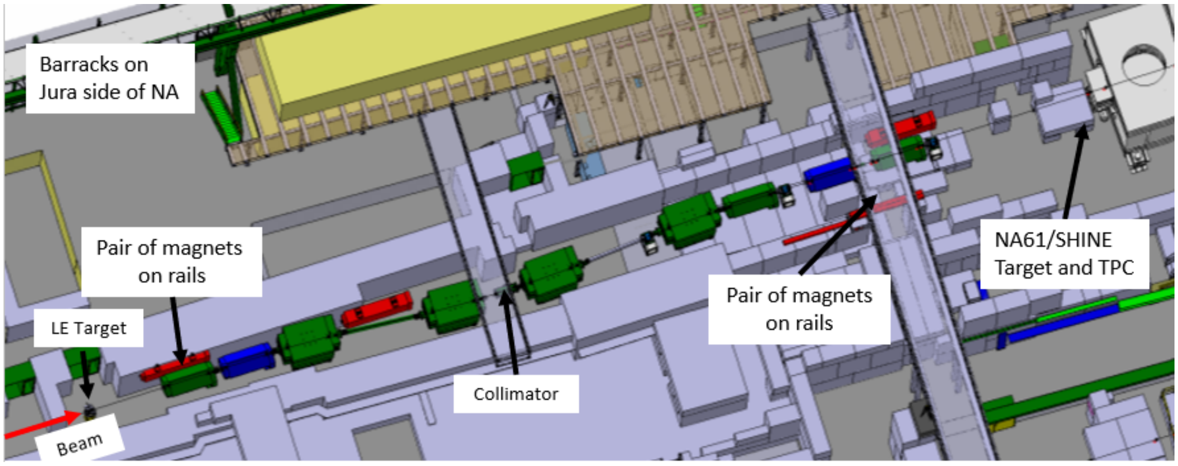

(b) The H2-VLE beamline in H2.

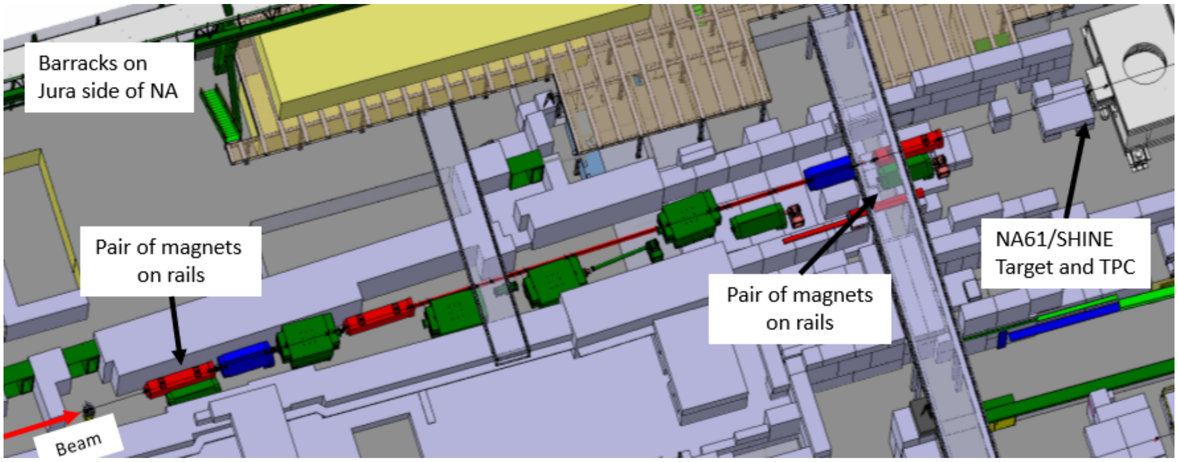

(c) The H2-2024 beamline.

Figure 7.2: CAD representations of beamline elements in the CERN North Area.

7.2 Power Supplies

The powering of the dipole and quadrupole magnets is not a trivial issue, as the availability of power supplies is not guaranteed and the cabling from these to the magnets can be a significant cost, as the price of cables is a fixed per metre quantity, giving another incentive for optimising the selection of the power supplies. This section provides an overview of the power supplies currently used at CERN, specifically in the North Area, and describes a scheme for powering the magnets in the low-energy beamline and H2-2024 using currently available power supplies.

7.2.1 Overview of the Power Supplies at CERN

In CERN's EHN1 many different types of power supplies and related electronics are available. A summary of these and their specifications is given in *Table* 7.1 [89]. As can be seen from this table, the first letter of the name gives information on the type of element type: elements starting with the letter R are rectifiers, which act as power converters, while those starting with a D are diode modules which can be mounted in series with a power converter to increase the output voltage. Finally, available at CERN but not present on this list are power converters for superconducting magnets, denoted by the letter S. These have been excluded from this discussion as superconducting magnets are not used in the low-energy beamline.

To be able to identify a specific power supply two additional pieces of information are added. A letter is prepended to the element type to represent in which of CERN's experimental areas it is used while its 3 digit ID is added to the end of this name, giving a unique identifier for each power supply. For example, in the North area, a 1000 A rectifier with the ID of 12 would be called NR21-012.

7.2.2 The Power Supplies for the Low-Energy Beamline and H2-2024

The magnets relevant to the proposed low-energy beamline and their power supplies (PS) can be seen in *Figure* 7.3. As discussed in section 7.1, the magnets and instrumentation up

Element type	Name	Max current (A)	Voltage (V)
Diode	D21	1500	200
Diode	D31	2500	285
Rectifier	R11	500	125
Rectifier	R12	500	300
Rectifier	R13	500	225
Rectifier	R21	1000	300
Rectifier	R22	1500	250
Rectifier	R31	2500	355

Table 7.1: A summary of the different types of power supplies and related electronics available for use in the H2 line in EHN1.

to Q16 will remain unchanged, meaning that any power supply used in these magnets must remain unaffected by the low-energy beamline. Between Q16 and the vertex magnets, used by the NA61/SHINE detector, however, the current H2 line will be significantly modified, meaning that all the power supplies used here can be used for the new low-energy beamline and for H2-2024. Additionally, all power supplies beyond Q21 are also available for use in the low-energy beamline. These were used in the optics used for various test beams, which will not take place in conjunction with the low-energy beamline, as such all these power supplies can be used to power the new beamline without causing any conflicts.

In *Figure* 7.3 it is important to note how the power supplies and diode modules are used for powering magnets, specifically how these are used for dipole magnets. Here, a rectifier module is connected to a diode module to provide sufficient current to power 2 dipoles simultaneously. This not only lowers the overall number of power supplies needed, but can also prove to be useful to ensure that the beam is centred on the NA61/SHINE target. If, for some reason, such as a misalignment in the upstream magnets, the beam is found to not be centred at the NA61/SHINE target, it will be possible to correct this effect by modifying the currents in two of the four dipoles.

By rearranging the PS shown in *Figure* 7.3, it has been possible to produce a scheme to power all necessary magnets in the low-energy beamline and in the H2-2024 configuration. This can be seen in *Table* 7.2, where the names of magnets, their operating currents, and the power supplies used can be found. Here, no power supply is used in both the low-

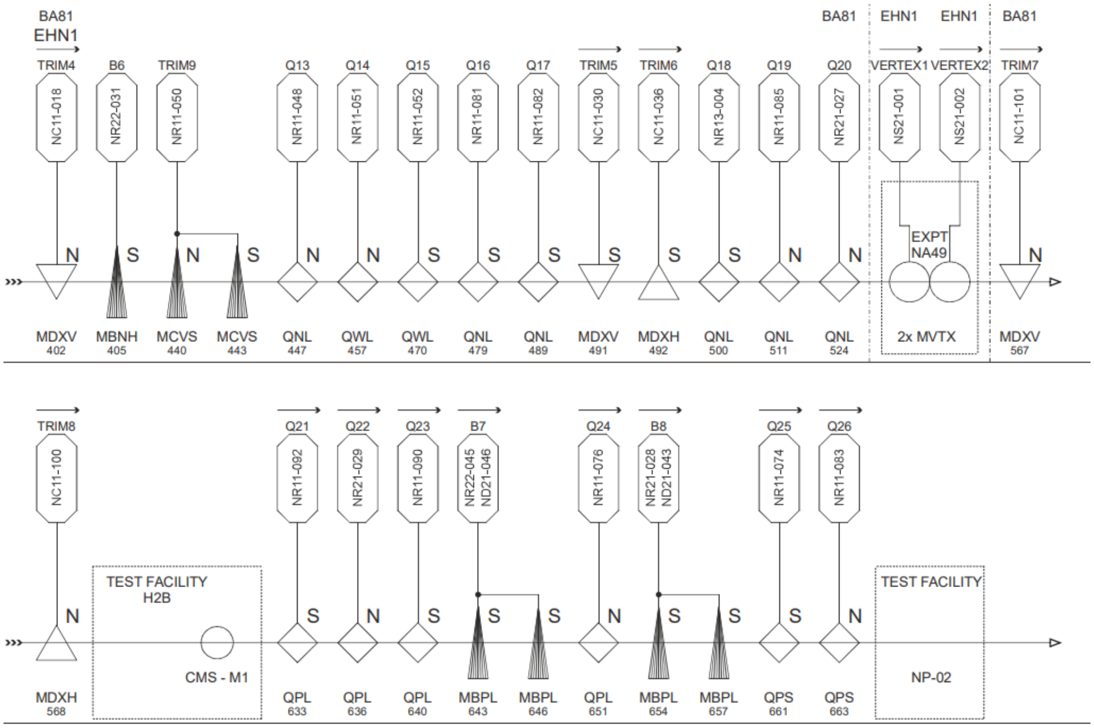

Figure 7.3: The magnets currently used in H2 and their corresponding power supplies [89]. In this figure, triangles represent trim magnets, the rotated squares are quadrupoles and the shaded triangles are bending magnets. The beam is incoming from the left hand side and the upper row of elements is upstream of the bottom row. Shown in the figure are also the vertex magnets of the NA61/SHINE detector.

energy configuration and in H2-2024, which leads to a greater efficiency when switching configurations. Additionally, this does not affect the use of the H2 beamline for test beams downstream of the NA61/SHINE experiment, as the PS of the low-energy configuration's magnets can be used for these optics without affecting the high-energy optics. This may prove to be important for the test beams which are expected to take place downstream using the H2 beamline in the future.

Name	Type	Necessary Current for Optics (A)	Power Supply Maximum Current (A)	PS NAME
QPL.X021.492	QPL	-619.66	1000	NR21-029
QPL.X021.494	QPL	455.28	500	NR11-092
MBPL.X021.497	MBPL	-741.00	1000	NR22-045 ND21-046
MBPL.X021.504	MBPL	741.00	1000	NR21-028 ND21-043
MBPL.021.509	MBPL	741.00	1000	NR21-028 ND21-043
MBPL.021.516	MBPL	-741.00	1000	NR22-045 ND21-046
QPL.021.519	QPL	236.16	500	NR11-090
QPL.021.523	QPL	-410.98	500	NR11-076
QPL.021.527	QPL	322.11	500	NR11-074
QNL.021.492	QNL	-	500	NR11-082
QPL.021.494	QPL	-	500	NR11-092
QNL.021.501	QNL	-	500	NR13-004
QPL.021.519	QPL	-	500	NR11-090
QPL.021.523	QPL	-	500	NR11-076
QNL.021.527	QNL	-	500	NR11-085

Table 7.2: A scheme to power each magnet in the low-energy beamline and in the H2-2024 configuration using only existing power supplies. The choice of PS used depends on the maximum current which will be needed. For the low-energy beamline magnets, this current is the one used when the beamline operates at 13 GeV/c. For H2-2024, currents higher than 500 A have not been necessary in the desired optics but these values have not been included due to the number of optics which have been considered.

7.3 Radiation Protection

The final consideration for the installation of the low-energy beamline in the North Area is the radiation it produces and whether this is within CERN's limits for radiation safety. To calculate this, FLUKA, a general-purpose Monte Carlo simulation code widely used for calculations of particle transport and interaction with matter, was used. In this section, the model which has been designed to study the Radiation Protection (RP) impacts of the beamline is described, alongside the results of these simulations in terms of dose-equivalent rates. With these, the feasibility of the low-energy beamline in H2 is assessed. Additionally, several changes to the shielding currently used in the H2 beamline are discussed.

7.3.1 A FLUKA Model of the Low-Energy Beamline

For FLUKA to provide an accurate estimate of the ambient dose equivalent produced by the beamline, it was important to produce an accurate model of not only the H2 low-energy beamline, but also of the shielding already present in the H2 beamline and any future modifications this may receive. The shielding, currently consisting of large concrete blocks, was simulated according to STEP files of the North Area, the same files used to generate *Figure* 7.2, while the beamline elements up to the collimator were placed according to the positions defined in the BEATCH files, including the elements of H2-2024. These elements were modelled using the information from Ref. [73].

This initial shielding however will have to be modified for the low-energy beamline. Here, the vicinity of the secondary target and the beam dump to two different access points, which can be seen in *Figure* 7.4, leads to insufficient shielding for containment of the radiation field. Additionally, the newly placed magnets would be too close to the shielding, leading to issues with the rails system described in the previous section and with CERN health and safety regulations regarding minimum distances to enable personnel to walk in the area.

With these issues in mind, the existing shielding was changed in the FLUKA simulations, following consultation with CERN experts to ensure that these modifications

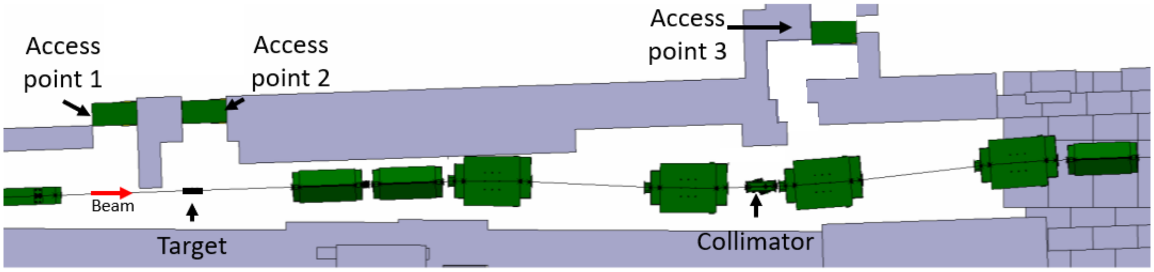

Figure 7.4: The current shielding configuration of the H2 beamline. Three different access points are present. If the low-energy beamline were to be built, these would be relatively close to the position of the new secondary target and collimator. Parts in grey are concrete blocks, while the metallic EHN1 safety system access doors are shown in green.

could be implemented in the future. First, the access point adjacent to the target was fully removed. This was the only solution to successfully shield the radiation field at this location without moving the secondary target. Secondly, the space around the target was widened, to allow space for safe passage, and iron shielding was added. This additional shielding consists of 80 cm by 80 cm by 160 cm iron blocks placed near the target to stop the highly energetic charged particles, and surrounded by concrete to stop the muons. Finally, the third access point was modified so that particles would have to travel through more material before being able to escape into the North Area. A concrete roofing was also added to the whole structure to prevent particles affecting the upper floors of the North Area. The changes can be seen in *Figure* 7.5, the $x - z$ view of the FLUKA input file used in these simulations.

7.3.2 Ambient Dose Equivalent Calculations

Simulations were performed with 1.5×10^5 400 GeV/c primary protons impinging onto the low-energy target, and then this result was normalised to 10^6 primary protons. With this normalisation, the ambient dose equivalent expected is identical to the value during operation to obtain the results shown in Chapter 5. The results of these simulations can be seen in *Figure* 7.6.

At CERN, for an area to be a *supervised* radiation area, requiring only a dosimeter, the ambient dose equivalent rate in a work location must stay below 3 μSv/hr and below

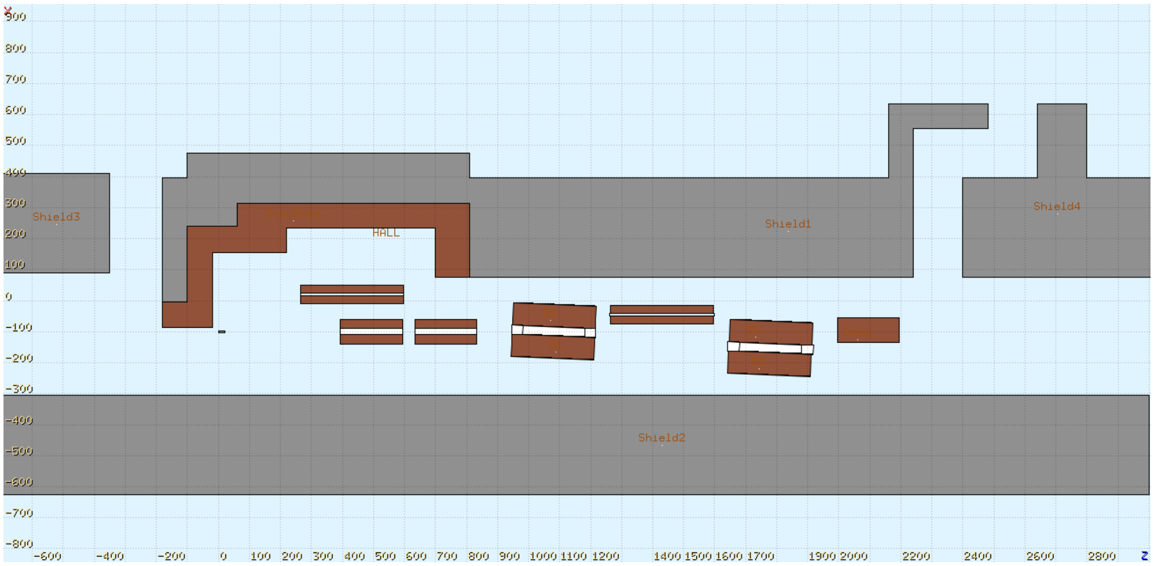

Figure 7.5: Modifications to H2's shielding. Some of the cement blocks are moved and others are replaced by iron blocks (shown in brown). Access point 1 is removed to contain the radiation field while access point 3 is modified to increase the shielding. The beamline has been modelled only up to the beam dump for simplicity.

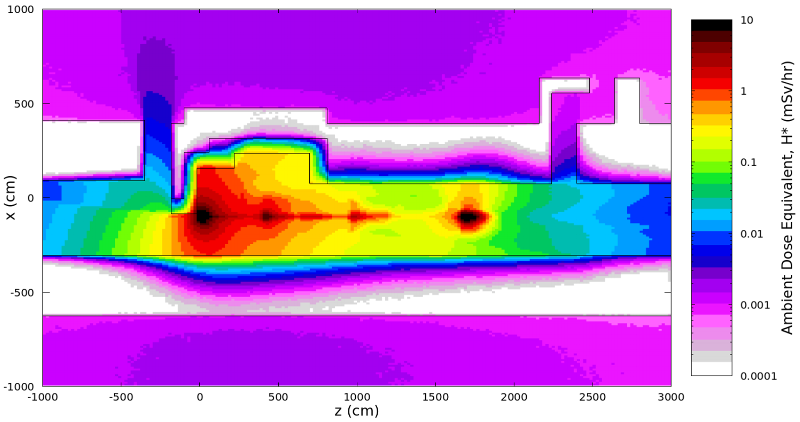

Figure 7.6: The x - z projection of the ambient dose equivalent produced by the low-energy beamline when shielded with the modified shielding. The ambient dose shown in this plot is normalised to 10^6 primary 400 GeV/c protons impinging on the target every 4.8 seconds, the duration of 1 SPS spill.

15 μSv/hr in low occupancy areas. Areas with higher ambient dose equivalent rates exist, such as the *simple* controlled area with the limit of 10 μSv/hr in working areas, exist but require special training to access [90].

EHN1 is designated as a *supervised* radiation, as such any beamline installed here cannot exceed the limit of 3 μSv/hr outside of the shielded area [91]. As can be seen from *Figure* 7.6, the beamline is within the limits imposed in EHN1 if 10^6 primary particles are used, with only some minor issues possibly arising at access point 1. Possible simple solutions to this problem exist and include either additional shielding or moving the access point, which constitutes the weak point of the shielding, to another location further upstream. Additionally, in the future, shielding modifications, such as the addition of more iron blocks, may enable the beamline's operation with a higher primary beam intensity, leading to higher rates of secondary particles to NA61/SHINE.

Chapter 8

Summary and Future Work

The NA61/SHINE collaboration has shown significant interest in cross section measurements of low-energy secondary hadrons to complement their ongoing neutrino programme. For these data to be collected, a novel, secondary low-energy beamline branch has been developed and optimised to be installed in CERN's North Area. This chapter gives an overview of the challenges faced during the development of this novel beamline and describes future work which may complement the studies shown in this thesis.

8.1 Summary

This optimisation process began by the choice of optimal targets for the production of the desired particles. For this process, several G4BL simulations were performed to estimate the yield and beam composition of each target. Following this, the three targets that produced beams with the highest yield, the lowest positron contamination and one performing as a middle ground were selected, to provide future flexibility to the experiment. The three targets will be installed on a remote switching station to enable NA61/SHINE to easily, safely, and rapidly change the target used in each run.

Following the selection of the target, the design of the beamline was started. Due to the various requirements and the vital importance of a high acceptance and particle rate, a new optimisation scheme was devised. This scheme is based on a grid parameter scan, and involves the calculation of the beamline's figures of merit for a large number of possible configurations. These figures of merit were then used to design the front end of the beamline and then the back end of the beamline. This design was subject to several constraints, from the limit on length to the magnets used and even the type of momentum selection structure which has been used, however, using this optimisation scheme, a beamline was found which satisfies all these requirements. Beyond the low-energy beamline for NA61/SHINE, the optimisation scheme developed in the context of this D.Phil may have a much broader applicability, and may prove to significantly simplify and improve the process of designing future beamlines.

Once the beamline design was completed, many simulations were performed to ensure the beamline would behave as desired and that even with a very conservative primary particle rate of 10^6 protons per spill onto the secondary target, the beamline's figures of merit would be satisfactory for the experiment. To this end, the entire beamline, from TCC2 to the NA61/SHINE TPC was simulated using G4BL and analysed, including not only the correct optics for the low-energy beamline, but also for the remainder of the H2 line. The results showed that the beamline's performance would be adequate to meet the desired specifications. Namely, the particle rates were sufficient for future experiments, the beam spot-size was small enough to interact with NA61/SHINE's target, and the beamline can be used to obtain momentum resolutions better than 1%. Additionally to these studies, a significant amount of work went into simulating accurately the QPL and MBPL magnets used in the North Area and their corresponding field maps. These were used to ensure that the particle rates would not be affected by realistic quadrupole fields, and more importantly that the backgrounds produced by decaying secondary pions would not overwhelm the low-energy signal. These additional simulations did not give rise to any new concerns regarding the suitability of the beamline design.

The final part of the beamline design involved the development of an instrumentation scheme to enable particle-by-particle identification of all secondaries over the relevant momentum ranges. This scheme relied on a scintillator, to obtain the total number of charged particles, a Time-of-Flight system, to separate particle pairs at the low end of the momentum range, and three Cherenkov Threshold Counters, filled with different gases at different pressures, to identify particles with momenta greater than approximately 4 GeV/c. When appropriately combined, these systems can provide all the desired information on the particles travelling through the beamline. These instruments were also simulated and their impact on the quality of the beam delivered to the NA61/SHINE experiment was assessed. While their impact on the higher end of the momentum range was small, at low momenta, especially at 4 GeV/c, the effects on the beam spot-size were significant. When considering these effects however, the beam spot-size is still within the requirements of NA61/SHINE at all energies.

Finally, this thesis addresses the implementation of the low-energy beamline into the North Area and how this can be done while maintaining the current capabilities of H2 and minimising the switching time between the high-energy and low-energy configurations. This was done using a system of magnets on rails to perform the switch on a time scale of one or two days. In addition to this, a brief description of the power supplies which can be used to power the magnets of the beamline, and where these are currently used has been included. The final section of this chapter focused on FLUKA simulations of the beamline and the modifications to the current shielding in H2 the low-energy beamline will require to operate within the radiation limits imposed by Radiation Protection at CERN.

8.2 Future Work

Further work on the optimisation of the instrumentation may be desirable. In this thesis, the scope of the gases used in the Threshold Cherenkov counters was limited to CO_2, He, N_2, as these could be implemented without any additional consideration on hazards posed by them. It may be possible to further improve the beam-spot sizes if more gases are considered.

Simulations of the interactions of the low-energy beam with the NA61/SHINE target, to better understand the necessary particle rates and analysis required by the low-energy programme, may also prove to be useful in the future and may be a worthwhile investment from the experiment.

There have also been discussions to include Gabor lenses to be used in the beamline design, with the work being spearheaded by the research group at Goethe University, Frankfurt. These lenses should be fully implemented in the simulations of the beamline before these are added to the low-energy beamline, such that their improvements over the baseline design can be fully benchmarked. The implementation of these devices offers significant potential for improvements over the beamline's spot-size in the lowest (< 2 GeV/c) momentum range.

Finally, while generally a complete scheme for the beamline's installation has been developed, this has not yet been finalised from all of CERN's stakeholders. As such, further fine tuning and additional work will certainly be involved. An example of this may be the optimisation and development of the beam dump which will be necessary to intercept the 400 GeV/c primary particles during low-energy operation.

Bibliography

[1] P. M. Watkins, "Discovery of the W and Z bosons," *Contemp. Phys.*, vol. 27, pp. 291–324, 1986.

[2] A. Collaboration, "Observation of a new particle in the search for the Standard Model Higgs boson with the ATLAS detector at the LHC," *Physics Letters B*, vol. 716, no. 1, pp. 1–29, 2012.

[3] CERN, "CERN's Accelerator Complex." `https://home.cern/science/accelerators/accelerator-complex`. Accessed: April 2023.

[4] J. Bernhard *et al.*, "The Beamlines of the CERN East Area Renovation Project," *9th International Particle Accelerator Conference*, pp. JACoW–IPAC2018–TUPAF023, 2018.

[5] B. Fastrup *et al.*, "CLOUD: An Atmospheric research facility at CERN," *CERN Document server*, vol. CERN-SPSC-2000-041, 10 2000.

[6] R. Froeschl, M. Brugger, and S. Roesler, "The CERN High Energy Accelerator Mixed Field (CHARM) Facility in the CERN PS East Experimental Area," in *12th Meeting of Task-Force on Shielding Aspects of Accelerators, Targets and Irradiation Facilities*, pp. 14–25, 2015.

[7] G. Arduini, J. Jaeckel, and C. Vallée, "Preparing for post-LS3 scenarios," *CERN Courier*, 2023.

[8] M. Chanel, "LEIR: the low energy ion ring at CERN," *Nuclear Instruments and Methods in Physics Research Section A: Accelerators, Spectrometers, Detectors and Associated Equipment*, vol. 532, no. 1, pp. 137–143, 2004. International Workshop on Beam Cooling and Related Topics.

[9] J. Jaeckel, M. Lamont, and C. Vallée, "Summary Report of Physics Beyond Colliders at CERN," Tech. Rep. CERN-PBC-REPORT-2018-003, CERN, Geneva, Switzerland, 2018.

[10] D. Banerjee *et al.*, "The North Experimental Area at the Cern Super Proton Synchrotron," Tech. Rep. CERN-ACC-NOTE-2021-0015, CERN, Geneva, Switzerland, 2021.

[11] M. Rosenthal *et al.*, "Commissioning results of the tertiary beam lines for the CERN neutrino platform project," *J. Phys.: Conf. Ser.*, vol. 1350, no. CERN-ACC-2019-241, 2019.

[12] J. Jaeckel, M. Lamont, and C. Vallee, "Summary Report of Physics Beyond Colliders at CERN," Tech. Rep. CERN-PBC-REPORT-2018-003, CERN, Geneva, Switzerland, 2018.

[13] N. Abgrall *et al.*, "NA61/SHINE facility at the CERN SPS: beams and detector system," *JINST*, vol. CERN-PH-EP-2014-003, p. 06005, 2014.

[14] A. László *et al.*, "Design and Performance of the Data Acquisition System for the NA61/SHINE Experiment at CERN," *Nucl. Instrum. Methods Phys. Res., A*, vol. 798, p. 1, 2015.

[15] M. Gazdzicki, M. Gorenstein, and P. Seyboth, "Onset of deconfinement in nucleus-nucleus collisions: review for pedestrians and experts," *Acta Physica Polonica B*, vol. 42, no. 2, p. 307, 2011.

[16] N. Abgrall, "NA61/SHINE plans beyond the approved program ," Tech. Rep. SPSC-P-330-ADD-6, CERN, Geneva, 2012.

[17] Y. Nagai, "Addendum to the NA61/SHINE Proposal: A Low-Energy Beamline at the SPS H2," Tech. Rep. SPSC-P-330-ADD-12, CERN, Geneva, Switzerland, 2021.

[18] k. Abe *et al.*, “The t2k experiment,” *Nuclear Instruments and Methods in Physics Research Section A: Accelerators, Spectrometers, Detectors and Associated Equipment*, vol. 659, no. 1, pp. 106–135, 2011.

[19] F. Di Lodovico and on behalf of the Hyper-Kamiokande Collaboration, “The hyper-kamiokande experiment,” *Journal of Physics: Conference Series*, vol. 888, p. 012020, sep 2017.

[20] B. Abi *et al.*, “Volume i. introduction to dune,” *Journal of Instrumentation*, vol. 15, p. T08008, aug 2020.

[21] C. Rott and on behalf of theJSNS2 Collaboration, “Status of jsns2 - j-parc sterile neutrino search at j-parc spallation neutron source,” *Journal of Physics: Conference Series*, vol. 1468, p. 012176, feb 2020.

[22] K. Nakajima *et al.*, “Materials and life science experimental facility (mlf) at the japan proton accelerator research complex ii: Neutron scattering instruments,” *Quantum Beam Science*, vol. 1, no. 3, 2017.

[23] “NA61/SHINE at Low Energy Workshop.” `https://indico.cern.ch/event/973899/`, December 2020. CERN, Geneva, Switzerland.

[24] N. Charitonidis and I. Efthymiopoulos, “Low energy tertiary beam line design for the CERN neutrino platform project,” *Phys. Rev. Accel. Beams*, vol. 20, no. 11, p. 111001, 2017.

[25] CERN Engineering Department, “How to control the north area beamlines.” `http://sba.web.cern.ch/sba/documentations/how2controlnabeams.htm`, 2023. Accessed: 2023-06-01.

[26] P. Coet, N. T. Doble, and S. Reucroft, “Beam possibilities for the European Hybrid Spectrometer,” Tech. Rep. CERN-SPS-81-25-EBP, CERN, Geneva, Switzerland, 1982.

[27] L. Gatignon, "Design and Tuning of Secondary Beamlines in the CERN North and East Areas," Tech. Rep. CERN-ACC-NOTE-2020-0043, CERN, Geneva, Switzerland, 9 2020.

[28] S. Ilieva, "Hadron production measurements at NA61/SHINE for precise determination of accelerator neutrino fluxes," *Phys. Part. Nuclei*, vol. 53, pp. 212–216, 2022.

[29] R. L. Workman *et al.*, "Fragmentation Functions in e+, e-, ep and pp collisions," *Prog. Theor. Exp. Phys.*, vol. 083C01, 2022.

[30] H. Wiedemann, *Particle Accelerator Physics.* Graduate Texts in Physics, Springer, 4 ed., 2015.

[31] S. Y. Lee, *Accelerator Physics (Fourth Edition).* World Scientific, 2018.

[32] H. Wollnik, "8 - Image Aberrations," in *Optics of Charged Particles* (H. Wollnik, ed.), pp. 210–252, Academic Press, 1987.

[33] L. Conradie, "Introduction to Beam Optics," in *Joint ICTP-IAEA Workshop on Accelerator Technologies, Basic Instruments and Analytical Techniques*, (Trieste, Italy), 2019.

[34] P. Chatzidaki, *Optics optimization of tertiary particle beamlines and efficiency measurement of prototype scintillating fiber detectors.* PhD thesis, National Technical University Athens, 2018. Presented Oct 2018.

[35] M. Martini, "AN INTRODUCTION TO TRANSVERSE BEAM DYNAMICS IN ACCELERATORS," 1996. in CERN/PS 96-11.

[36] S. Guiducci, "CHROMATICITY," in *CAS - CERN Accelerator School : 5th General Accelerator Physics Course, pp.191-206*, (Jyväskylä, Finland), 1994.

[37] P. Coet and N. Doble, "AN INTRODUCTION TO THE DESIGN OF HIGH-ENERGY CHARGED PARTICLE BEAMS," *CERN Libraries, CERN/SPS/86/23*, 1986.

[38] E. Parozzi, *"Design and optimisation of a variable momentum secondary beamline for the NP06/ENUBET project"*. PhD thesis, Milan Bicocca University, 2023.

[39] B. Holzer, ed., *Particle Interactions with Matter*, vol. 5/2018 of *CERN Yellow Reports: School Proceedings*, (Geneva, Switzerland), CERN, 2018. CERN-2018-008-SP.

[40] R. L. Workman *et al.*, "Passage of Particles Through Matter," *Prog. Theor. Exp. Phys.*, vol. 083C01, 2022.

[41] R. L. Workman *et al.*, "Atomic and Nuclear Properties of Materials for more than 350 materials," *Prog. Theor. Exp. Phys.*, vol. 083C01, 2022.

[42] K. Brown, D. Carey, C. Iselin, and F. Rothacker, "TRANSPORT A COMPUTER PROGRAM FOR DESIGNING CHARGED PARTICLE SYSTEMS," *CERN Libraries, CERN/SPS/80/04*, 1980.

[43] L. Deniau and H. Grote and G. Roy and F. Schmidt, *"The MAD-X Program (Methodical Accelerator Design) Version 5.02.08 User's Reference Manual"*. CERN, Geneva, Switzerland, 2022, `https://mad.web.cern.ch/mad/webguide/manual.html`.

[44] L. Deniau, "MAD-X progress and future plans," in *Proceedings of International Conference on Atomic Physics (ICAP) 2012*, vol. 1, (Rostock-Warnemünde, Germany), pp. 211–226, 2012.

[45] A. Adelmann and others, "The OPAL Framework - Version 2022.1-dev." (Zurich, Switzerland), p. 221 – 235, 2018, `http://amas.web.psi.ch/opal/Documentation/master/Manual.pdf` .

[46] P. K. Skowronski, F. Schmidt, and E. Forest, "Advances in MAD X using PTC," *Conf. Proc. C*, vol. PAC07.070625, p. 3381, 2007.

[47] L. Nevay *et al.*, "BDSIM: An accelerator tracking code with particle–matter interactions," *Computer Physics Communications*, vol. 252, p. 107200, 2020.

[48] T. Roberts and D. M. Kaplan, “G4beamline simulation program for matter-dominated beamlines,” *2007 IEEE Particle Accelerator Conference (PAC)*, pp. 3468–3470, 2007.

[49] J. Kunz, P. Snopok, M. Berz, and K. Makino, “Hybrid methods for muon accelerator simulations with ionization cooling,” *Journal of Instrumentation*, vol. 13, p. P07026, Jul 2018.

[50] C. Yoshikawa and D. Neuffer, “NEUTRINO FACTORY/MUON COLLIDER FRONT END SIMULATION COMPARISONS AND ECONOMIZATION OF RF CAVITIES,” in *Proceedings of PAC09*, vol. 1, (Vancouver, BC, Canada), pp. 2709 – 2711, 2009.

[51] N. Charitonidis, P. Chatzidaki, Y. Karyotakis, and M. Rosenthal, “Particle identification in the low-GeV/c regime using Octafluoropropane (R-218) as Cherenkov radiator,” *Nuclear Instruments and Methods in Physics Research Section B: Beam Interactions with Materials and Atoms*, vol. 457, pp. 20–23, 2019.

[52] N. Charitonidis, A. Longhin, M. Pari, E. G. Parozzi, and F. Terranova, “Design and Diagnostics of High-Precision Accelerator Neutrino Beams,” *Applied Sciences*, vol. 11, p. 1644, February 2021.

[53] N. Charitonidis, I. Efthymiopoulos, and Y. Karyotakis, “Beam performance and instrumentation studies for the ProtoDUNE-DP experiment of CENF,” *CERN-ACC-NOTE-2016-0052*, 2016.

[54] C. Ahdida *et al.*, “FLUKA website.” `https://fluka.cern`, 2023. Accessed: June 2023.

[55] C. Ahdida *et al.*, “New Capabilities of the FLUKA Multi-Purpose Code,” *Front. Phys.*, vol. 9, p. 788253, 2022.

[56] G. Battistoni *et al.*, “Overview of the FLUKA code,” *Annals of Nuclear Energy*, vol. 82, pp. 10–18, 2015.

[57] L. Mokhtari Oranj, M. Bakhtiari, K. Yong Uk, J. Nam Suk, A. Lee, and L. Hee Seock, “Benchmarking FLUKA, PHITS, MCNPX, and MARS15 codes with product yields of 209Bi(p, x) reactions,” *Nuclear Instruments and Methods in Physics Research Section B: Beam Interactions with Materials and Atoms*, vol. 462, pp. 154–162, 2020.

[58] G. Aricò, G. Battistoni, F. Cerutti, F. Horst, A. Mairani, C. Schuy, U. Weber, and A. Ferrari, “Benchmarking of FLUKA production cross sections of positron emission tomography isotopes for in-vivo range verification in hadron therapy,” *EPJ Web Conf.*, vol. 239, p. 24001, 2020.

[59] V. Vlachoudis, “FLAIR: A Powerful But User Friendly Graphical Interface For FLUKA,” *Proc. Int. Conf. on Mathematics, Computational Methods & Reactor Physics*, 2009. Saratoga Springs, New York.

[60] W. Heitler, *The Quantum Theory of Radiation.* Oxford University Press, 3rd ed., 1954. Section 38.

[61] J. Matthews, “A Heitler model of extensive air showers,” *Astroparticle Physics*, vol. 22, pp. 387–397, January 2005.

[62] H. W. Atherton *et al.*, “Precise measurements of particle production by 400 GeV/c protons on beryllium targets,” Tech. Rep. CERN Yellow Reports: Monographs, 10.5170/CERN-1980-007, CERN, Geneva, Switzerland, 1980.

[63] M. Bonesini, “The NA56/SPY experiment at CERN,” in *1997 Europhysics Conference on High Energy Physics*, pp. 866–867, 1997.

[64] N. Charitonidis and I. Efthymiopoulos, “Low energy tertiary beam line design for the CERN neutrino platform project,” *Phys. Rev. Accel. Beams*, vol. 20, p. 111001, Nov 2017.

[65] M. Novak, “Short Guide to Choosing Your Physics Lists,” in *First GEANT4 workshop in São Paulo*, (Instituto de Física da Universidade, São Paulo, Brasil), February 2019.

[66] K. Abe *et al.*, “T2K neutrino flux prediction,” *Phys. Rev. D*, vol. 87, p. 012001, Jan 2013.

[67] R. L. Workman *et al.*, “Kinematics,” *Prog. Theor. Exp. Phys.*, vol. 083C01, 2022.

[68] F. James, “MINUIT: Function Minimization and Error Analysis Reference Manual,” Tech. Rep. CERNLIB-D506, CERN, Geneva, Switzerland, 8 1998.

[69] E. Regenstreif, “Phase acceptance of quadrupole triplets in terms of matrix elements,” Tech. Rep. CERN-70-22, CERN, Geneva, Switzerland, 7 1970.

[70] E. Regenstreif, “Phase acceptance of an alternating gradient doublet made of quadrupoles of different apertures,” Tech. Rep. CERN-71-11, CERN, Geneva, Switzerland, 5 1971.

[71] E. Regenstreif, “Phase Space Acceptance of a General Triplet,” tech. rep., CERN, Geneva, Switzerland, 1970.

[72] Wes McKinney, “Data Structures for Statistical Computing in Python,” in *Proceedings of the 9th Python in Science Conference* (Stéfan van der Walt and Jarrod Millman, eds.), pp. 56 – 61, 2010.

[73] L. Gatignon, “Magnets Kit for the Experimental Areas of the CERN PS/SPS complex,” Tech. Rep. CERN-OPEN-2004-003, CERN, Geneva, Switzerland, 1991.

[74] Private communication between Dr. N. Charitonidis and C. Mussolini in September 2020.

[75] E. Regenstreif, “Remarks on the phase acceptance of a quadrupole multiplet application to the doublet and the symmetric triplet,” *Proceedings, 7th International Conference on High-Energy Accelerators, HEACC 1969*, vol. 1, pp. 669–674, 1969.

[76] K. L. Brown and A. C. Hindmarsh, "Properties of Symmetric Quadrupole Magnet Triplets," *SLAC Report*, vol. SLAC-0047, 8 1965.

[77] E. Regenstreif, "Acceptance angulaire du quadruplet de retournement," Tech. Rep. CERN-68-06, CERN, Geneva, Switzerland, 2 1968.

[78] CERN, "North Area Handbook - User's manual to the beam lines in the North area." `https://nahandbook.web.cern.ch/default/`, 2023. Accessed: 2023-04-01.

[79] A. Gerbershagen, "Beam Generation for Test Beams," in *7th Beam Telescopes and Test Beams Workshop*, (Geneva, Switzerland), 2019.

[80] T. Roberts, "G4beamline User's Guide," February 2017.

[81] Dassault Systèmes, "OPERA, ELECTROMAGNETIC AND ELECTROMECHANICAL SIMULATION." `https://www.3ds.com/products-services/simulia/products/opera/`, 2023. Accessed: 2023-06-01.

[82] A. C. Booth *et al.*, "Particle production, transport, and identification in the regime of $1-7$ GeV/c," *Phys. Rev. Accel. Beams*, vol. 22, p. 061003, Jun 2019.

[83] H. Kragh, "The Lorenz-Lorentz Formula: Origin and Early History," *Substantia*, vol. 2, p. 7–18, September 2018.

[84] D. Dannheim, K. Elsener, W. Klempt, A. Lucaci Timoce, and E. van der Kraaij, "Particle Identification with Cherenkov detectors in the 2011 CALICE Tungsten Analog Hadronic Calorimeter Test Beam at the CERN SPS," Tech. Rep. LCD-Note-2013-006, AIDA-NOTE-2015-012, CERN, Geneva, Switzerland, 2013.

[85] Private communication, exchanges with Dr. Y. Nagai and Dr. E. D. Zimmerman for the NA61 Collaboration, Winter 2022.

[86] Private communication between Dr. N. Charitonidis and C. Mussolini in Winter 2022.

[87] G. Burton, M. Hanney, and P. Strolin, "BEATCH: a Fortran programme for the particle optics of beam transfer channels," Tech. Rep. CERN-ISR-BT-TH-69-27, ISR-BT-TH-69-27, CERN, Geneva, Switzerland, 1969.

[88] Private communication between S. Girod, V. Clerc, Dr. N. Charitonidis, and C. Mussolini in Summer 2021.

[89] G. Arduini *et al.*, "ELECTRICAL CIRCUITS LAYOUT BETWEEN CONVERTERS AND MAGNETS SPS NORTH AREA," October 2018. TE/MSC/MNC 1062808.

[90] D. Forkel-Wirth, S. Roesler, M. Silari, M. Streit-Bianchi, C. Theis, H. Vincke, and H. Vincke, "Radiation protection at CERN," *CERN Yellow Report*, vol. CERN-2013-001, pp. 415 – 436, 2013.

[91] D. Forkel-Wirth and T. Otto, "Règles Générales d'Exploitation Consignes Générales de Radioprotection Area Classification," in *CERN RGE*, Section 9/S3-GSI1, (Geneva, Switzerland), 12 2006.

Appendix A

Target Simulations Analyses at Other Momenta

In this appendix the results of particle yields and beam compositions for several different secondary nominal momenta are presented. All of these values are obtained considering the acceptance cuts for the low-energy beamline and assume a decay distance of 50 meters.

A.1 Effect of the primary beam's momentum

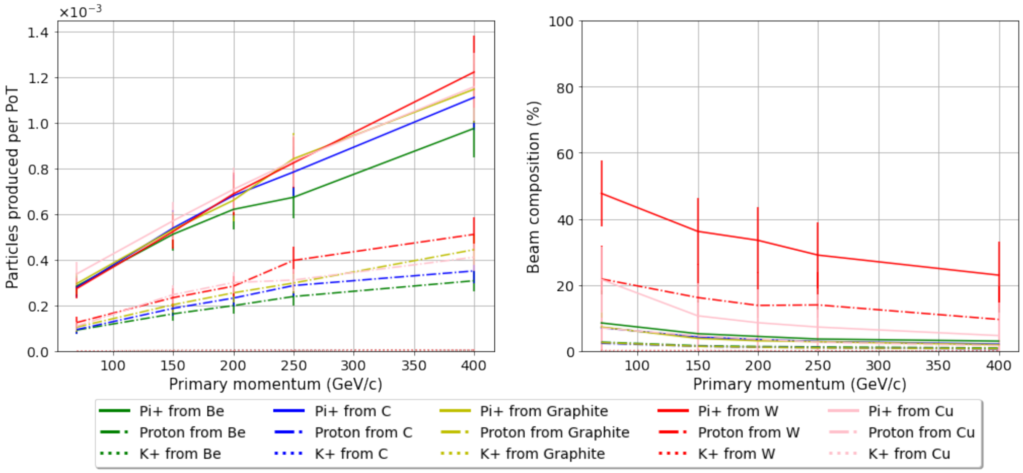

Figure A.1: Effect of the primary beam's momentum on hadron production centred at 2 GeV/c (±10%) from targets made of several different materials. *Left*: The number of hadrons produced per particle on target as a function of primary momentum. *Right*: The beam composition reaching the end of the beamline as a function of primary momentum, not shown is the positron content.

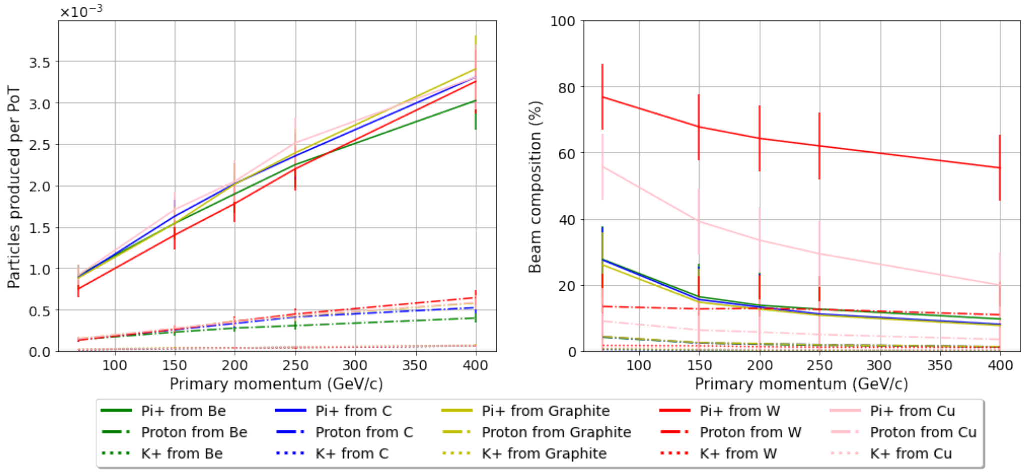

Figure A.2: Effect of the primary beam's momentum on hadron production centred at 4 GeV/c (±10%) from targets made of several different materials. *Left*: The number of hadrons produced per particle on target as a function of primary momentum. *Right*: The beam composition reaching the end of the beamline as a function of primary momentum, not shown is the positron content.

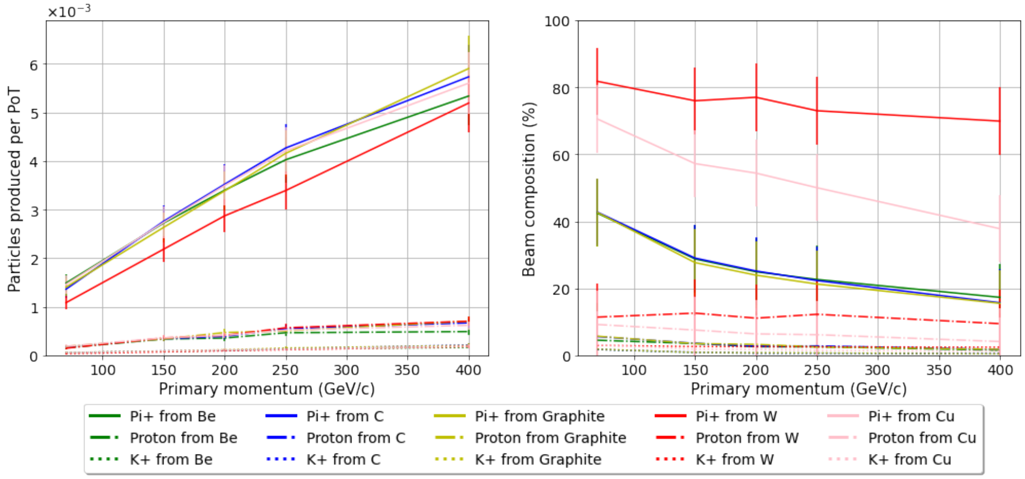

Figure A.3: Effect of the primary beam's momentum on hadron production centred at 6 GeV/c (±10%) from targets made of several different materials. *Left*: The number of hadrons produced per particle on target as a function of primary momentum. *Right*: The beam composition reaching the end of the beamline as a function of primary momentum, not shown is the positron content.

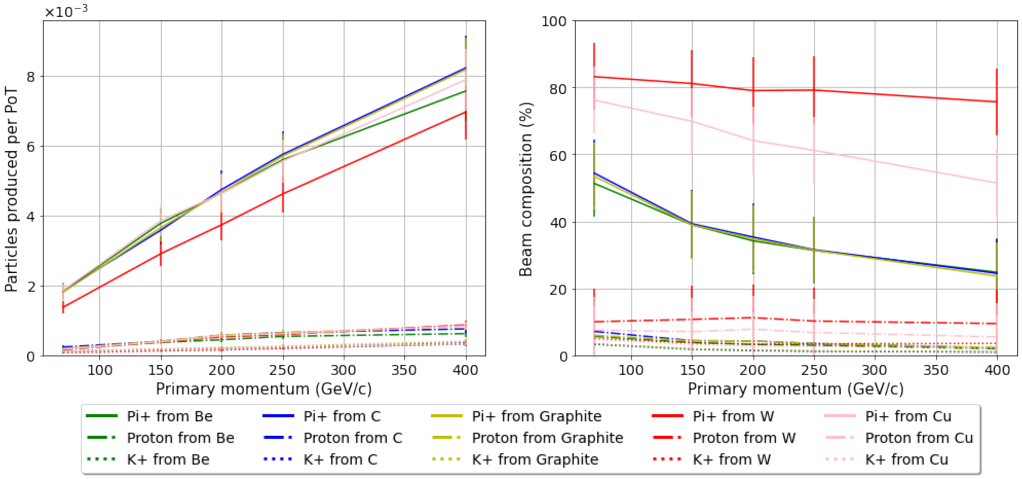

Figure A.4: Effect of the primary beam's momentum on hadron production centred at 8 GeV/c (±10%) from targets made of several different materials. *Left*: The number of hadrons produced per particle on target as a function of primary momentum. *Right*: The beam composition reaching the end of the beamline as a function of primary momentum, not shown is the positron content.

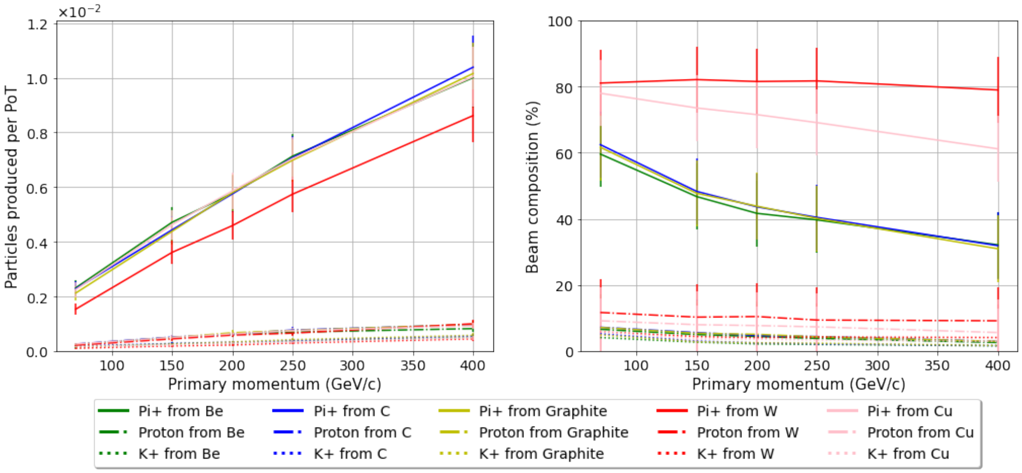

Figure A.5: Effect of the primary beam's momentum on hadron production centred at 10 GeV/c (±10%) from targets made of several different materials. *Left*: The number of hadrons produced per particle on target as a function of primary momentum. *Right*: The beam composition reaching the end of the beamline as a function of primary momentum, not shown is the positron content.

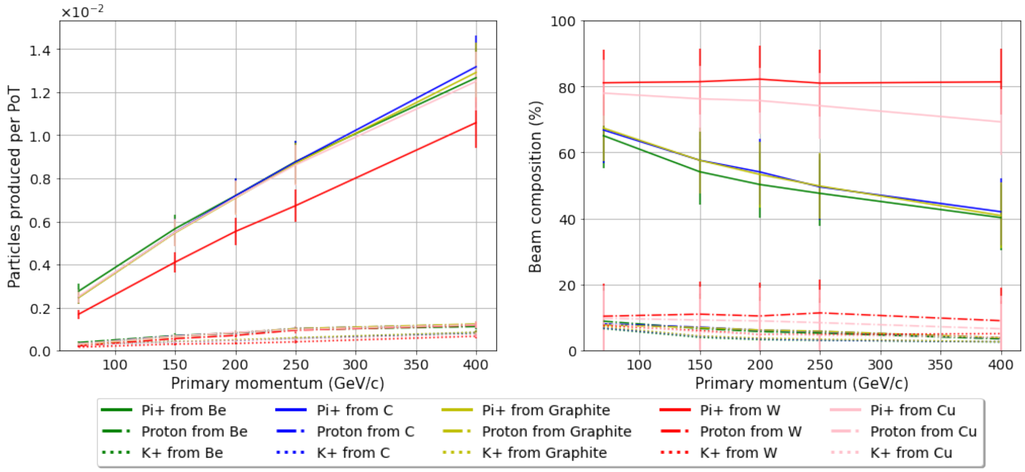

Figure A.6: Effect of the primary beam's momentum on hadron production centred at 13 GeV/c ($\pm 10\%$) from targets made of several different materials. *Left*: The number of hadrons produced per particle on target as a function of primary momentum. *Right*: The beam composition reaching the end of the beamline as a function of primary momentum, not shown is the positron content.

A.2 Effect of Target Length

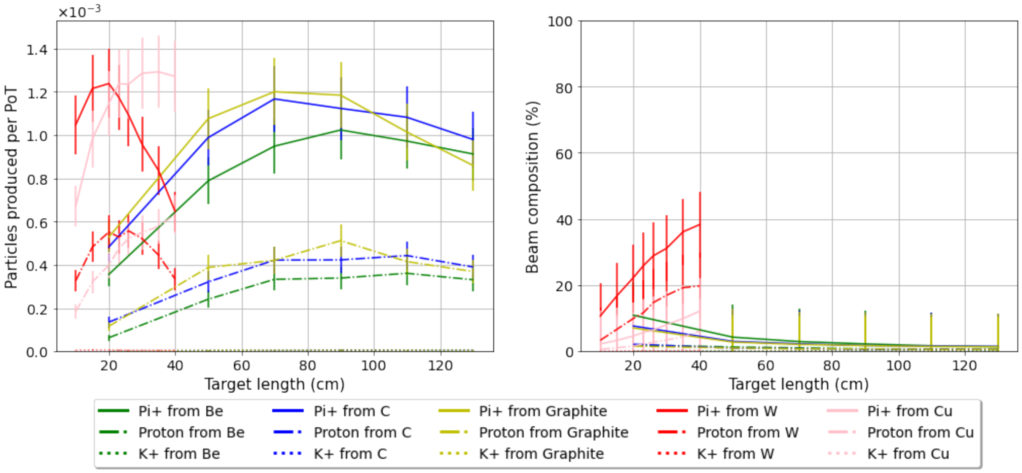

Figure A.7: Effect of varying the target length on hadron production centred at 2 GeV/c (±10%) from targets made of several different materials. *Left*: The number of hadrons produced per particle on target as a function of target length. *Right*: The beam composition reaching the end of the beamline as a function of target length, not shown is the positron content.

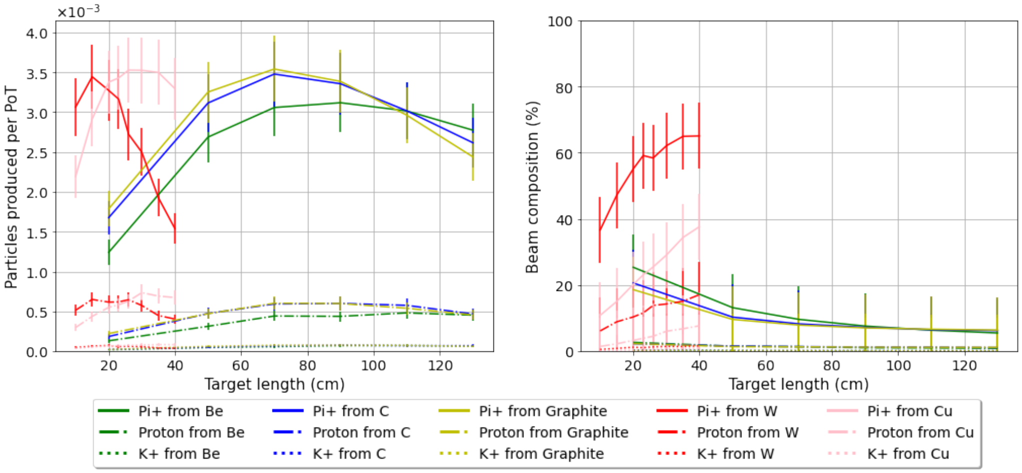

Figure A.8: Effect of varying the target length on hadron production centred at 4 GeV/c (±10%) from targets made of several different materials. *Left*: The number of hadrons produced per particle on target as a function of target length. *Right*: The beam composition reaching the end of the beamline as a function of target length, not shown is the positron content.

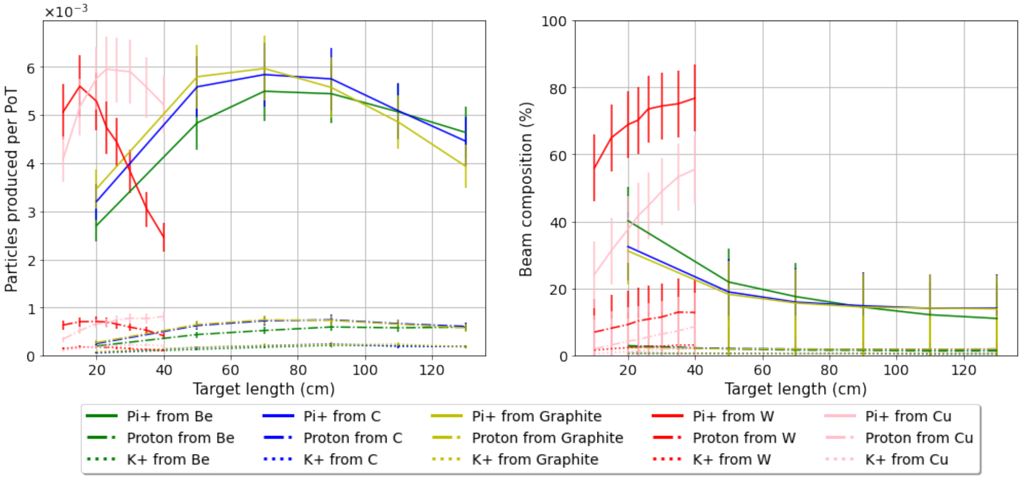

Figure A.9: Effect of varying the target length on hadron production centred at 6 GeV/c (±10%) from targets made of several different materials. *Left*: The number of hadrons produced per particle on target as a function of target length. *Right*: The beam composition reaching the end of the beamline as a function of target length, not shown is the positron content.

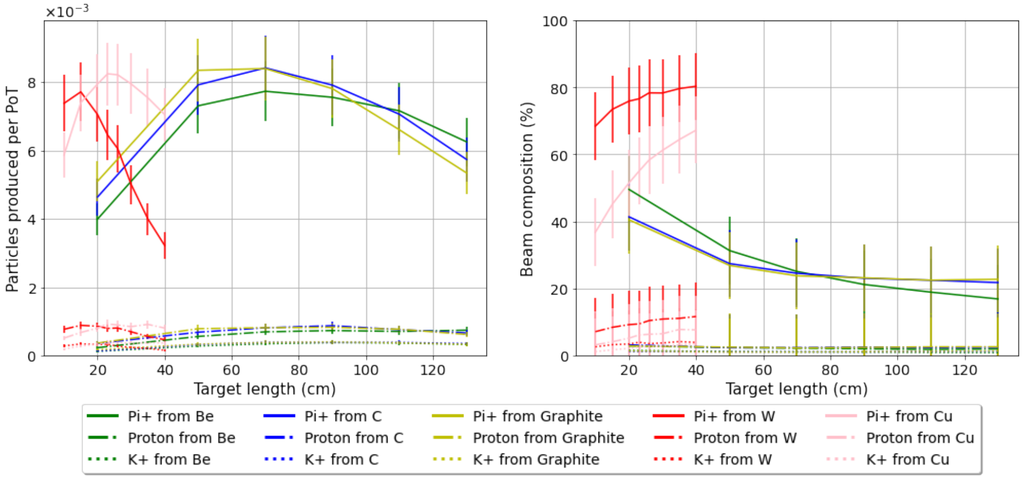

Figure A.10: Effect of varying the target length on hadron production centred at 8 GeV/c (±10%) from targets made of several different materials. *Left*: The number of hadrons produced per particle on target as a function of target length. *Right*: The beam composition reaching the end of the beamline as a function of target length, not shown is the positron content.

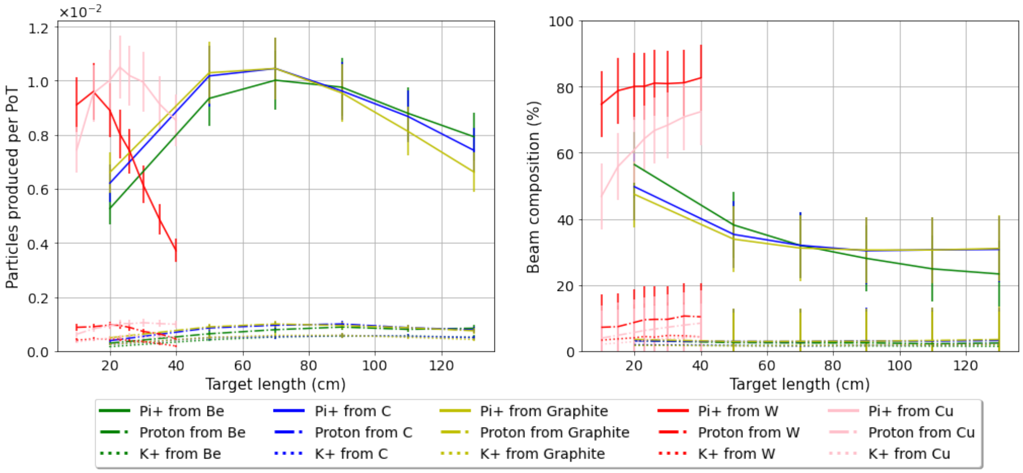

Figure A.11: Effect of varying the target length on hadron production centred at 10 GeV/c (±10%) from targets made of several different materials. *Left*: The number of hadrons produced per particle on target as a function of target length. *Right*: The beam composition reaching the end of the beamline as a function of target length, not shown is the positron content.

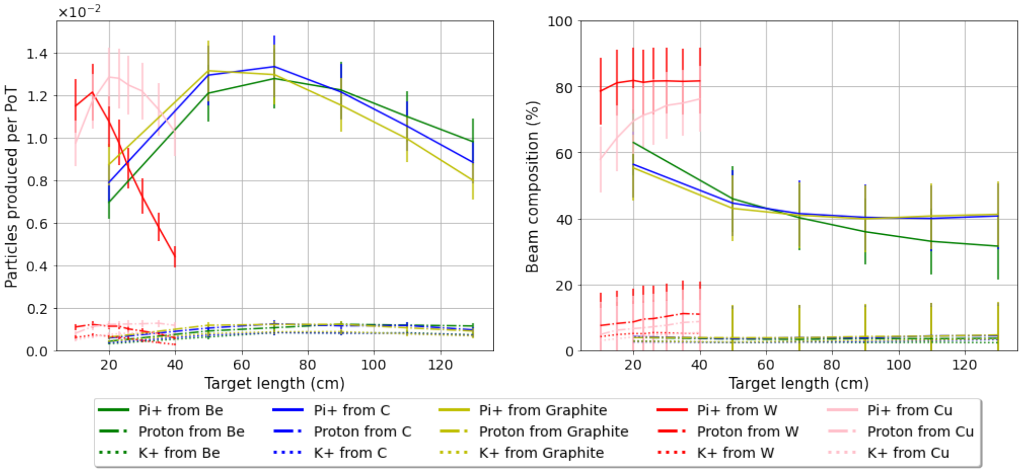

Figure A.12: Effect of varying the target length on hadron production centred at 13 GeV/c ($\pm 10\%$) from targets made of several different materials. *Left*: The number of hadrons produced per particle on target as a function of target length. *Right*: The beam composition reaching the end of the beamline as a function of target length, not shown is the positron content.

A.3 Effect of Target Radius

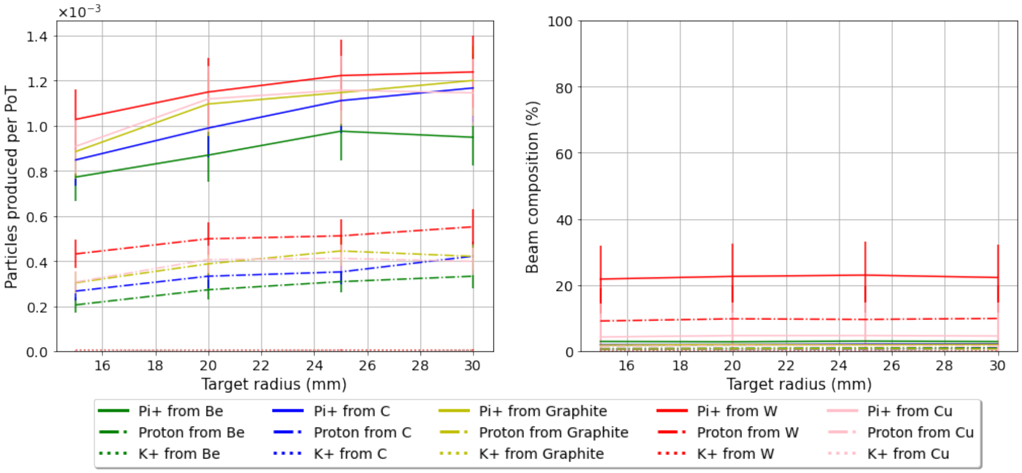

Figure A.13: Effect of varying the target radius on hadron production centred at 2 GeV/c ($\pm 10\%$) from targets made of several different materials. *Left*: The number of hadrons produced per particle on target as a function of target radius. *Right*: The beam composition reaching the end of the beamline as a function of target radius, not shown is the positron content.

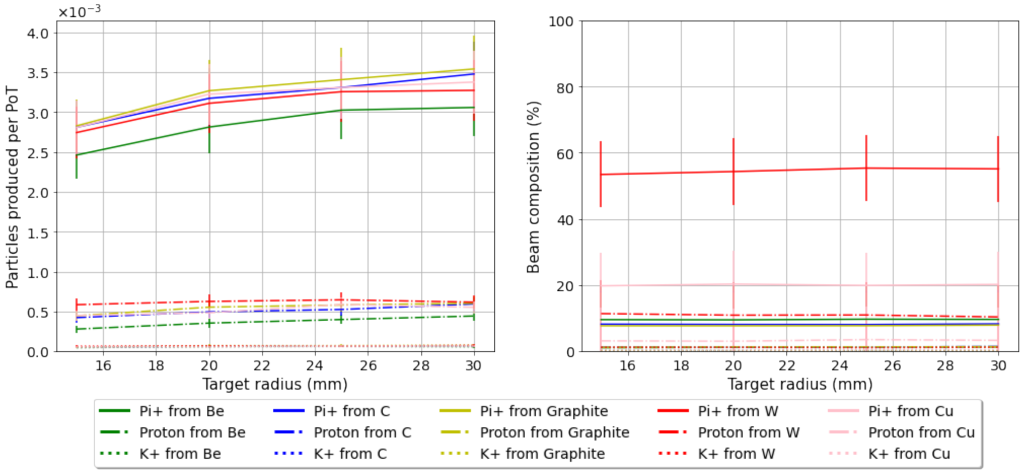

Figure A.14: Effect of varying the target radius on hadron production centred at 4 GeV/c ($\pm 10\%$) from targets made of several different materials. *Left*: The number of hadrons produced per particle on target as a function of target radius. *Right*: The beam composition reaching the end of the beamline as a function of target radius, not shown is the positron content.

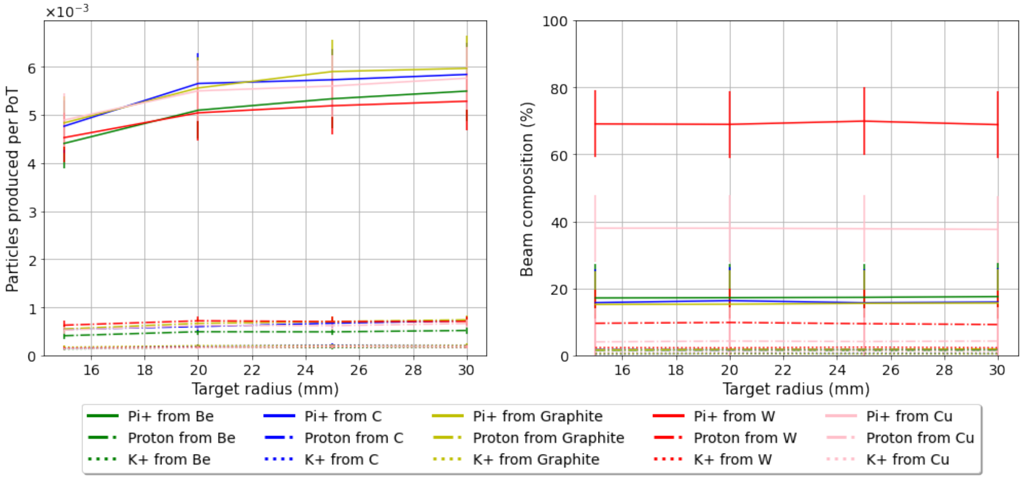

Figure A.15: Effect of varying the target radius on hadron production centred at 6 GeV/c ($\pm 10\%$) from targets made of several different materials. *Left*: The number of hadrons produced per particle on target as a function of target radius. *Right*: The beam composition reaching the end of the beamline as a function of target radius, not shown is the positron content.

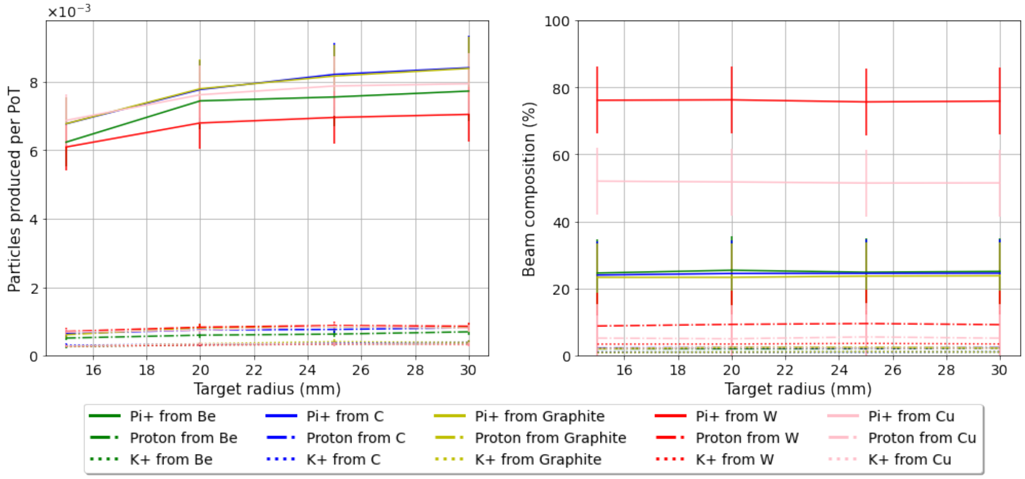

Figure A.16: Effect of varying the target radius on hadron production centred at 8 GeV/c ($\pm10\%$) from targets made of several different materials. *Left*: The number of hadrons produced per particle on target as a function of target radius. *Right*: The beam composition reaching the end of the beamline as a function of target radius, not shown is the positron content.

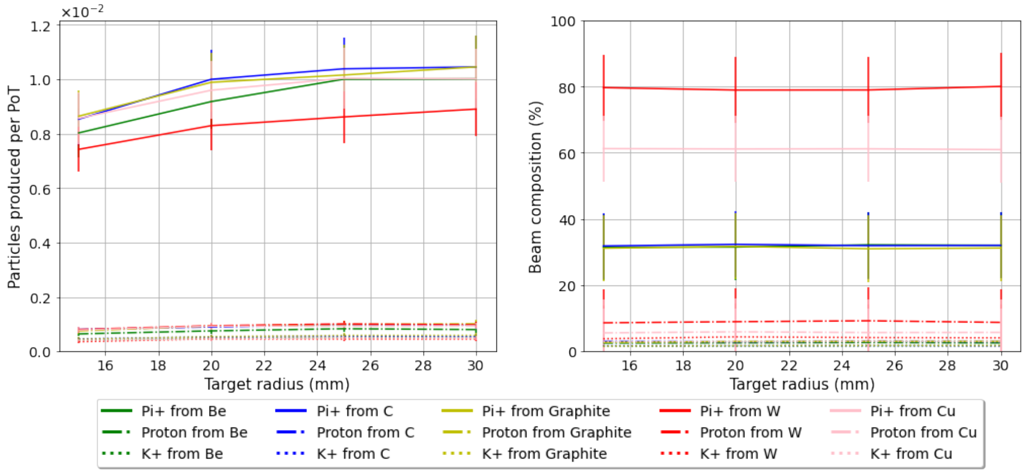

Figure A.17: Effect of varying the target radius on hadron production centred at 10 GeV/c ($\pm10\%$) from targets made of several different materials. *Left*: The number of hadrons produced per particle on target as a function of target radius. *Right*: The beam composition reaching the end of the beamline as a function of target radius, not shown is the positron content.

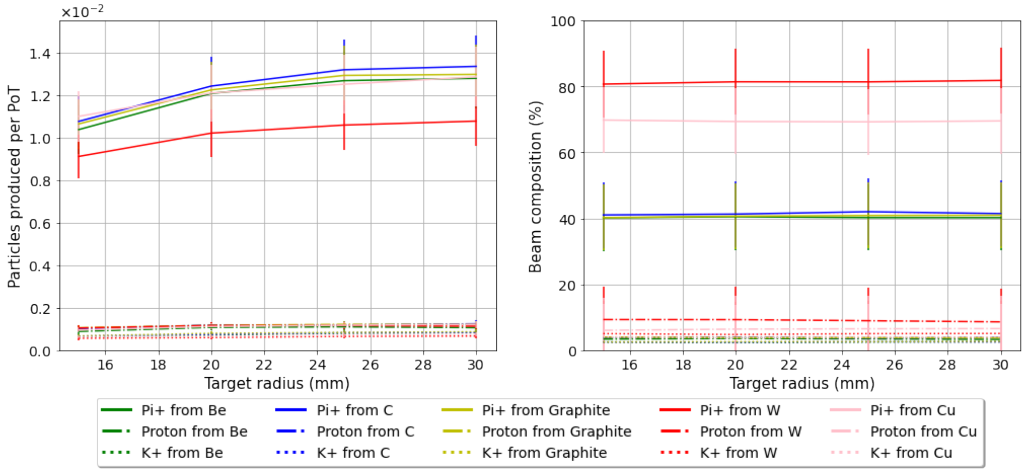

Figure A.18: Effect of varying the target radius on hadron production centred at 13 GeV/c (±10%) from targets made of several different materials. *Left*: The number of hadrons produced per particle on target as a function of target radius. *Right*: The beam composition reaching the end of the beamline as a function of target radius, not shown is the positron content.

Appendix B

Low-Energy Beamline Parameters

Here are presented the final parameters of the low-energy beamline. *Table* B.1 contains the distances between magnets of the low-energy beamline.

Name	Distance (m)
d1	3.737
d2	0.860
d3	1.016
d4	5.000
d5	1.100
d6	0.705
d7	5.000
d8	1.041
d9	2.022
d10	1.260
d11	8.435

Table B.1: The distances between the various elements in the low-energy beamline. These distances are between the magnetic fields, so do not take into account the coils of magnets.

Table B.2, on the other hand, contains the magnetic gradients and magnetic field strengths of the quadrupoles and dipoles in the low-energy beamline at a nominal momentum of 13 GeV/c.

Element	Strength (T·M, T/M · M)
Q1	-19.8816
Q2	15.4517
Q3	8.0512
Q4	-14.0095
Q5	10.9812
B1	3.5000
B2	-3.5000
B3	-3.5000
B4	3.5000

Table B.2: The magnetic fields and magnetic field gradients of the magnets in the low-energy beamline.

Appendix C

QPL and G4BL Magnetic Field Map Discussion

This Appendix presents differences between the values of the magnetic field in the field maps and in the G4BL *genericquad* quadrupole magnets. *Figure* C.1 presents the difference between the B_x components of the two maps, *Figure* C.2 presents the difference between the B_y components, and *Figure* C.3 focuses on the B_z components. Finally, *Figure* C.4 shows the difference between $|\overline{B}|$ for the two maps.

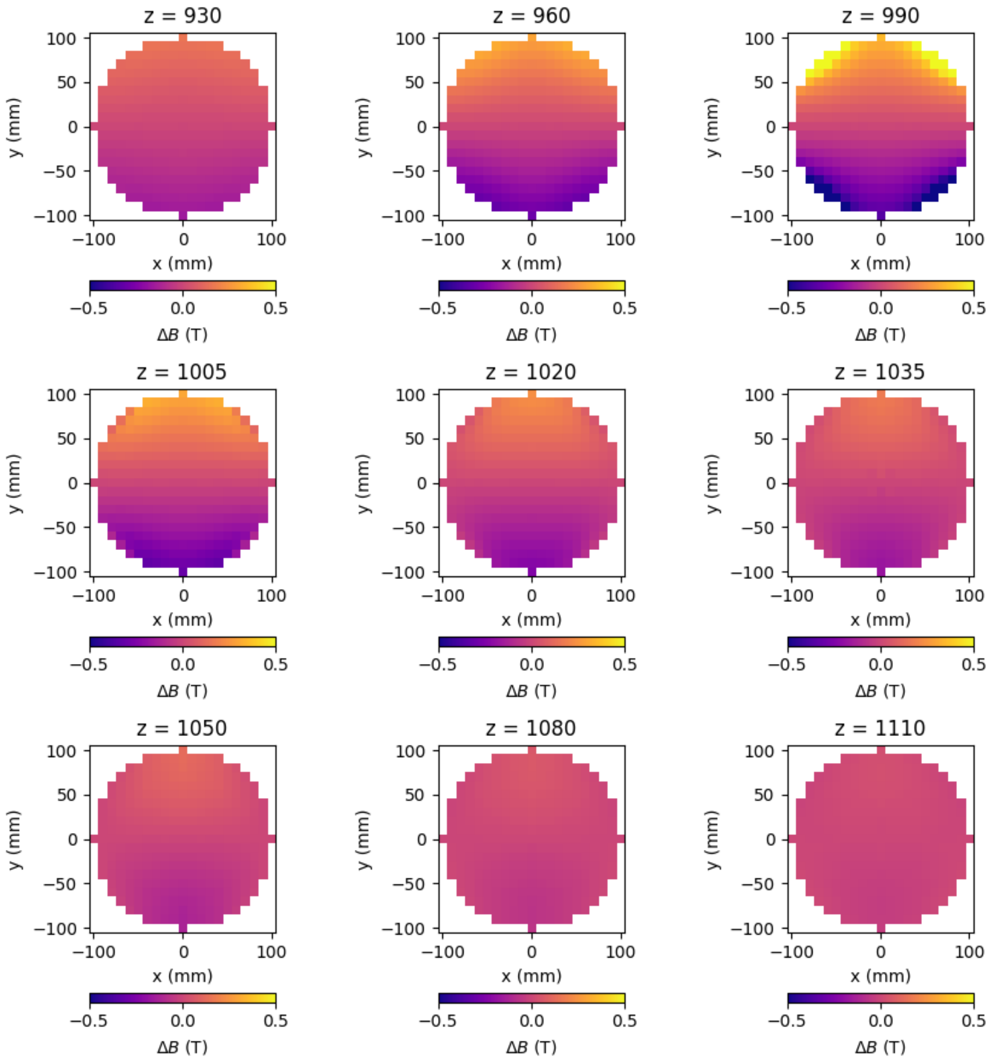

Figure C.1: The difference in the B_x component of the OPERA simulations and the G4BL *genericquad* field map at various z values (in mm) inside and outside of the magnets' cores.

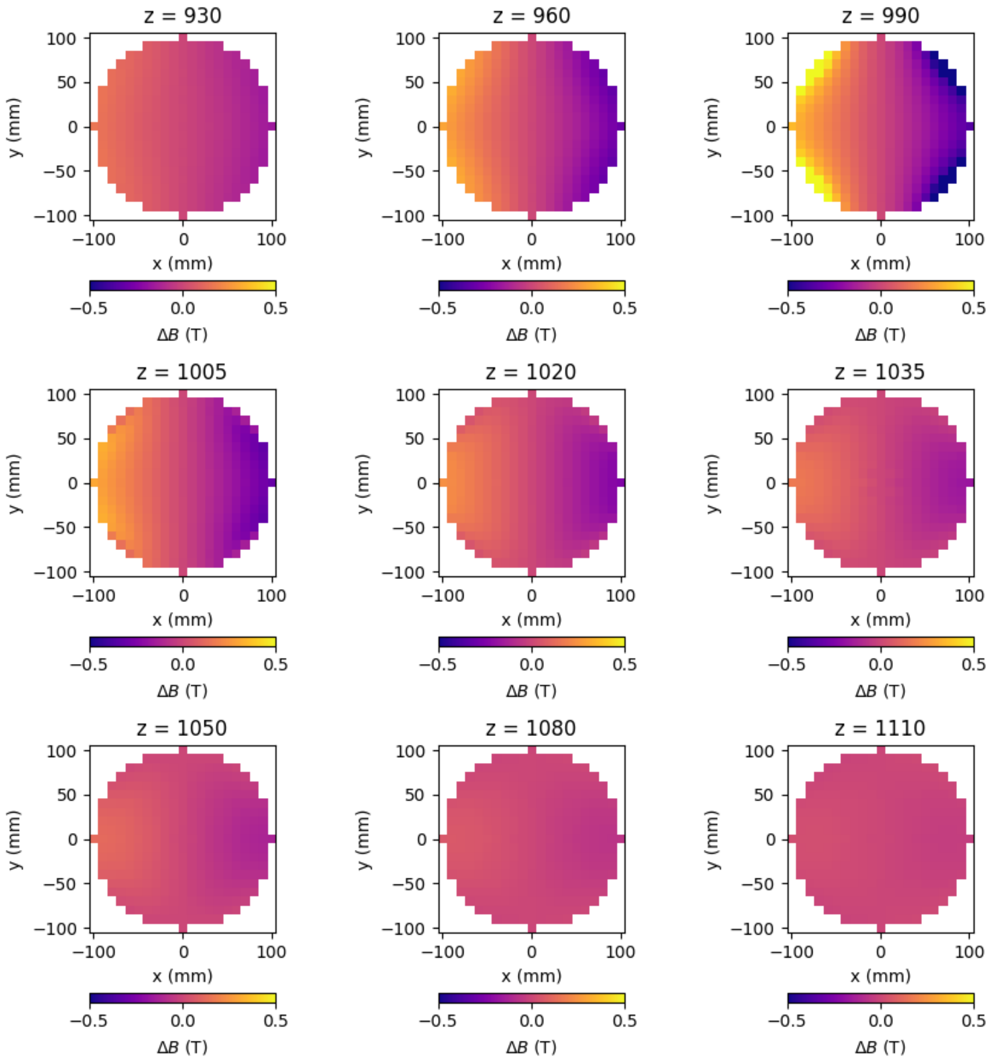

Figure C.2: The difference in the B_y component of the OPERA simulations and the G4BL *genericquad* field map at various z values (in mm) inside and outside of the magnets' cores.

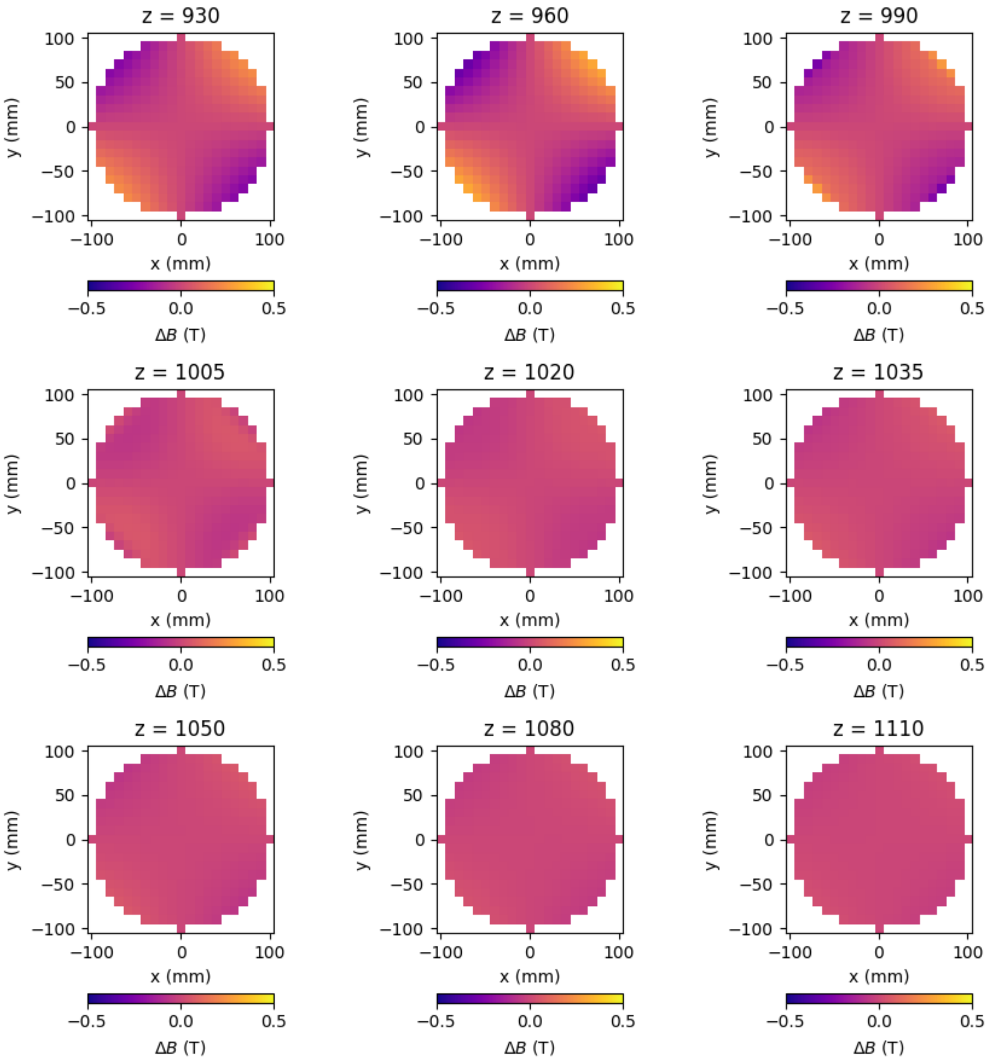

Figure C.3: The difference in the B_z component of the OPERA simulations and the G4BL *genericquad* field map at various z values inside (in mm) and outside of the magnets' cores.

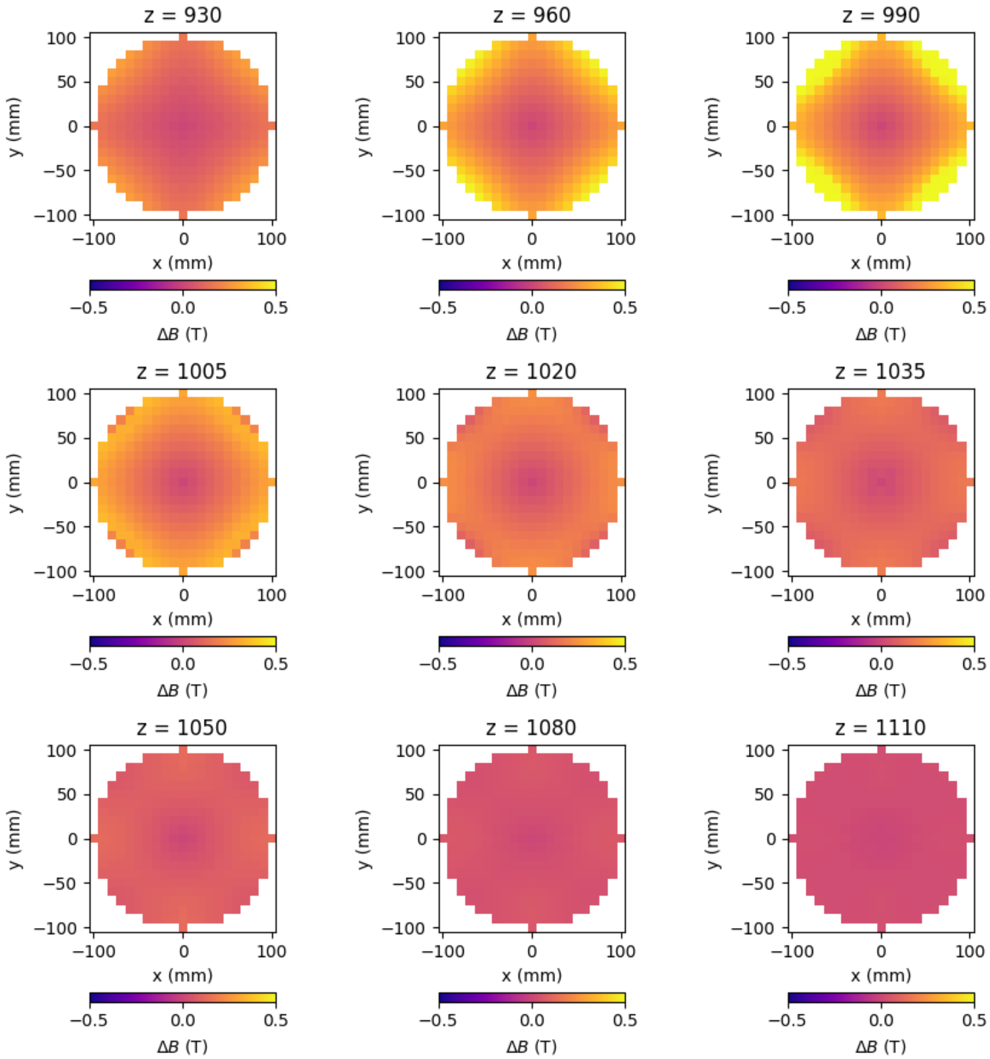

Figure C.4: The difference in the $|\overline{B}|$ component of the OPERA simulations and the G4BL *genericquad* field map at various z values (in mm) inside and outside of the magnets' cores.

Appendix D

Optics for H2-2024

In this Appendix alternative optics for the H2 beamline in the H2-2024 configuration are presented. In these, the beam properties at the NA61/SHINE target are identical to what is currently obtained using the H2 beamline. The optics presented are ones delivering a parallel beam to the NA61/SHINE target in *Figure* D.1 and *Figure* D.2, delivering a focused beam onto the MPTC of NA61/SHINE in *Figure* D.3 and *Figure* D.4, and finally delivering a focused beam of 450 GeV/c onto the NA61/SHINE target in *Figure* D.5 and *Figure* D.6.

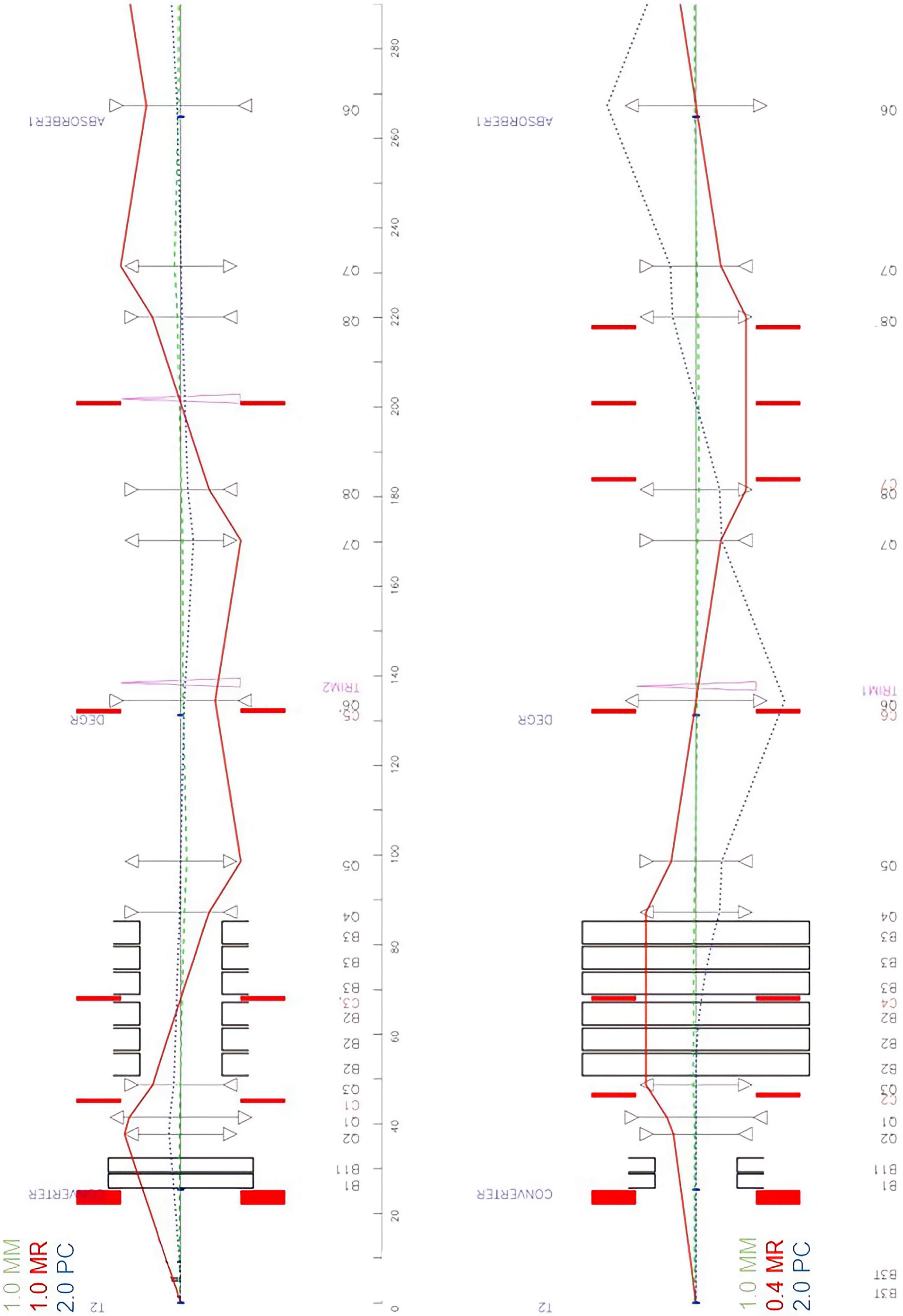

Figure D.1: Parallel beam to NA61/SHINE target (1/2).

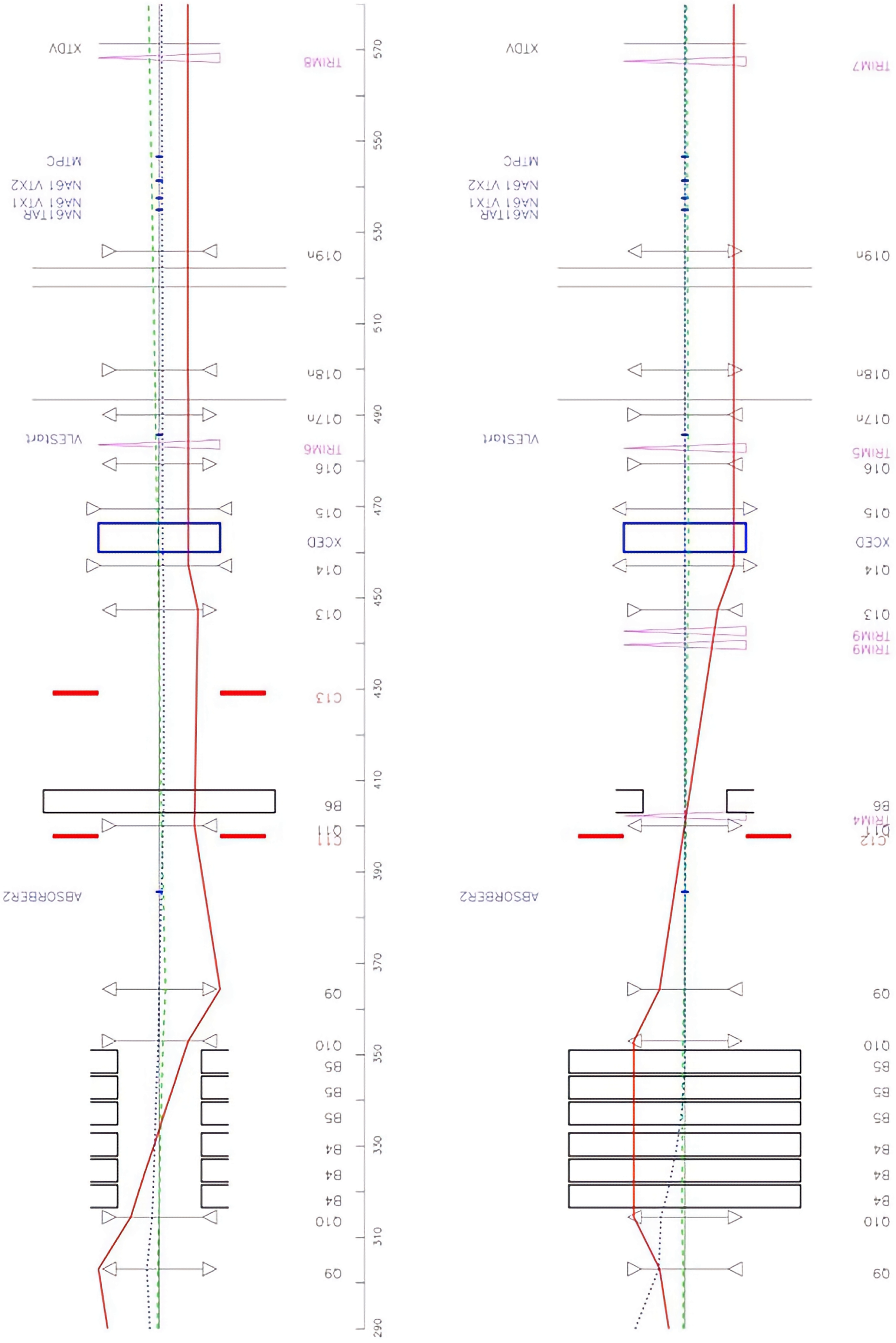

Figure D.2: Parallel beam to NA61/SHINE target (2/2).

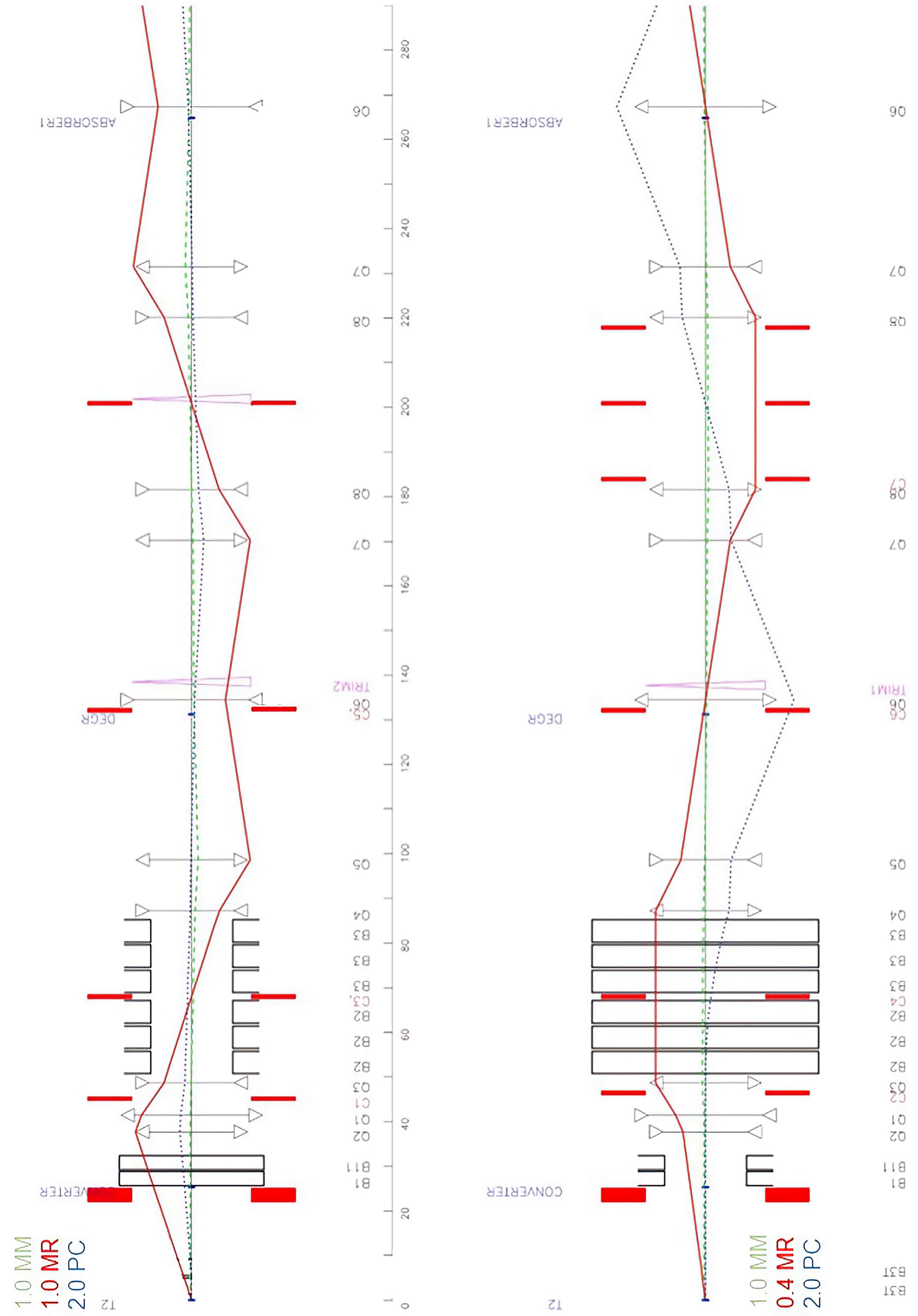

Figure D.3: Focused beam to NA61/SHINE MTPC at 300 GeV/c (1/2).

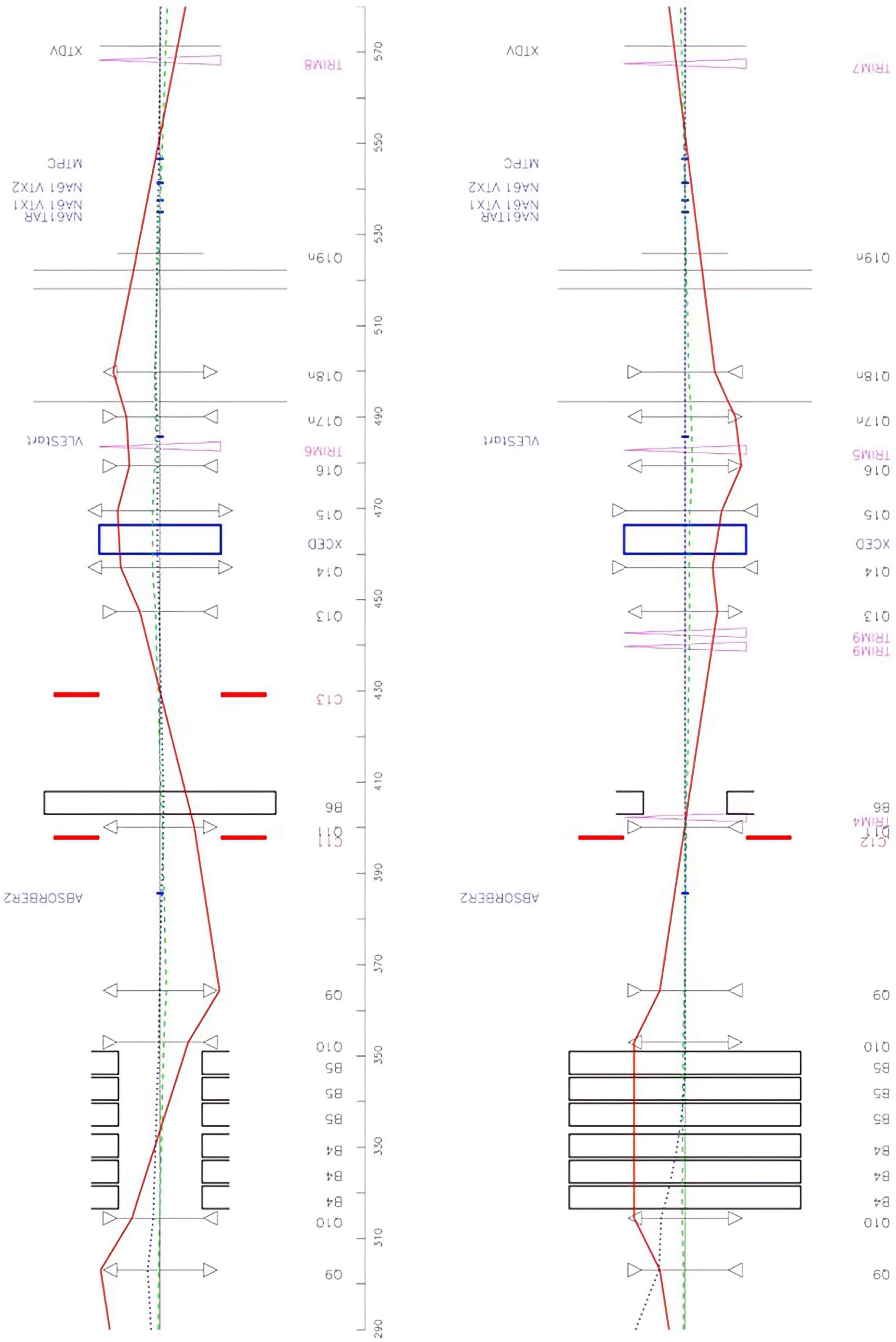

Figure D.4: Focused beam to NA61/SHINE MTPC at 300 GeV/c (2/2).

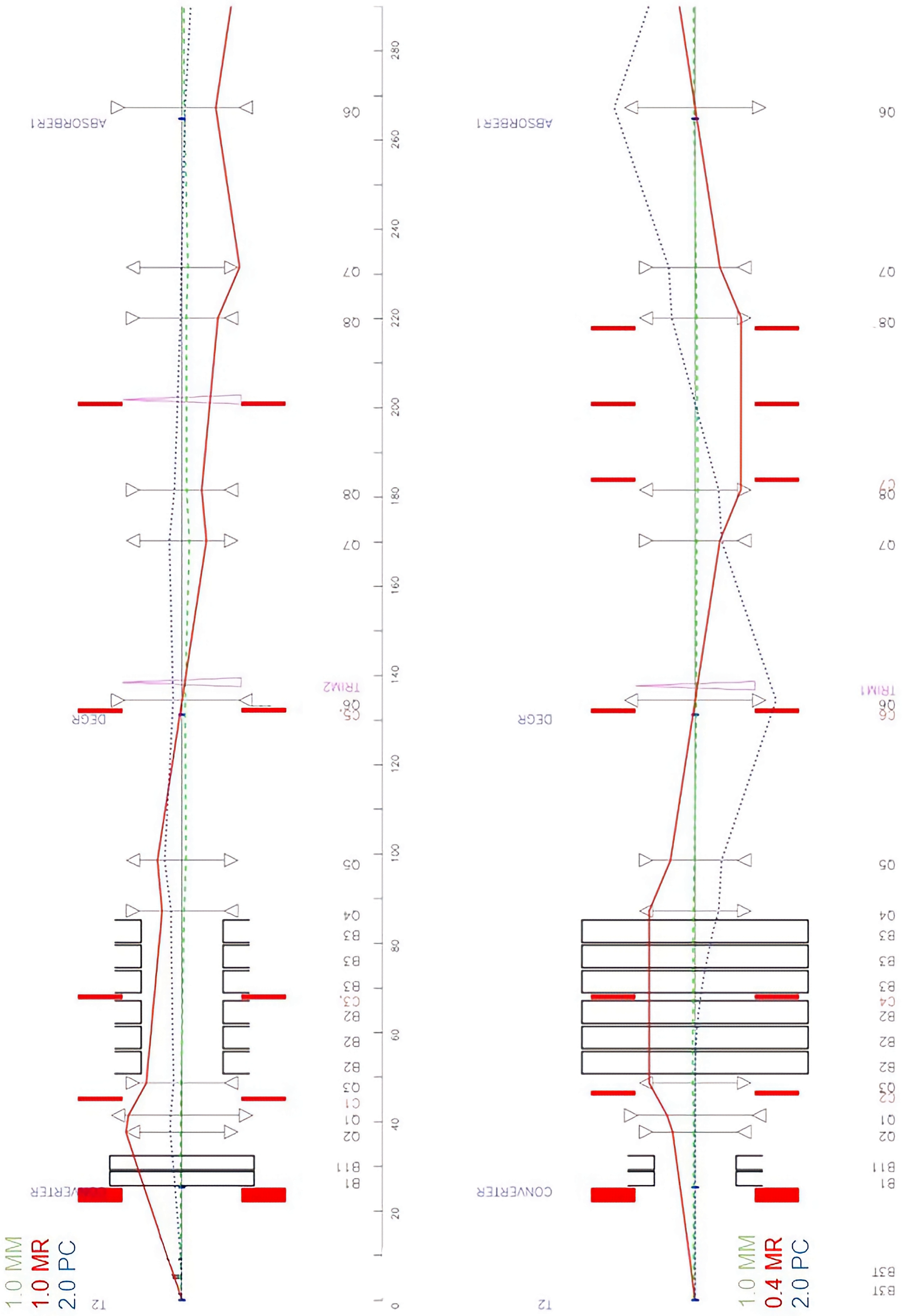

Figure D.5: Focused beam to NA61/SHINE target at 450 GeV/c (1/2).

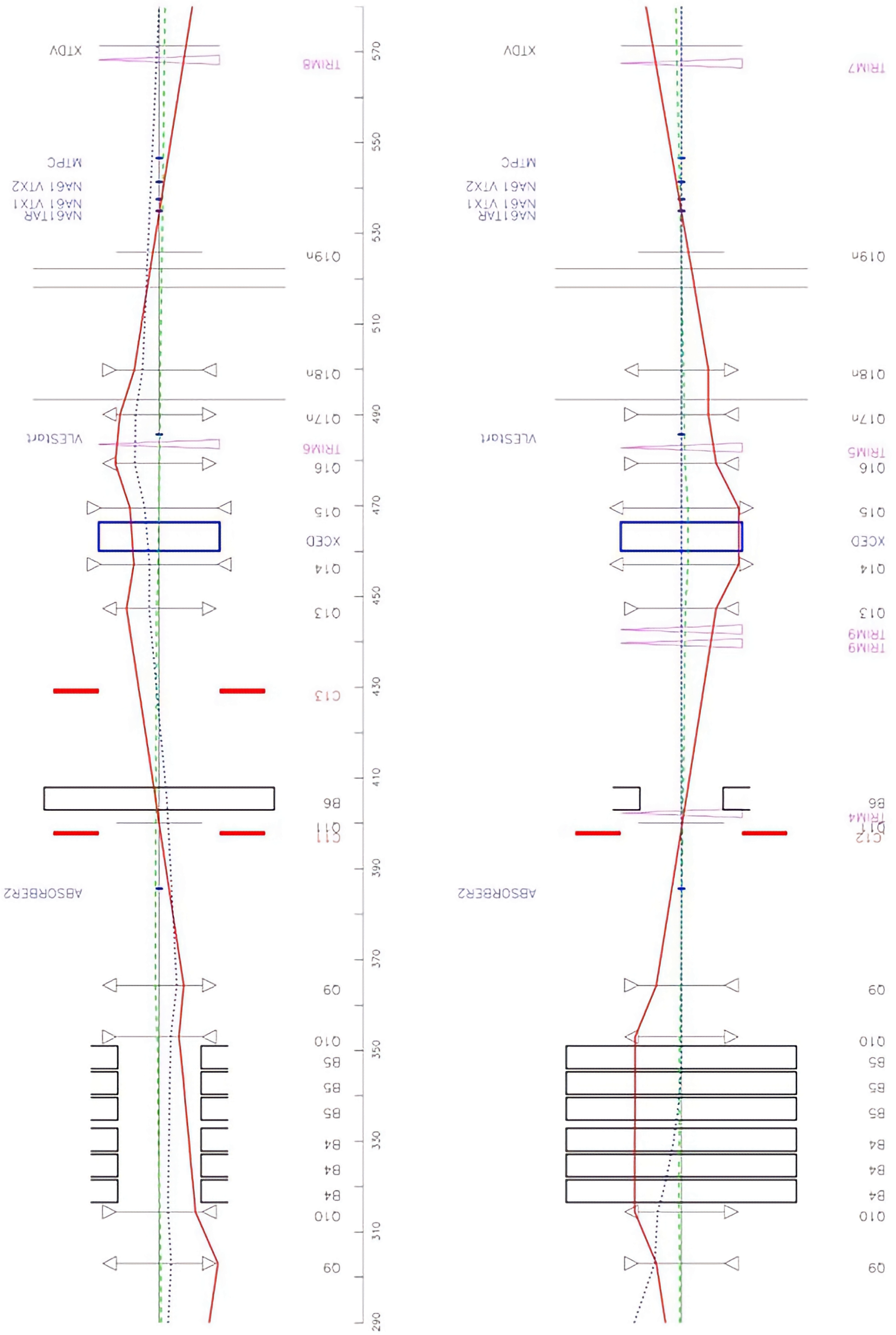

Figure D.6: Focused beam to NA61/SHINE target at 450 GeV/c (2/2).